8-2020

High Temperature Epoxy Composites for Material Extrusion Additive Manufacturing

Madeline G. Wimmer
University of Tennessee, mwimmer1@vols.utk.edu

To the Graduate Council:

I am submitting herewith a thesis written by Madeline G. Wimmer entitled "High Temperature Epoxy Composites for Material Extrusion Additive Manufacturing." I have examined the final electronic copy of this thesis for form and content and recommend that it be accepted in partial fulfillment of the requirements for the degree of Master of Science, with a major in Engineering Science.

Brett G. Compton, Major Professor

We have read this thesis and recommend its acceptance:

Chad Duty, Christopher Wetteland

Accepted for the Council:
Dixie L. Thompson

Vice Provost and Dean of the Graduate School

(Original signatures are on file with official student records.)

High Temperature Epoxy Composites for Material Extrusion Additive Manufacturing

A Thesis Presented for the

Master of Science

Degree

The University of Tennessee, Knoxville

Madeline G. Wimmer

August 2020

ACKNOWLEDGEMENTS

I would first like to thank my advisor, Dr. Brett Compton, for his support, insight, guidance, and humor throughout my master's program. I began this project knowing little about research and am thankful to him for teaching me how to both ask and answer better questions. My lab mates – Willie Kemp, Nadim Hmeidat, Stian Romberg, Cody Pack, Dustin Gilmer, and Michael Roberts – have been a constant source of encouragement and helpful discussions. To Samantha Maness, Bo Wagner, and Cole Wilder, thank you for your help in creating and testing samples. Specifically, to Cole Wilder for fiber length measurements.

Thank you to my committee members, Dr. Chad Duty and Dr. Chris Wetteland. In addition, I would like to thank Dr. Wetteland along with Dr. Gerald Egeland, and Zane Palmer for the use of characterization equipment through the University of Tennessee Center for Materials Processing. Without the use of their lab equipment, this project would not have been possible. Moreover, I would like to thank them for their skills and knowledge which they have shared.

I would like to thank Mark Edwards, Masaharu Takahashi, Hiromu Takahashi, and Akihito Iwasaki of Sun Chemical / DIC Corporation for their help in formulating the high temperature systems. Their resin suggestions and processing experience were invaluable for development of the printable feedstock.

Lastly, I would like to acknowledge and thank the Air Force Research Laboratory for funding this work. Specifically, I thank Dr. Jeff Baur and Dr. Hilmar Koerner for their guidance and feedback throughout these two years.

ABSTRACT

The geometric design freedom, short lead time, and customization make additive manufacturing (AM) increasingly popular. In addition to rapid prototyping and three-dimensional molds, additive manufacturing has created wind turbine blades, robotic arms, and custom medical implants. Major manufacturing companies such as Porsche and Aetrex are utilizing AM to customize automotive seats and orthopedic footwear. However, available materials limit AM applications. Currently, the high-temperature requirements from the aerospace and automotive industries provide additional, unmet challenges.

Many high-temperature epoxies have high pre-polymer viscosities and produce highly exothermic cure reactions, which limits volumetric scaling. Traditionally, fast, high-temperature processing reduces the viscosity, filling a mold before crosslinking initiation; however, this is not possible for AM. Currently, epoxy-fiber composites replace many traditional materials, such as aluminum, in applications where their high strength-to-weight ratios reduce lifetime energy costs. Fiber composites are limited by current fabrication methods, which can be expensive with limited geometric adaptability. Direct ink write (DIW) AM extrudes viscoelastic feedstock, creating parts layer-by-layer. The ink feedstock can readily incorporate fibers while AM produces parts without a mold reducing start-up requirements.

This work aims to develop a high-temperature fiber-filled feedstock while broadly considering print and extrusion parameters of viscous inks. Two pre-polymers are combined, to maintain a glass transition temperature upwards of 285°C while reducing the viscosity. A heated deposition system requires understanding the thermal viscosity and cure profiles. With a viscosity of 5.4 Pa.s and an 18-hour pot life, 70°C allows for shear flow without premature cure during extrusion. This formulation achieves strength and modulus values of 145 MPa and 4.9 GPa, respectively. An upper loading limit of 30 vol% glass fibers was determined. The fibers improve the heat deflection temperature by 100°C to 320°C and yield a 160% increase in flexure modulus; however, a 34% reduction in strength occurs. While processing did not decrease the fiber length as observed with carbon, the initial distribution contained 15% of fibers shorter than the critical length. The short fibers and pores that arose from both processing and dissimilar fiber-matrix expansion can account for the reduction.

TABLE OF CONTENTS

LIST OF TABLES

LIST OF FIGURES

CHAPTER ONE
INTRODUCTION AND MOTIVATION

This chapter details general background on additive manufacturing, specifically direct-ink write applications, and fiber composites. It provides both historical and current work to give context and motivate current work.

1.1. Additive Manufacturing

First developed in the mid-1980's, additive manufacturing (AM, 3-D printing) allows for production of near-net shape parts by building material layer by layer [1-3]. Initially developed for rapid prototyping, AM has since found applications for specialty parts, low volume production, and custom, lightweight molds [4, 5]. While polymeric materials are most common with the advent of the personal printer [2], ceramic [6], metal [7], medical [8, 9], and food [10] applications exist. Additive manufacturing creates near net-shape products, reduces material consumption by selective infills, and allows for on-site production. All of which lower both the cost and carbon footprint by reducing material consumption and energy expenditure during production and transport [11]. At the 2013 State of the Union address, President Obama predicted that "3D printing has the potential to revolutionize the way we make almost everything" [12].

Although slower than established methods, such as injection molding, AM is quickly customizable and adaptable as additional machinery, such as molds which can be expensive, are not required. Recently, AM has been called upon to produce parts combatting the global shortage of medical supplies required for COVID-19. In Italy, the company Isinnova produced ventilator valves for respirators. Within 24 hours, the valve was designed, built, and in use [13]. In the United States, businesses, universities, and the general public with 3-D printers were called upon to print parts for personal protection equipment to be delivered to local hospitals [14-16].

However, additive manufacturing remains is its infancy. Challenges are still being determined and applications are limited, but growing. A cost analysis conducted by Franchetti *et al.* considered total material, initial capital, time, energy, waste material, and labor costs to determine that for high volume production, current methods, such as injection molding, are less expensive above some break-even threshold [17]. Rather than directly competing with

established manufacturing methods, AM allows for the production of parts that previously was not possible. Through topology optimization, material placement is optimized and only added where required [18]. For example, the company Jabil redesigned an impeller reducing 73 parts to a single unit [19]. AM is excellent for customized, difficult-to-machine parts for on-demand manufacturing [20].

3D printing allows for remote areas to produce parts as needed, reducing transport time and cost. A notable example is National Aeronautics and Space Administration (NASA) astronauts aboard the International Space Station (ISS) forming tools in space that were then recycled and reformed [21]. Corporations are finding ways to incorporate AM into current manufacturing methods. Creating parts via AM allows for in-house production and a shorter lead time as Bell Helicopter demonstrated by reducing manufacturing time from 6 weeks to 2.5 days [20]. Companies such as Porsche [22, 23] and Aetrex [24] are capitalizing on the “complexity is free” feature to create custom parts to fit individual consumer needs. Accounting for 18.2% of the total additive manufacturing market in 2017, the aerospace industry dominates a significant portion of the field [25]. Although these applications generally require metals for operating temperatures above 400dC, high temperature polymer matrix composites (PMC) can be easier to manufacture and reduce the overall weight of the structure making it an attractive alternative. As AM becomes more common for end-use applications [22, 26], high-performance printable materials must continue to be developed.

Direct-ink writing (DIW), a type of material extrusion additive manufacturing, is used to fabricate components by extruding viscoelastic feedstock materials through deposition nozzles mounted to a computer-controlled multi-axis motion platform as depicted in figure 1. Although developed in the 1990s by Cima, Cesarano, and Calvert [27-30] and utilized to 3D-print a broad range of materials, from structural and functional ceramic slurries [31, 32], to conductive inks [33], to gels and biomaterials [34], DIW has recently found increased attention as a route to print structural thermoset polymers and thermoset polymer composites like epoxy resins [35-37], polyurea elastomers [38, 39], and vinyl ester resins [40]. In addition, recent work has focused on scaling up DIW of thermoset materials – which has traditionally been limited to benchtop hardware and printed items on the order of tens of millimeters to centimeters in dimension – to industrial level [41] with the goal of additive manufacturing of thermally-stable tooling and lightweight structural components [35]. This work will focus on DIW of a thermoset, specifically, a high temperature epoxy resin.

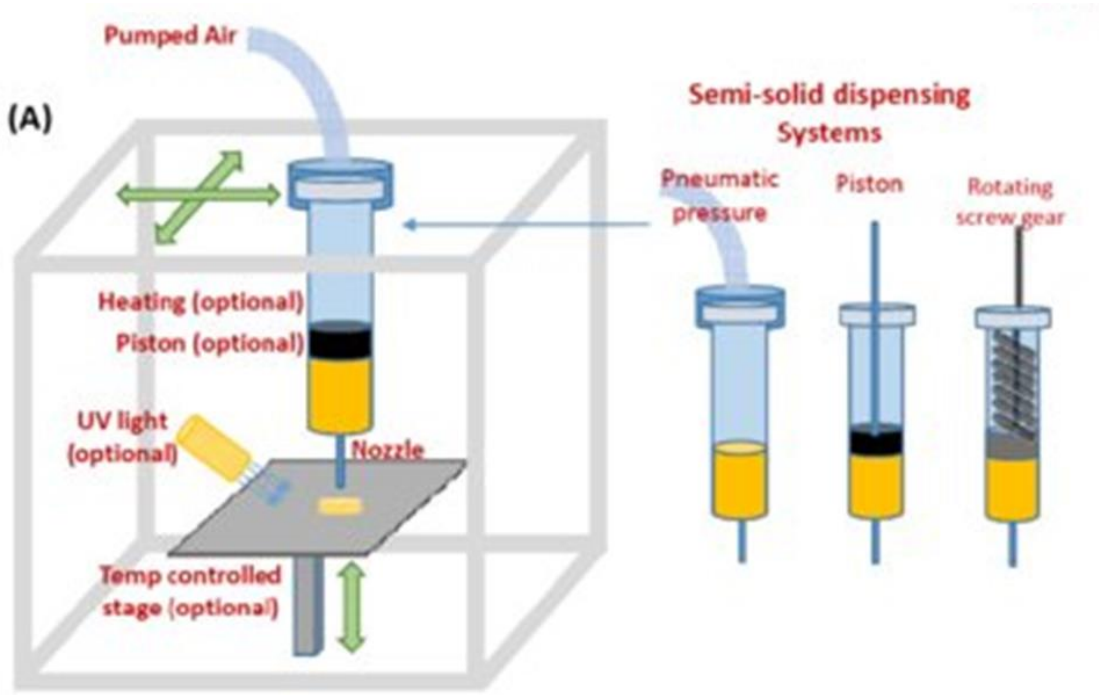

Figure 1. *Direct Ink Write Additive Manufacturing schematic [42].*

1.2. Epoxy

Epoxies are thermosets which means that they undergo an irreversible crosslinking reaction when heated unlike thermoplastics which melt and are recyclable. This crosslinking leads to high chemical resistance, good dimensional stability, stiffness, and strength. However, for application in demanding aerospace environments, power electronics, and as tooling for high performance autoclave-cure composites, a glass transition temperature (T_g) above 200°C is required [43, 44]. Although additive manufacturing of high-temperature thermoplastics is being explored via fused filament fabrication (FFF) methods [45, 46], thermoplastics melt when heated and lack the long-term thermal stability that thermosets provide. While some epoxies have been formulated for high-temperature coatings, the curing agent and cure profile largely impact the final thermal and mechanical properties by controlling the crosslinking density and degree of cure respectively [47]. High temperature epoxy work by Silva *et al*. achieved a T_g of 140 - 160°C [48] and 132°C was reached by Pierson *et al* [49]. High temperature epoxies are generally highly viscous and tend to produce highly exothermic cure reactions which complicate processing and scalability, as will be discussed in chapter 2.2. However, epoxies present good fiber compatibility and are readily printable [37]. Other high temperature thermosets, such as bismaleimides, phenolic resins, and cyanate esters exist. However, these can be difficult to process, brittle, require energy intensive cure schedules, and are toxic [50-53]. Figure 2 compares the glass transition temperature and modulus of selected epoxies, high temperature thermosets, and thermoplastics; filled markers indicate that the material has been printed.

1.3. Fiber Composites

Commonly injection molded [73] or formed into woven fiber mats [74], traditional fiber composites play a large role in the manufacturing industry. Epoxies are commonly used as the matrix for their strong fiber adhesion and good wetting properties [75]. They can be found in applications from lightweight alternative for sporting equipment to structural aerospace components [76-78]. Although fiber composites are more expensive than traditional structural materials – such as aluminum, steel, or wood – the lightweight design reduces lifetime energy costs [79].

As of current, work has focused on characterizing carbon fibers (CF) for DIW AM applications. [49, 66, 80, 81]. However, glass fibers (GF) are 5 – 10 times less expensive than their carbon counterparts [82], are IR transparent making them an excellent candidate for radome

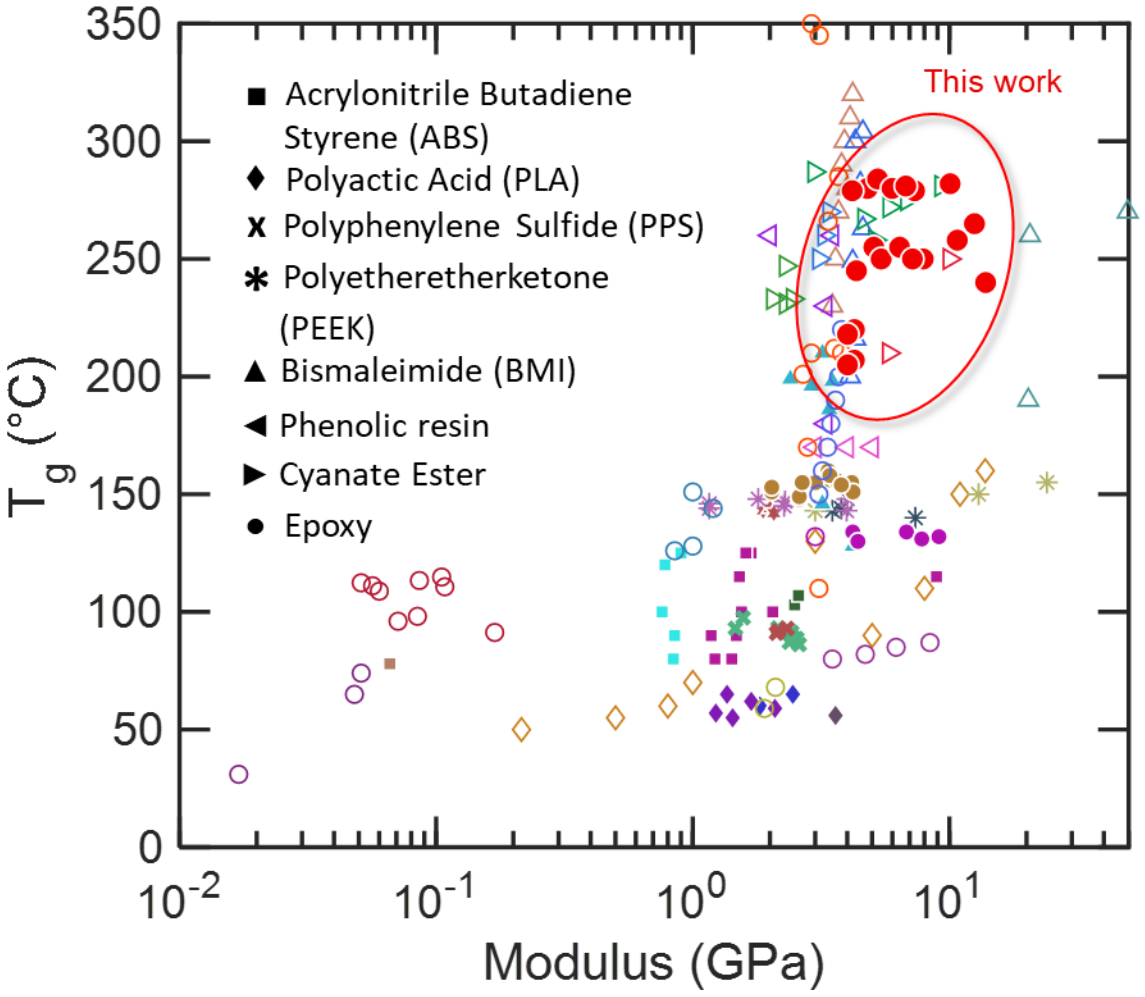

Figure 2. *Glass transition temperature vs. modulus for several polymers. Circles indicate epoxies, triangles are other thermosets, and squares are thermoplastics. Filled markers indicate that the material is printed while unfilled points correspond to non-printed work. Refs: Epoxy (●) [37, 43, 48, 49, 54 – 56], polyetheretherketone (PEEK, ⋆) [9, 57 - 59], bismaleimide (BMI, ▲) [50, 56, 60-62], phenolic resin (◄) [56, 63], cyanide ester (►) [56, 64, 65], polyphenylene sulfide (PPS,* ***x****) [45, 58], acrylonitrile butadiene styrene (ABS, ■) [66 – 69], and polyactic acid (PLA, ♦) [68, 70-72].*

applications [83], generally have strengths around 2,000 MPa and moduli of 80 GPa [84], and are stronger off-axis than carbon fibers [73].

The design freedom and with the mold-free formation provided by AM will expand current fiber applications. Love *et al.* noted that printed fiber composites have improved dimensional and thermal stability as compared to the neat polymer [66]. Fibers improve the strength and modulus by up to 115% and 700% as determined by Tekinalp *et al*. which allows for printing of load-bearing parts [85]. However, printed fiber composites have increased anisotropy and pores are common [86]. Despite this, printed composites are essential for improved mechanical properties of printed components.

1.4. Project Overview

This work aims to develop and characterize a novel high temperature (T_g > 200°C) epoxy feedstock using commercially available resins for direct ink write additive manufacturing. This will allow for automotive [87], aerospace [76], and autoclave mold [88] applications. The addition of glass fibers will improve the both the thermal and mechanical properties [66, 89], enabling further uses for structural applications. The work can be divided into three subsections: epoxy selection, formulation, and fiber incorporation.

First, a viable epoxy resin for DIW is required. Five commercial epoxies are considered and evaluated based on the T_g, cure behavior, and ease of processing. Because a high glass transition temperature is achieved from low free volume, these resin precursors generally present high uncured viscosities which can limit extrusion processes. However, none of the tested resins achieved a T_g above 200°C while meeting the printability requirements. This required a blending of two resins to create a DIW feedstock.

This work introduces a heated printing approach for a novel semi-solid high temperature epoxy-based ink that addresses several of the challenges associated with solvent-based printing and thermoplastic melt-based printing of polymer composites. A high-temperature solid resin and a lower-temperature liquid resin are blended in varying ratios with a latent curing agent to form a 3D-printable system that possess a cured T_g above 200°C while remaining sufficiently inert at intermediate temperatures (60 – 90°C) allowing for formation and printing of complex, tall structures that remain stable during a heated cure.

The third task incorporates up to 30 vol% glass fibers into the high temperature epoxy ink developed in task two. Fiber length measurements are conducted throughout the mixing process

to confirm minimal breakage during formulation. Thermal and mechanical properties of four formulations – 0, 10, 20, and 30 vol% GF – are compared along with processing considerations.

CHAPTER TWO
SCIENTIFIC BACKGROUND

This chapter provides the technical knowledge required for the work.

2.1. Additive Manufacturing Requirements

All additive manufacturing processes involve the gradual buildup of material layer-by-layer. While methods vary between techniques, all allow for the production of a part directly from a computer aided drafted (CAD) file to create a near-net shape part [2]. This requires the selective placement of material that remains free-standing for the duration of production. For methods such as binder jetting of metals [90] or selective laser sintering (SLS) of metals, polymers, or ceramics [91], this is accomplished by coalescing selected regions in a bed of material by sintering or a photo-initiated crosslinker. Extrusion based methods hold the bulk material in a secondary vat and selectively place material where needed. These methods are common, found in fused filament fabrication (FFF) [92], fused deposition modelling (FDM) [93], big area additive manufacturing (BAAM) [94], fused deposition of ceramics [29], and DIW [27].

2.1.1. Viscoelastic fluids

Not all viscous materials lend themselves to extrusion-based printing. Work by Duty *et al*. characterized the material property requirements for successful printing. The first, material extrusion, quantifies the shear thinning and pressure requirements for feedstock to flow. The second, bead geometry, stipulates that an extruded bead must maintain shape. Additionally, the material must maintain bead functionality and previously printed layers remain stable when additional material increases the height. Lastly, the printed structure must retain geometric functionality [94]. These requirements can be evaluated through rheology.

Parallel plate rheology incudes an oscillating shear force on a material at some prescribed frequency. This can be used to determine the storage, E', and loss, E", modulus as well as the viscosity, η, when the resin experiences a shear force as occurs during DIW extrusion. The storage modulus, E', provides information about the viscoelastic nature of the material. Conversely, the loss modulus, E", describes the energy lost due to friction or heat [95]. Conducting a stress sweep at a given temperature gives information about the relative stability

and flow under pressure. At low stresses which correspond to the steady-state nature of a material before or after printing, the storage modulus must be less than the loss indicating elastic solid properties [94]. However, the material must exhibit shear thinning behavior to flow. Defined as the tangent intercept between the initial linear viscoelastic region and subsequent decrease in the loss moduli as the stress increases, the shear yield stress, τ_y, can indicate both flow and stability.

For thermoplastics, the material is heated to above the melting temperature, reducing τ_y for extrusion. Upon cooling, the viscosity decreases resulting in a stable structure [45]. However, this creates thermal gradients within the part that can lead to warping, cracking, and layer deboning [46]. Additionally, printed thermoplastics can have poor interlayer bonding which imposes anisotropy. Work by Abbott *et al.* found an 80% reduction of strength when measured along versus against the bead direction [92]. However, thermosets cure when heated and a different process is employed.

2.1.2. Direct Ink Write

Direct ink write printing can be applied for a range of paste-like viscoelastic fluids including ceramic slurries [6, 29], gels and biomaterials [33, 34], conductive materials for sensors [96], and epoxies [35, 41, 97, 98]. This work will focus on epoxy thermosetting resins. As a thermoset, epoxies require a secondary cure during [99] or after [37] extrusion where the printed part must remain stable.

Rheological Modification - Nanofillers

Many epoxies are fluid at room temperature, do not experience shear thinning, and require rheological modification through a filler material. Work by Compton *et al*. determined that high-aspect ratio fillers, such as fibers, do not produce appropriate shear thinning behavior with an epoxy-graphene ink (τ_y = 70 Pa) unable to hold shape above 2-3 mm in height [36]. Rather, a low-aspect ratio functionalized nanofiller, commonly nanoclay [49, 80] and fumed silica [27, 100], is utilized. Hmeidat *et al.* determined that for $1x10^2 < \tau_y < 1x10^3$ Pa, room temperature extrusion works well and prints maintain structure [37]. The nanoclay acts as a rheological modifier to impose shear thinning properties, increase the stability, and decrease the effects of temperature on viscosity. The nanofiller allows the material to extrude from a nozzle at a constant rate under an applied pressure and maintain structure until cured.

DIW Extrusion

DIW behaves similar to FFF by extruding a constant stream of material to form the printed part layer by layer using a multi-axis print platform as demonstrated in figure 3 [101]. Some overlap with the previous layer is required to fully bond the material for a fully dense part. Wang and Shaw determined a critical nozzle height, h_c, such that the material retains dimensional stability without a squeezing effect as would be seen for $h < h_c$, but the cross-sectional geometry is no longer dictated by just the rheological properties and ink wettability ($h > h_c$). The critical height can be defined by

$$h_c = \frac{V_d}{v_n D_n} \qquad 1$$

where V_d is the volume of extruded ink per unit time, v_n is the print head speed, and D_n is the nozzle diameter [102].

The process is highly adaptable and can print a wide range of materials as discussed above. Because crosslinking occurs after extrusion, limited overhangs are achievable, although partial curing during extrusion can improve this [99]. Direct ink write additive manufacturing provides excellent print control and can be applied to a large range of materials with varying filler materials making it attractive for continued development.

2.2. High Temperature Epoxies

Thermal stability can be determined by the glass transition or heat deflection temperature and is related to the relative motion of the polymer chains. Some pre-polymeric resins have been formulated for high temperature applications. However, the curing agent and cure profile determine the final crosslinking density of the solid epoxy. As such, the pre-polymer, curing agent, relative ratios, cure time, and temperature must all be considered to determine the final properties.

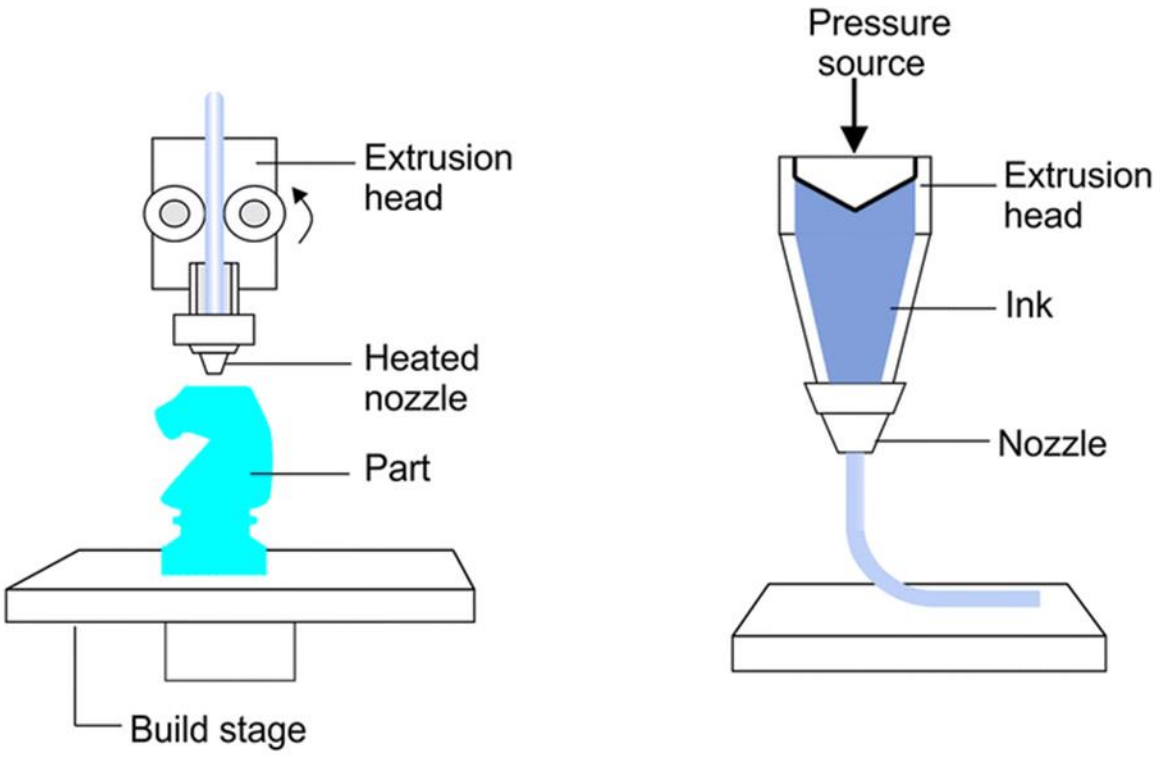

Figure 3. *Comparison of thermoplastic FFF additive manufacturing and DIW. Refs: [103] adapted from [104, 105].*

In addition to the shear thinning and bead stability requirements for DIW AM, two additional challenges must be considered for a high temperature thermoset system. Pre-polymers that have been formulated for high temperature applications are often bulky molecules with high molecular weights that yield high viscosities and many are solid [106-108]. Further, many of these are recommended for thin film applications as the cure reaction is highly exothermic [109, 110]. Scaling up to bulk parts can produce excess heat leading to auto-acceleration where the effects compound and can become dangerous. As such, to print these systems, the initial resin viscosity must be reduced and the heat produced during cure must be controlled.

2.2.1. Glass Transition and Heat Deflection Temperatures

As a second order transition, the glass transition temperature is determined by kinetic limitations to movement rather than a thermodynamic equilibrium [111]. Rather, the glass transition temperature is a measure of the free volume and molecular mobility of a structure [112, 113]. Free volume is a measure of remaining available space for the polymer chains to occupy and can arise from motion of the chain ends, side chains, or main chain itself. Lower free volume corresponds to less possible chain motion as the molecules become locked into place. Decreasing the number of end groups, length of side chains, and increasing the steric hindrance and the crosslinking density all lower the free volume and therefore increase the glass transition temperature [114, 115]. Crosslinking density depends on the curing agent and cure cycle with longer cures at higher temperatures increasing the T_g [116, 117]. Below the T_g, molecules are frozen leading to a polymer that is macroscopically hard and brittle. Above the transition point, molecules are able to experience rotational and translational motion resulting a rubbery bulk material [118]**.**

While the glass transition temperature considers molecular behavior, the heat deflection temperature (HDT) provides a practical measurement [112]. Defined by ASTM D648, the heat deflection temperature is the temperature where a sample in 3-point bend geometry distorts a set amount under a constant stress. The two values are similar for unfilled systems, but the HDT provides a macroscopic measurement and generally is 15°C lower for unfilled systems [119]. While both provide upper limits for the usable temperature, the HDT is a short-term test and additional work must be conducted to observe long-term behavior [120]. Further, while T_g is a material property of the resin, the HDT reflects the impact of reinforcing agents. While fibers are

commonly used [47], Wang *et al*. demonstrated that at low loading fractions (3 wt%), nanoclays can induce a 10.5% improvement in HDT [121].

While there are many methods to determine the T_g, including thermomechanical analysis (TMA) [122] and dynamic mechanical analysis (DMA) [123], measuring the heat capacity from differential scanning calorimetry (DSC) [124] provides a direct consideration of the molecular behavior. Both TMA and DMA measure macroscopic changes and generally yield higher T_g values [125, 126]. Although single values are reported, the glass transition temperature represents a range of temperatures and can vary with the heating rate [95]. As HDT measures deflection as a function of temperature, 3-point bend tests can be conducted using either DMA or TMA. While DMA employs larger samples which allows for measurements of as-printed properties, TMA provides more accurate load control and thin samples are less likely to experience a temperature gradient. For both of these tests, the heating rate generally ranges from 2 – 10°C/min with lower values being reported at slower rates [122-124].

Differential Scanning Calorimetry (DSC)

Heat is either released or adsorbed as a material undergoes a physical transformation. This energy transfer is measured by DSC. Because a material must adsorb energy to increase molecular mobility, the glass transition temperature is an endothermic reaction denoted by a decrease in the heat capacity at temperature from a DSC curve. After the transition, the slope levels and a new, linear steady-state is reached. The T_g is measured at the midpoint of the slope change [124].

For thermosets, DSC can also be used to determine the cure behavior. The cure is an exothermic reaction, and the change in enthalpy, ΔH, which describes the heat of cure can be determined by the area under the resultant DSC curve. Unlike the cure onset and peak temperatures, ΔH is independent of the heating rate. The degree of cure, α, at a given time, t, can be calculated by

$$\alpha(t) = \frac{H(t)}{H_T} \qquad 2$$

where H_T is the total heat released by the system [127]. The rate of reaction, $d\alpha/dt$, can be determined by

$$\frac{d\alpha}{dt} = \frac{1}{H_T}\frac{dH(t)}{dt}. \quad 3$$

Following this, the maximum rate of reaction occurs at the peak temperature. At faster heating rates, the exothermic peak increases in both magnitude and temperature which correlates to a faster cure [127, 128]. As such, lowering the cure rate or temperature results in a slower, more controlled cure [129].

Thermomechanical Analysis (TMA)

As materials heat, they expand which is measured by TMA. Quantified by the coefficient of thermal expansion (CTE), the rate increases above the T_g corresponding to the higher chain mobility [130]. Tests are conducted on 5 mm cubes experiencing a constant load [131]. The coefficient of thermal expansion can be calculated as

$$CTE = \frac{\Delta L}{L\,\Delta T} \quad 4$$

where *L* is the length being measured and *T* is the temperature [132]. When using the expansion probe, the length is the *z*-height. From TMA, T_g can be measured at the tangent intercept of the two slopes denoting the macroscopic expansion at a constant heating rate [95].

Also tested at a constant load, HDT experimentation utilizes a 3-point bend flexure geometry. The force is calculated for an individual sample to experience a constant stress, *S*, which is generally 0.455 or 1.82 MPa although other values are allowed [133]. The corresponding force, *F*, is determined through

$$F = \frac{2Sbd^2}{3L} \quad 5$$

where *b, d, and L* are the width, thickness, and gauge length respectively. Deformation, *D*, at 0.2% strain, *ε*, given in mm/m, follows

$$D = \frac{\varepsilon L^2}{6d}. \quad 6$$

The temperature at which a sample reaches this deformation is the heat deflection temperature. The 0.2% strain is standard; however, it is selected arbitrarily [134].

Dynamic Mechanical Analysis (DMA)

DMA probes a sample with an oscillating force at a set frequency to measure material recovery. This recovery can be divided into two parts. The first, the storage moduli, ***E'***, gives the elastic properties describing the recoverable energy after deformation. The damping properties are described by the loss modulus, ***E''***, which describes the energy lost due to friction and internal movement [95]. The ratio of the two is given by tan(δ) such that

$$tan(\delta) = E'/E". \quad 7$$

DMA is recommended for glass transition temperature measurements of continuous-fiber polymer matrix composites (PMC) [123]. The T_g can vary up to 25°C on the same test when measured from the storage moduli, loss moduli, or tan(δ) [95]. From the storage modulus, T_g can be determined from the intersection of two tangential lines below and above this value. Above T_g, more chain motion occurs increasing the amount of energy lost to heat. As such, both the onset and maximum temperatures from the loss modulus are used to mark the transition. However, Gupta *et al*. found a 20°C difference between the two methods [125]. Comparing the storage and loss moduli in tan(δ) shows the T_g as the maximum value of the resultant peak. Although this is the least ambiguous of the three methods, Paroli *et al*. found a 35% increase in T_g from tan(δ) DMA as compared to DSC, TMA, and E" from DMA [126]. Disagreement between E" measurements have led to only E' and tan(δ) approximations being incorporated into ASTM standards [123]. Table 1 summarizes characterization methods for both cured properties and uncured resin (see chapters 2.2.3 and 2.2.4).

2.2.2. Glass Transition Temperature and Viscosity

For polymers, movement along the molecular chain determines the T_g which is related to the relative size and bulkiness of the chain. Common chain motion methods include bending, stretching, rocking, rotating, twisting, and wagging of the individual atoms as depicted in figure 4. More atoms along the monomer backbone, tightly bonded molecules, and bulky groups all

Table 1. *Summary of characterization method and properties measured. Rheology is conducted on uncured samples, TMA and DMA measure cured properties, and DSC can be performed on either to obtain different results.*

Characterization Method		Properties Measured
Thermomechanical Analysis	TMA	Cured Epoxy, macro-expansion
		Glass Transition Temperature, T_g
		Coefficient of Thermal Expansion, CTE
		Cured Epoxy, constant force 3pt-flexure
		Heat Deflection Temperature, HDT
Dynamic Mechanical Analysis	DMA	Cured Epoxy, 3pt-flexure
		Glass Transition Temperature, T_g
		Storage Modulus, E'
		Loss Modulus, E"
		tan(δ)
Differential Scanning Calorimetry	DSC	Cured Epoxy
		Glass Transition Temperature, T_g
		Uncured Resin
		Heat produced via curing, ΔH
		Cure onset temperature, T_{onset}
		Temperature of maximum rate of cure, T_{peak}
Parallel Plate Rheology		Uncured Resin
		Storage Modulus, E'
		Loss Modulus, E"
		Viscosity, η

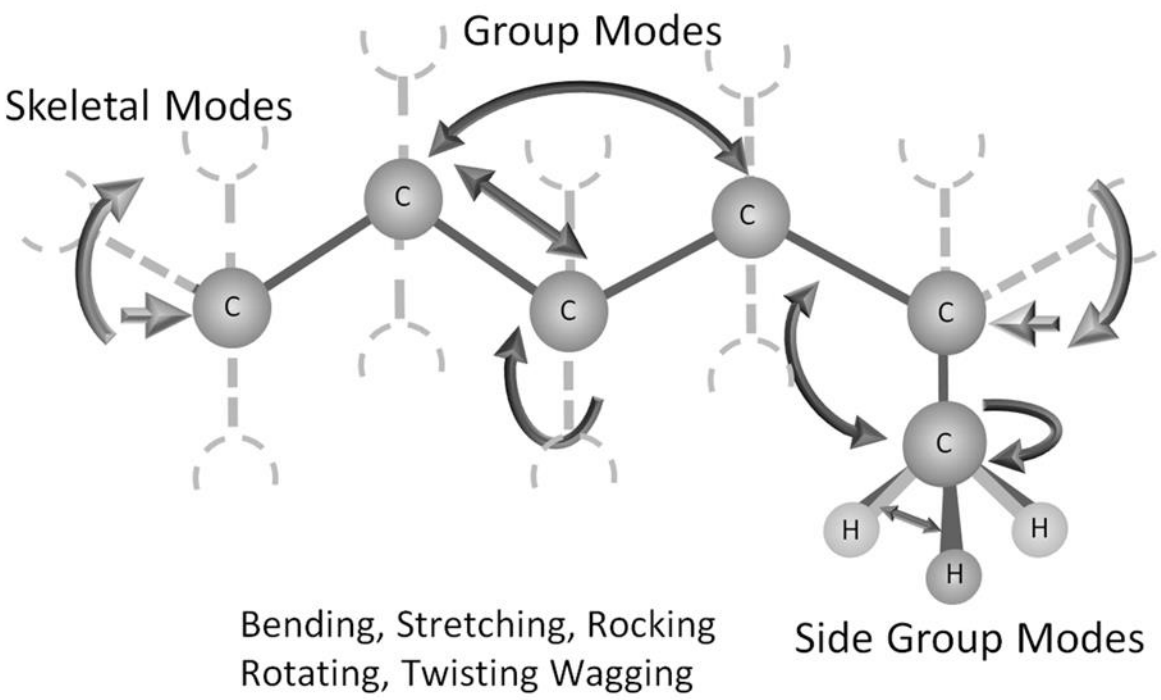

Figure 4. *Selected methods of polymer chain motion. Long, bulky chains require more energy to move which correspond to increased glass transition temperatures [136].*

increase the steric hindrance. In turn, this limits chain motion and the T_g increases [135]. While limiting motion increases the glass transition temperature, this also impacts room temperature properties. For uncured systems, bulky, high molecular weight pre-polymers increase the room temperature viscosity; once cured, they decrease the materials toughness leading to brittle materials [43].

The glass transition temperature of thermoset resin increases after the cure corresponding to the crosslinking density [115]. Many epoxies resins have initial T_g values that are below room temperature which results in a liquid pre-polymer. However, for high temperature epoxies, it is common for the initial T_g to be higher, leading to viscous or solid pre-polymers [107, 109].

In 1950, Flory and Fox developed a relationship between the number-average molecular weight (M_n) and T_g such that

$$T_g = T_{g,\infty} - \frac{K}{M_n} \quad 8$$

where K is a constant related to the total free volume and $T_{g,\infty}$ is the maximum theoretical glass transition temperature [111]. Because polymer chains vary in length, the molecular weight also varies following a Gaussian bell distribution. While several averaging methods exist, number and weight average are the most common. Using a generic variable, X, which can be the molecular weight, fiber length, or another factor which varies in length, the number average is defined as

$$X_N = \frac{\sum N_i X_i}{\sum N_i} \quad 9$$

and the weight average follows

$$X_W = \frac{\sum W_i X_i}{\sum W_i} \quad 10$$

where N_I and W_i are the number or weight of things X at length I [73]. Work by Fox *et al.* found that the short polymer chains have a larger impact on final properties, and the number-average calculations more closely agree (M_N = ± 5°C, M_W = ± 30°C) with measured values [111].

Molecules with long polymeric chains have high molecular weights and require more energy to move which increases the T_g. As observed by Chan *et al.*, for some high temperature systems, this can increase the pre-polymeric T_g such that uncured resins are solid at ambient temperatures [137]. Additionally, when there is less free volume in the system, there is less space to move in which also increases the T_g.

However, free volume and viscosity are also directly related. Large molecules result in steric hindrance and long chains limit motion. To achieve a high T_g, many pre-polymers have high degrees of steric hindrance before crosslinking occurs. As such, to achieve high temperature properties, a high viscosity resin will have to be used.

Figure 5 shows three resins used in this study along with their epoxide equivalent weight (EEW), room temperature viscosity, and cured T_g for a resin-4,4'-diaminodiphenylsulfone (DDS) system. The EEW will be discussed in chapter 2.2.4 and is included for comparison. In figure 5.a, a common Bisphenol A diglycidyl ether (DGEBPA) resin, Epon 826 [138], is shown. This system is liquid at room temperature and shows success as a printable base ink for DIW application [35, 37, 49]. A high-temperature, naphthalene-type, liquid resin, Epiclon HP-4032SS [109] is depicted in figure 5.b. Lastly, figure 5.c depicts Epiclon HP-7250 [109], a high-temperature "semi-solid" modified multi-functional resin. With the lowest viscosity (and lowest T_g), Epon 826 is a long chain with two functional epoxide groups. Although longer than HP-4032SS, there is a higher degree of freedom leading to a larger free volume. As a short chain with two phenol groups and two epoxide functional groups, HP-4032SS reaches a high crosslinking density to achieve its thermal properties. HP-7250 has ≥ 5 epoxide reaction sites and the same number of phenol groups. The phenol groups add bulkiness reducing the free volume and increasing the viscosity while the high number of reaction sites allow for an intertwined crosslinking structure.

This study also considers a solid epoxy, Epiclon HP-6000. However, the structure is proprietary and therefore not included. The T_g values are reported after curing with DDS as provided by the manufacture and other work. DDS will be discussed in chapter 2.2.5 and is known to produce high thermal properties, making it popular for aerospace applications [43]. However, DDS increases the uncured viscosity of a resin and is unable to be incorporated for DIW applications. As such, the measured values reported in this work are lower.

a)

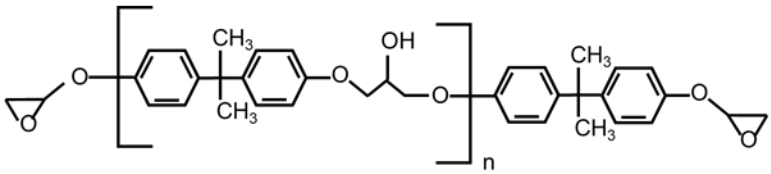

Epon 826 (common liquid)
EEW = 186 g/mol, η_{RT} = 4 Pa.s , T_g = 180°C

b)

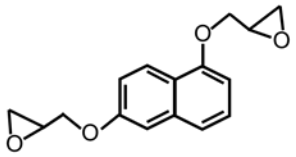

HP-4032SS (high temperature liquid)
EEW = 143 g/eq, η_{RT} = 39 Pa.s, T_g = 212°C

c)

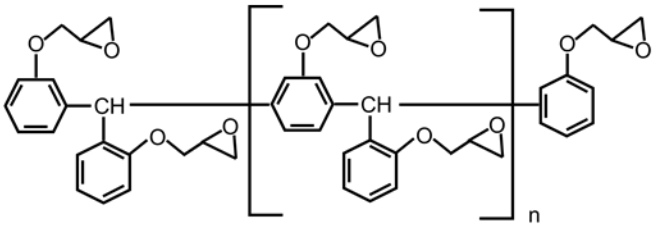

HP-7250 (semi solid)
EEW = 162 g/eq, η_{RT} = 50,000 Pa.s, T_g = 345°C

Figure 5. *Molecular structures of 3 epoxies. Epon 826 is a common DGEBA epoxy, HP-4032SS is a high temperature liquid, while HP-7250 is a semi-solid. Note that all Tg values are measured using DDS as the curing agent. Refs: [109, 138-140].*

2.2.3. Crosslinking and Evolved Heat

The epoxide equivalent weight (EEW) tells the molecular weight of the epoxy resin per the number of reactive sites. The lower the EEW, the more reactions occur simultaneously leading to more heat produced. This is described by the heat of reaction, ΔH, and can be measured by DSC which chapter 2.2.2 outlined.

Excessive heat can lead to auto-acceleration as the heat from previous reactions initiate further reactions. Although a reaction rate is constant at a given temperature, the exothermic cure reaction coupled with a decrease in the surface area-to-volume ratio traps heat within the bulk material. In a phenomena known as a runaway reaction, this is difficult to stop until all material has been consumed. In 2007, improper scaling produced a runaway reaction at T2 Laboratories in Florida which destroyed the plant and killed four people [141].

Generally, the reaction heat from high temperature epoxies is controlled by limiting applications to thin films where the excess heat can safely dissipate [142]. However, lowering the rate of cure (and heat production) by decreasing the temperature prevents thermal build up and can allow the generated heat to dissipate safely. For AM, this is provided via a low-temperature pre-cure step which also allows the printed structure to maintain shape as the viscosity decreases with temperature.

The EEW can determine the amount of curing agent required. For a reaction to occur, an active hydrogen atom of the curing agent reacts with the epoxide group of the resin. Binks *et al.* determined that an excess of curing agent shifts the reaction onset to lower temperatures [143]. The reverse is also true; a lower content of curing agent shifts the crosslinking temperature higher. However, at low concentrations, the reaction is unable to fully occur and excess epoxide groups can decrease the T_g by acting as rubbery interstitials [144]. Additionally, Minty *et al*. found that improper curing agent to epoxy ratios can result in decreases fiber bonding decreasing strengths of PMC's [145].

Similar to the epoxide equivalent weight, curing agents also have an equivalent weight. For this, the molecular weight of the structure is divided by the number of active reaction initiation sites which are exposed and available to readily react. A 1:1 stoichiometric ratio of curing agent can be calculated by

$$\frac{equivalent\ weight\ of\ curing\ agent}{epoxide\ equivalent\ weight} * 100 = \ \ mass\ of\ curing\ agent\ (pph) \quad (11)$$

to determine the amount of curing agent needed in parts per hundred (pph) of epoxy. Excess curing agent can lead to a quicker reaction and increase the possibility of auto-acceleration.

2.2.4. Impact of Curing Agents

For DIW, inks can be formulated prior to extrusion [6, 37] or mixed at deposition [41, 146]. Based on the type of curing agent, crosslinking can be activated chemically when combined with the resin [41], at elevated temperatures [37], or with an UV light [147] among other methods.

Generally producing lower thermal properties than developed with a thermal cure [148], room temperature curing can reduce energy costs from curing. Further, Rios *et al.* has determined that, for small scale applications or with thin walls, the crosslinking of previous layers can provide additional stability for further material similar to thermoplastic printing, but with reduced warpage and improved inter-laminar strength [146]. However, the cure reaction remains exothermic where Romberg *et al*. has observed that for large scale applications, heat from previously printed material can soften subsequent layers, resulting in bead instability and print failure [41].

Heat and UV-activated curing agents allow for longer working times. Because of the latent systems, inks can be formulated in advance. The degree of latency varies with the system, but Rahmathullah determined that formulated inks at room temperature can have a pot life of over 2 months [149]. Heat activated systems can produce a range of crosslinking densities producing HDT's ranging from 30 [55] to 260°C [47] for a single resin (Epon 828). However, because of the inverse relationship between temperature and viscosity, heat activated curing agents are more prone to failure from the decreased shear yield stress during curing. Recent work has considered a dual UV-heat cure [99, 150]. Inverizzi *et al*. has found that by partially curing (UV) the system during printing, increased print stability was achieved allowing for a 50° print overhang [99]. The heated cure then provided additional mechanical and thermal properties.

This work considers three heat-activated systems: an ionic liquid, dicyandiamide, and a diaminodiphenyl sulfone as depicted in figure 6. The heat activated system allows for a long latency with pot life of several hours at intermediate temperatures.

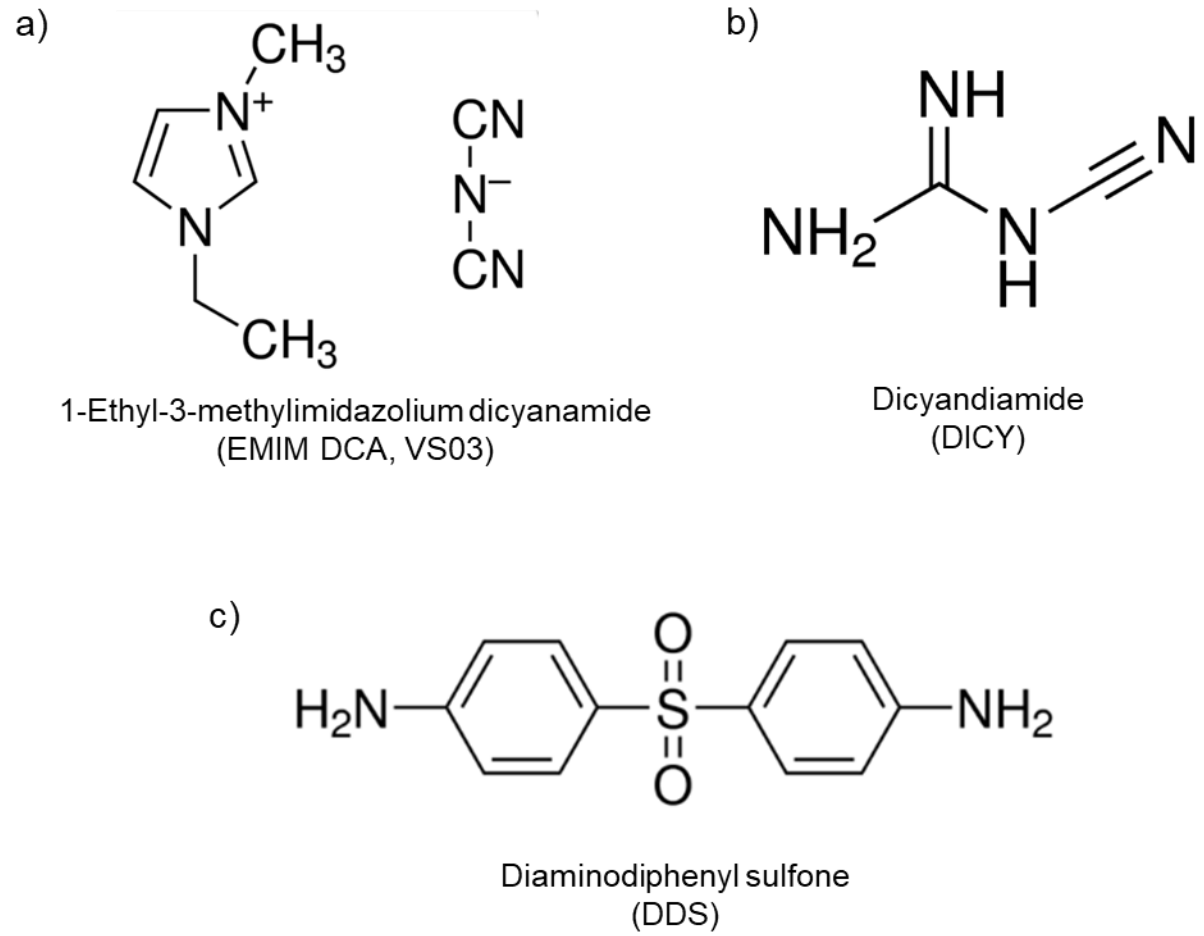

Figure 6. *Three common curing agents. A) 1-Ethyl-3-methylimidazolium dicyanamide (EMIM DCA, VS03), B) Dicyandiamide (DICY), C) Diaminodiphenyl sulfone (DDS). Refs: [151-153].*

1-Ethyl-3-methylimidazolium dicyanamide (EMIM DCA, Basionics VS03)

Basionics VS03 is an imidazolium-based ionic liquid that has shown success as a latent curing agent for printed Epon 826 systems leading to moderate (130 – 155°C) glass transition temperatures [35, 37]. It can be used as the primary curing agent or as a catalyst for a less latent curing agent such as a dicyandiamide. At low loading fractions (6 pph), Neumeyer *et al.* observed a 17 – 35°C reduction in the curing onset temperature measured by DSC at varying heating rates [154]. Work by Rahmathullah *et al*. has determined that for DGEBA-VS03 systems, there is a pot life greater than 60 days and the reaction completes in 20 minutes at 165°C [149]. As such, VS03 is readily accessible and provides sufficient latency required for pre-mixed printing.

Dicyandiamide (DICY)

The second curing agent, the dicyandiamide (DICY), comes as a white powder. DICY is able to be incorporated similar to nanoclay by directly mixing into the epoxy resin [74]. While DICY commonly uses an accelerator to lower the required activation energy, crosslinking occurs quickly above 175°C [155]. Although more energy is required to initiate a reaction than for an imidazole dicyanamide, Hu *et al.* found that crosslinking progressed when lowering the cure temperature to 110°C, but the time to full cure doubled [156]. Work by Thakkar *et al*. showed that although DICY is not an aromatic amine, it produces similar properties by acting as a catalytic curing agent. The thermal stability is imparted by using all four nitrogen containing functional groups to cure resulting in a highly crosslinked structure [47].

Diaminodiphenyl sulfone (DDS)

Diaminodiphenyl sulfone (DDS) also comes as a white powder. Known to produce high crosslinking densities, epoxies from this system can lead to glass transition temperatures 100°C higher than found using an imidazole curing agent [47]. However, DDS has a low solubility and a melting temperature of 175°C [153]. This leads to challenges with dispersion and is commonly found dissolved in solvents [157] or heated and mixed using a rotary evaporator [43, 109]. The patent filed by Blakhaman showed that when incorporated with the liquid prepolymer CY179, the resultant formulation became solid with a T_g of 46°C and a melting point at 76°C prior to curing [158]. As such, despite the excellent properties achievable with DDS, solid resins are unable to be processed via DIW at this time and will not be considered for this work.

2.3. Cure Progression

Because the epoxy systems incorporate a heat-activated crosslinker, care must be taken to prevent curing during processing. Latent curing agents will cure at lower temperatures than optimizal, but at reduced rates [117]. The minimum amount of energy required for molecules to interact and react is described by the activation energy. At each temperature, the activation energy can be used to determine a rate constant [159].

A time-temperature-transformation (TTT) diagram is shown in figure 7 and describes expected resultant properties when varying the two variables for an isothermal cure [117]. The y-axis shows three T_g values as reference points. The first, $T_{g,o}$, is the initial value for the uncured system. Below this point, there is limited chain motion, reaction sites do not interact, and crosslinking is unable to occur. The second, ${}_{gel}T_g$, is the transition temperature after long-range crosslinking has developed. The T_g of the cured system will fall between this and $T_{g,\infty}$ which is the maximum achievable transition temperature.

2.3.1. Gelation

Charlesby determined that a thermoset gels once when each monomer has cross-linked, on average, one time leading to an insoluble network producing long range elastic behavior [161]. While an ASTM standard does exist to determine the gel time [162], it remains arbitrary and based on visual observation. As such, other work has been done to determine gelation by rheometry [117, 163-166]. Winter *et al*. proposes that the gel point is reached when infinite viscosity is observed [166] while Hinrickhs *et al.* defines it at the point where the storage and loss modulus are equal and tan(δ) = 1.0 [163]. Regardless of the measurement technique, gelation marks the onset on solid behavior. At sufficient temperatures, molecules are able to move freely and gelation occurs rapidly. However, if a fiber-filled resin gels too quickly, the fiber wetting properties and resultant fiber adhesion, can be worsened [74].

2.3.2. Vitrification

Vitrification occurs when the glass transition temperature of a system increases to equal the cure temperature [117]. Provided that the cure temperature is below that of the maximum achievable glass transition temperature, the system will continue to crosslinking increasing the thermal properties past this point when provided sufficient energy. At vitrification, the thermoset

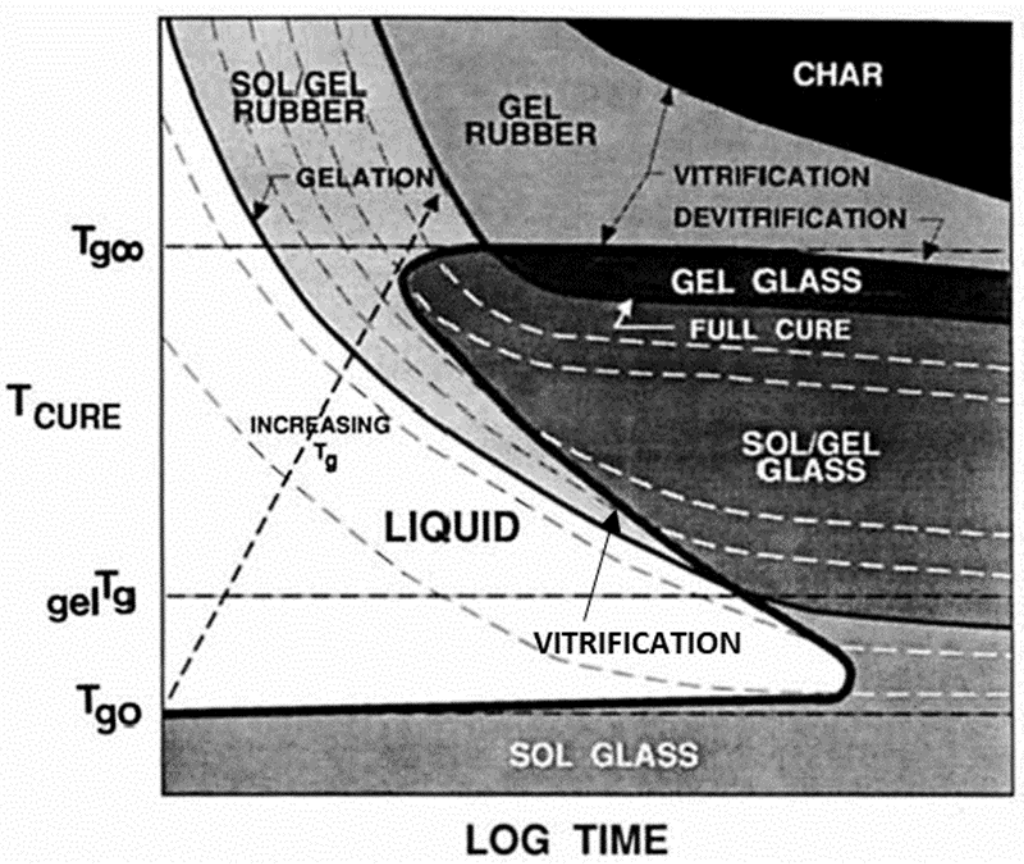

***Figure 7**. Time-temperature-transformation (TTT) isotherm cure diagram for a generic thermosetting polymer [160].*

system remains malleable and processable at higher temperatures, but rigid at lower temperatures [117].

As depicted in figure 7, the vitrification curve is *S*-shaped. If the cure temperature is below ${}_{gel}T_g$, gelation and vitrification occur simultaneously forming a sol-gel glass [117, 165]. At higher cure temperatures, the two occur separately with vitrification increasing long range order from the sol-gel rubber state to a glassy state. Crosslinking continues until insufficient thermal energy is provided, the reactions sites are unable to interact, and the reaction stops prematurely. However, by increasing the cure temperature, the reaction can continue. At cure temperatures above $T_{g,\infty}$, the cure is able to fully progress and vitrification does not occur [167].

When vitrification occurs, it acts as an intermediate to the full cure and largely impacts the reaction rate. Before vitrification, the reaction rate follows chemical-controlled kinetics. After, the reaction becomes diffusion-controlled and slows [156, 160].

2.3.3. Maximum Glass Transition Temperature

Rarely is the maximum glass transition temperature achievable. Enns *et al.* found that competing reactions, steric hindrance, and insufficient time can prematurely stop crosslinking [167]. While no one cure path is "best", the process to develop an optimal cycle is time consuming and expensive [163]. While high temperature, faster cures without intermediate steps can be more straightforward, these can also shock the system where the outer surface cures before the inside structure is heated. This outside-in cure progression can lead to high internal stresses from thermal expansion and cure shrinkage [117].

The phenomena of longer cures producing higher glass transition temperatures and mechanical properties is well documented [116, 160, 167, 168]. Wisanrakkit *et al.* found that after vitrification an additional 18 hours at temperature lead to a 30-50°C increase in T_g which they attribute to the diffusion-controlled nature of the reaction and steric hindrance [160]. This relationship was expanded by Enns and Gillam to state that

$$\frac{d\alpha}{dt} = A\, exp\left(\frac{-E_A}{RT}\right) f(\alpha) f(\eta_L) \qquad 12$$

where α is the extent of the reaction, E_A is the activation energy required to initiate the reaction, and R is the universal gas constant. The function $f(\alpha)$ provides information as to the reaction kinetics and extent of conversion while local viscosity, and diffusion kinetics, are described by $f(\eta_L)$ [117, 167]. The activation energy can be determined through DSC thermograms following Kissinger's methods [127, 128, 169].

2.3.4. Degradation: Char and Devitrification

When thermosetting systems are exposed to high temperatures for extended periods of time, they can undergo char or devitrification; both of which can mark the lifetime of a thermoset. For each resin-curing agent system, this lifespan before degradation varies. Char formation occurs when operated above the glass transition temperature [117]. A high char yield can be an indicator of good flame resistance [170]. When used below the transition temperature for sufficient time, devitrification can break crosslinks and the T_g is subsequently decreased. For high temperature systems, these reactions can interfere with the maximum achievable T_g. Work by Chan *et al.* using trifunctional epoxy-DDS system found that while the calculated maximum T_g was 352°C, the measured results fell at 324°C due to this competing reaction [137]. Using degradation rates, the initial T_g and HDT, Stutz *et al.* determined the relationship between lifetime and service temperature to avoid thermal degradation. From this work, for the selected DGBA epoxy system with an initial T_g of 200°C to maintain a 20-year lifespan, 135°C is the maximum usable temperature [171]. While these values vary between systems and applications, thermal degradation will diminish cured properties provided sufficient time.

2.3.5. Phase Separation

If applicable, phase separation occurs before gelation. When a secondary material – either a filler or non-primary epoxy – is added to the matrix, the two can begin crosslinking at different temperatures or variations in the thermal properties can force material out of the matrix leading to a heterogeneous final structure [117]. This correlates to a non-uniform increase in viscosity leading to intermediate plateaus during the cure as observed via rheology [163]. Poor miscibility can result in multiple glass transition points and dissimilar properties across a cured part [119].

2.4. Processing Requirements

2.4.1. Resin Deposition

Two approaches have been explored for material extrusion printing of nominally solid materials. In the first approach, the solid material is dissolved or suspended in a solvent or carrier fluid. This approach enables deposition at room temperature and encompasses robocasting of ceramic and metal particle suspensions [30] and solvent casting of polymer resins [74]. However, with this approach, the solvent or carrier fluid must evaporate after deposition, which limits applications to thin walls [172] can lead to shrinkage and cracking due to solvent outgassing [173]. In addition, solvents used for polymer resins can present health and safety hazards [174].

A more widely used alternative, particularly for polymer-based systems, is melt extrusion (figure 3.a). In this process, the print head applies heat to liquefy the feedstock material thereby reducing its viscosity and enabling extrusion and deposition. After deposition, the material cools and solidifies. This approach encompasses all of the thermoplastic material extrusion printing technologies, including FFF, FDM, and BAAM as discussed in chapter 2.1. This process is attractive for its commercial maturity, robustness, and minimal post-processing. However, the thermal history in printed parts is complex [41, 98], which can lead to geometric warping, poor layer-to-layer bonding, and interlaminar deboning [94, 175]. For thermoplastics, this is achieved by heating a material above the melting temperature [45]. However, for thermoplastics, care must be taken to reduce the viscosity but not induce cure. For this work, a warmed extrusion process is selected. Because of the required post-processing cure, issues with interlayer bonding, residual stresses, and warping are minimized.

2.4.2. Pre-cure

For DIW of thermally cured inks, an intermediate temperature pre-cure is required for the print to maintain structure. While the formulations can cure at room temperature, this can be on the order of weeks as determined by a materials pot life. Practical time constraints require moderate temperatures to initiate crosslinking. However, the decrease in viscosity can limit build heights.

Work by several authors have found success with a moderate temperature cure around 100°C for 12 – 24 hours for an DGEBA epoxy system [36, 37, 80, 176]. The temperature at

minimum viscosity and time required to achieve vitrification will vary based on the system. Kuman *et al.* noted that slow cures can be mechanically beneficial [177]. During fast cures, the rapid release of heat from the cure exotherm can create hot spots which lead to voids. Mechanically, the pre-cure temperature is less important than the extent of crosslinking. Patel *et al*. showed that, while faster cures presented lower fatigue lives, similar behavior occurred provided the epoxy was able to reach a critical gel point prior to a post-cure [75]. As such, the pre-cure does lengthen the cure time.

The pre-cure also improves the safety of the system. As discussed in chapter 2.2.4, the heat produced by crosslinking remains constant regardless of the cure rate. By lowering the cure temperature, the reaction rate decreases. In turn, the probability of a runaway reaction also decreases. Other methods to minimize the exothermic reaction include adding filler materials to reduce the reaction sites and bulk volume [178] and maintaining thin walls for sufficient heat egress [35].

2.5. Fibers

Generally more expensive than the traditional structural materials (e.g. aluminum or steel alloys), fiber composites are lightweight which saves energy reducing the overall lifetime costs [82]. Although the strength and stiffness are commonly less than traditional materials, the specific strength and moduli improve. The high strength-to-weight ratio makes fiber composites attractive in the automotive [179] and aerospace industries [76] as well as for sporting equipment where lightweight equipment requires less physical expenditure [73]. Generally made with carbon or glass fibers (GF) imbedded into a polymer or ceramic matrix, fiber composites are designed such that the matrix provides support and structure for the fibers which give strength.

Differences in thermal expansion leads to swelling at different rates which can produce pores and poor fiber-matrix adhesion. This is worsened by highly viscous materials [73] or a rapid cure [117]. Fiber composites are commonly vacuum sealed to prevent this [180, 181]. However, one of the strengths of AM is the lack of mold required. As such, vacuum sealing a printed part would negate the benefits of printing.

2.5.1. Types of Fibers

Carbon and glass fibers are commonly selected for thermoset composites. Carbon fibers are commonly employed when high performance properties are required. Currently, work on printed fiber-reinforced thermosets predominantly focuses on carbon fiber composites to improve mechanical strength [27, 49, 85, 97, 99] of printed components and thermal properties [98, 105]. In one such example, Wang *et al.* utilized carbon's electrical conductivity to produce a flexible, printed wearable lithium ion battery [182]. Work by Mishhaevky *et al.* observed that when using carbon fibers in an epoxy matrix, fibers improved the modulus by 57% although this correlated to a 44% reduction in strain at failure [183]. This reduction in strain along with their high cost, can limit applications. Alternatively, glass fibers are less expensive and have a higher strain-to-failure than carbon.

Glass fibers come in two main categories: E-glass and S-glass. More common, E-glass is named for its electrical insulation properties and has good strength, stiffness, and weathering properties. S-glass is more expensive than E-glass, but has a higher moduli and thermal resistance. Glass fibers are unique among fibers because its properties are isotropic [73]. This becomes important for AM applications as processing causes high shear stresses which can break fibers. However, when the fibers rub against each other, they can fracture the strands causing surface cracks which diminish the strength. Additionally, glass fibers are IR transparent, making them attractive for applications such as radomes [184].

Fiber properties are compared in table 2**.** However, processing and thermal history impact the properties. The values included in the table are not all-inclusive.

2.5.2. Fiber-Matrix Adhesion

The fiber-matrix adhesion determines the effectiveness of a fiber to strengthen a composite. Stronger interfacial bond strengths allow for higher load transference from the matrix to fiber which determines the strength of the composite [73]. As such, significant work has been done to improve fiber-matrix bonding by modifying the fiber surface [190, 191], the matrix content [192], and examining the degree of cure [168, 193]. It has been shown that for matrix epoxies with high viscosities, there can be reduced fiber-matrix adhesion [74]. This leads to voids that become more common with increasing fiber content [73, 194]. With AM, voids are more probable than other manufacturing methods with material being placed layer-by-layer. Figure 8 depicts

Table 2. *Selected property comparison of carbon, E-glass, and S-glass. Refs: [73, 185-189].*

		Carbon	E-Glass	S-Glass
Density (g/cc)		1.44 - 1.95	2.54 - 2.60	2.46 - 2.49
Modulus (GPa)	parallel to axis	240 - 525	72 - 85	85 - 93
	perpendicular to axis	12 - 20	72 - 85	85 - 93
Strength (GPa)		2.9 - 5.3	1.9 - 3.2	4.5 - 4.9
Failure Strain (%)		0.5 - 1.8	1.8 - 4.8	5.4 - 5.7
CTE ($x10^{-6}$ °C)		-1.2 - 0 (parallel) 7 - 12 (radial)	4.9 - 5.4	2.8 - 5.6
Thermal Conductivity (W/m-°C)		24 - 105	1.0 - 1.35	1.2 - 1.45

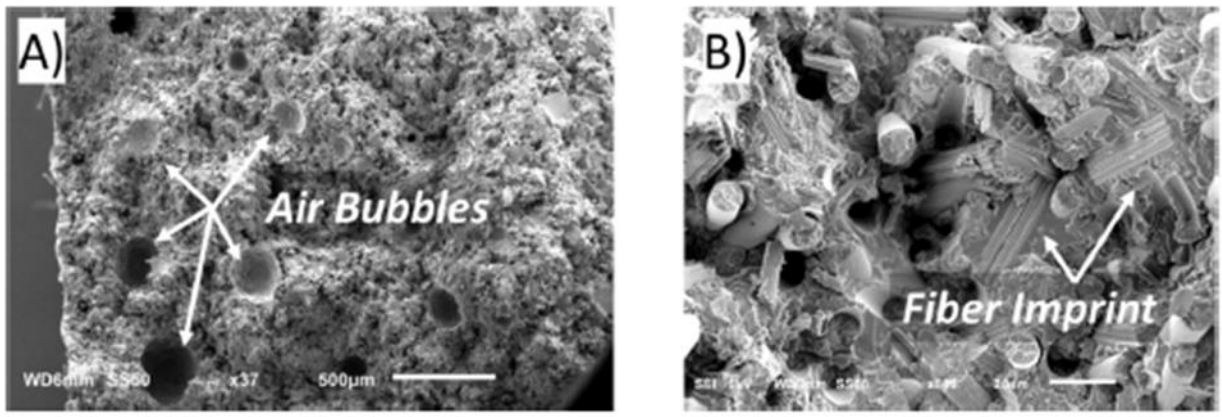

Figure 8. *Effect of printing on fibers. A) pores caused from air bubbles during printing and B) highly oriented fibers in the print direction [80].*

both voids formed during printing of an epoxy-carbon fiber composite (A) and fiber orientation and bonding (B).

2.5.3. Fiber Length and Orientation

Although long fibers yield superior mechanical properties compared to short fibers, processing requirements (e.g. deposition height, small corner radii, and nozzle clogging) prevent them from being readily usable in AM applications [80]. By following a mixing method to disperse fibers, the fiber interactions lead to fibers breakage. While a higher volume of shorter fibers can be added, more load can be transferred to fibers longer than a critical length, producing greater property improvements [49]. The critical length, depicted in figure 9, is determined by the fiber strength, diameter, and fiber-matrix interface and describes the transfer of load from the matrix to the fibers. While a higher volume of short fibers can increase the modulus, strength improvements only occur when the applied load is able to transfer from the matrix to the fibers. The minimum length, l_c, that load transference occurs can be calculated by [195, 196]

$$l_c = \frac{\sigma_f d}{2\tau} \qquad 13$$

where σ_f is the fiber strength, d is the fiber diameter, and τ is the interfacial shear strength between the fiber and matrix. This can be approximated by assuming that the interfacial shear strength is equal to the shear strength of the matrix following a von Mises yield criterion such that

$$\tau = \frac{\sigma_m}{\sqrt{3}} \qquad 14$$

and

$$l_c = \frac{\sigma_f d\sqrt{3}}{2\sigma_m} \qquad 15$$

where σ_m is the matrix strength. Because AM orients material during printing which can lead to variations in the matrix yield strength, Pierson *et al.* averaged the 0 and 90° print direction strengths to simulate isotropy [49]. For fibers shorter than the critical length, less load

transference is achieved and the strength decreases. Work by Ohsawa *et al.* found that for an epoxy – E-glass composite, the shear stress between the matrix and fiber is inversely related to temperature, which increases the critical fiber length as the temperature increases [197]. This was credited to a decrease in the matrix shear strength at elevated temperatures and a relaxation of thermal stresses which held fibers at low temperatures.

2.5.4. Printed Fibers

The majority of work done on printed thermoset-fiber systems has studied carbon fibers [27, 49, 80, 85, 198]. While carbon fibers do present superior strengths and moduli than glass fibers, they are anisotropic and brittle in the off-axis direction making them fragile prior to being included in a matrix. Using a similar resin and mixing schedule followed in this work, Pierson *et al*. measured a 95% reduction in carbon fiber length after incorporation into epoxy [49]. By using glass fibers, less breakage during processing is expected as the fibers can adsorb more impact before fracture. However, even if the fibers do not fracture during mixing, the fiber impact can still cause surface defects which decrease properties [73, 199]. Because glass fibers maintain their initial length, shorter fibers must be used than previously determined. With carbon fiber, chopped tape can be employed with the mixing time controlling the length distribution. For glass fibers, milled fibers are sized by bulk density leading to variation in fiber length distributed around some average. As such, some fibers are shorter than the critical length.

Unlike injection molding epoxy-fiber composites, AM requires a constant flow rate for longer periods of time. Agglomeration of the fibers in the extrusion nozzle can be detrimental and prematurely terminate flow [94, 200]. Recent work by Nawafleh and Celik employed a vibrational extrusion system to reduce fiber clogging during extrusion which allowed for a 46 vol% carbon fiber-epoxy ink to extrude through a 0.84 mm nozzle. Despite using short (50 μm) fibers, they achieved 70% of the calculated strength for long fibers which they credited to the highly aligned fibers reaching a percolation threshold [80].

Fibers must bend when exiting the nozzle to become a printed road as shown in figure 10. This limits the fiber lengths that are able to be processed, decreasing the available property space. Nawafleh and Celik note that for fibers with high aspect ratios, fiber agglomeration and nozzle clogging become more prevalent [80]. Although short fibers yield reduced strengths when compared to continuous, they provide favorable processing conditions for AM.

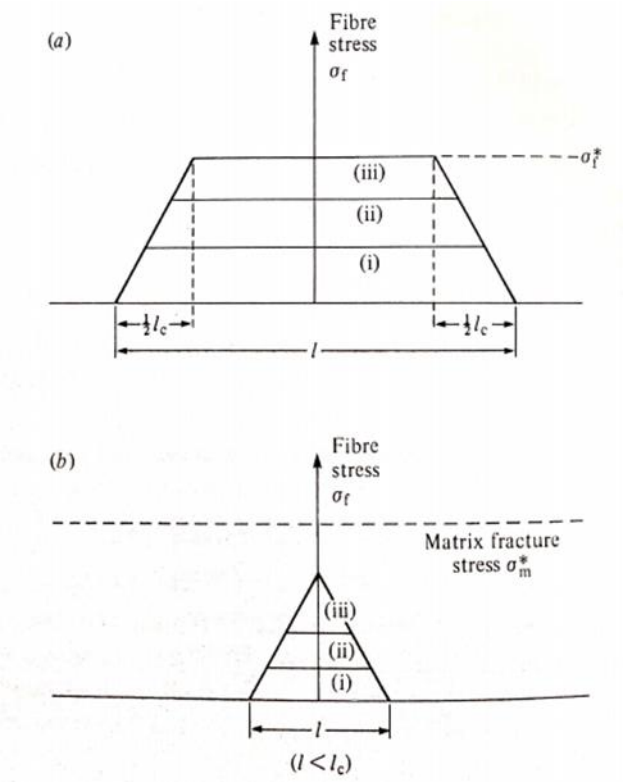

Figure 9. *Load transference and fiber length. The critical fiber length, when applied force is primarily carried by the fibers, is determined by the fiber strength, diameter, and fiber-matrix interface [73].*

During printing, Takinalp *et al*. measured a 91.5% alignment of short fibers in the print direction [85]. Thermoplastic work by Es-Said *et al*. found that mechanical strengths along the printed path were 55% higher than when tested at an 90° angle which they believe to be the result of directional processing and poor interlayer bonding [201]. Although this occurs less in thermoset AM due to stronger interlayer bonding, fibers impose directionality that must be considered [85, 202]. Recent work by Hmeidat *et al.* [97] quantified the mechanical strengths correlating with fiber orientation through an anisotropy factor following

$$\psi = \frac{M_{0^\circ}}{M_{90^\circ}} \qquad 16$$

which is the ratio of properties, *M*, in the two directions. This work determined that both smaller nozzle diameters and faster print translation rates induce higher degrees of anisotropy. Knowing the anisotropy relationship allows for customized parts that take advantage of the differing properties [203, 204].

Some success has been accomplished printing with continuous fibers. Work by Li *et al.* (thermoplastics) [205] and Hao *et al.* (thermosets) [198] have both successfully printed with continuous fibers. However, continuous fibers are unable to execute sharp corners without breaking, limiting the design freedom additive manufacturing is known for, must extrude slowly (3 mm/s by Hao *et al.* [198] as compared to 30 mm/s for short fibers by Hmeidat *et al*. [37]), and are less robust that short fiber systems. An industrial printer was developed by Markforged which allows for extrusion of carbon fibers, fiberglass, and Kevlar [206]. To maintain design freedom and reduce complexity, short fibers are considered in this work.

2.6. Fiber Composite Models

2.6.1. Mechanical models

There are several models that can describe the fracture behavior of these systems. The first two assume continuous, unidirectional fibers which leads to an equal strain approximation when force is applied along the fiber direction and equal stress when the load pulls transverse to the fibers [73]. Following an equal strain assumption, the Voigt model, more commonly referred to as the rule of mixtures (ROM), provides the upper limit following

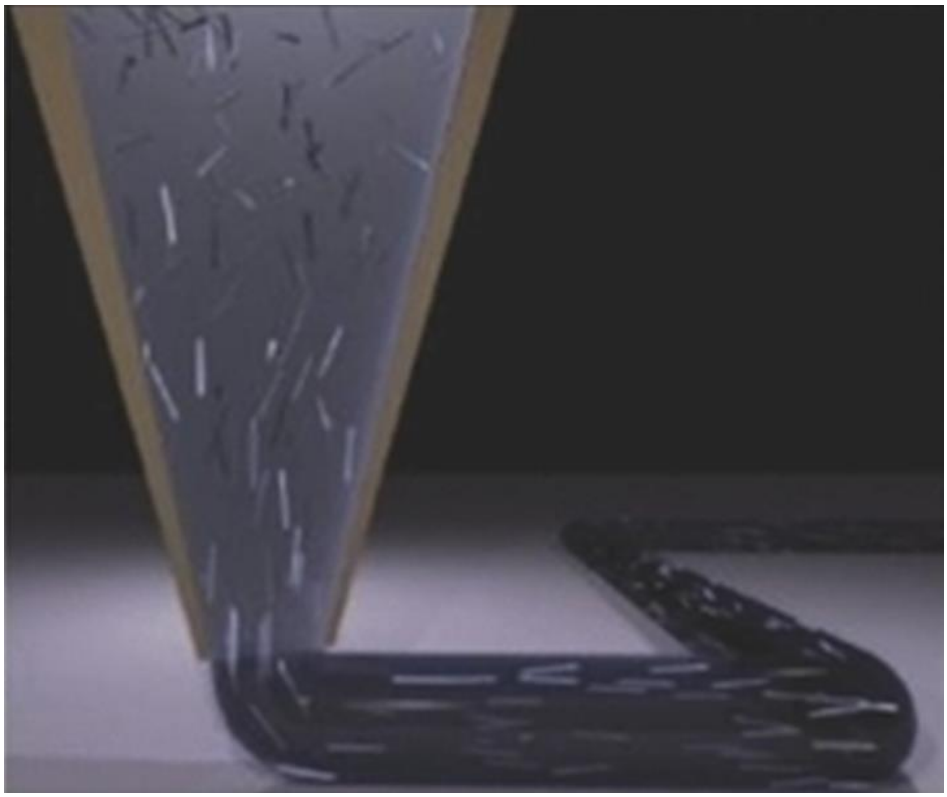

Figure 10. *Fibers becoming aligned during material extrusion [35].*

$$\bar{M}_U = V_f M_f + (1 - V_f) M_m \quad 17$$

where *M* denotes the modulus and *V* is the volume fraction. The subscripts *f* and *m* denote the fiber or matrix properties respectively while the bar signifies a composite property. The subscript *U* indicates that ROM calculates the upper limit. The lower limit, $\bar{M}_L$, is given by

$$\frac{1}{\bar{M}_L} = [\frac{V_f}{M_f} + \frac{(1-V_f)}{M_m}] \quad 18$$

following the same nomenclature. However, these models assume continuous fibers which can limit the applications.

The Halpin-Tsai equations are a common short-fiber model which can be applied to a generic property, *P*, that applied to the bulk and shear moduli as well as Poisson's ratio [207]. Here, the composite properties can be calculated by

$$\frac{\bar{P}}{P_m} = \frac{1+ \xi\eta V_f}{1- \eta V_f}. \quad 19$$

where

$$\eta = \frac{(P_f/P_m) - 1}{(P_f/P_m) + \xi} \quad 20$$

and ξ is a constant related to the geometry of the filler. While ξ can be determined experimentally, it is related to the shape factor. Work has been done to model these values which vary based on the modulus being examined and the loading direction as cataloged by Halpin *et al*. [207]. However, when determining the moduli,

$$\xi_{E_{xx}} = 2(a/b)\,. \quad 21$$

When the fibers are aligned in the *x*-direction (tested axially), *a* is the fiber length and *b* is the fiber diameter. However, when fibers are aligned in the *y*- or *z*-direction, both *a* and *b* are the fiber diameter and $\xi = 2$. Halpin-Tsai assumes that all fibers are oriented [207].

Additive manufacturing does not allow for parts to be vacuum sealed during curing to prevent pores. Further, because AM builds a part layer-by-layer, voids can be created from insufficient flow during extrusion [67, 92] although this is more common in thermoplastic applications [49]. Voids and pores reduce mechanical properties. Considering the Halpin-Tsai model, a shape factor of 0 is assigned to pores. However, this does not account for shape, distribution, or the type of deformation occurring [207]. Rather, an approximation of the reduction in modulus from pores has been developed by Boccaccini *et al*. such that [208]

$$E_{m,eff} = E_m \left(1 - V_p^{\frac{2}{3}}\right)^{1.21\,s} \qquad 22$$

where the effective matrix modulus, $E_{m,\,eff}$, is a factor of the initial matrix modulus, E_m, the volume of pores, V_p, and a scaling factor, *s*, which is defined by

$$s = \left[\frac{z}{x}\right]^{1/3} \sqrt{1 + \left(\left[\frac{z}{x}\right]^{-2} - 1\right) cos^2\alpha_p} \qquad 23$$

Where z/x gives the axial ratio of pores and $cos^2\alpha_p$ describes the pore orientation. For spherical, randomly aligned pores, z/x = 1 and $cos^2\alpha_p$ = 0.33 respectively. Note that this relationship has been developed with V_p = 0.75 as the upper limit.

2.6.2. Testing Methods

Tensile testing of brittle materials is difficult due to machining challenges and stress concentrations leading to premature failure [209, 210]. As such, all mechanical tests are conducted using a 3-point bend geometry. However, surface defects and voids from insufficient flow during printing or post-processing are more apparent for flexure testing as they act as stress concentration points. Work by Swaminathan *et al*. observed a 38% increase in modulus after polishing samples which could then be improved an additional 25% by continuing to machine the top and bottom surface [211]. Similar work by Brenbaum *et al*. determined that surface defects

can decrease the strength by 50% by acting as stress concentrations and fracture initiation points [209]. Because printing imposes a rough upper surface, proper machining is critical to observe material properties. When compared to traditional machining, additive manufacturing creates near-net parts reducing the amount of post-processing required and material waste produced.

Flexure testing generally yields higher strength and moduli values than tensile. Bullock observed a 35 – 50% increase in strength which was accounted for by the non-uniform stress distribution of the sample experiencing both compressive and tensile forces [212]. Upon application of a load, the top surface experiences a compressive force while the bottom experiences tensile. Because the free volume decreases under compression loading, the material is able to support more load than in tension [210]. As such, failure occurs along the bottom surface [213]. Shear effects are possible from this configuration. However, this can be minimized by maintaining a 15:1 span to depth ratio [211].

2.6.3. Thermal Models

Although fibers can interfere with crosslinking and modify the crosslinking density, this effect is minimal, and thermal phase changes and transitions are not impacted by the fiber loading content [214]. However, fibers can improve the moduli and strength of a composite at elevated temperatures. Because the heat deflection temperature is related to the modulus, the presence of fibers can increase thermal dimensional stability. Work by Zhang *et al.* observed a 20°C raise in HDT with the addition of basalt fibers regardless of the loading fraction [215].

As the temperature increases, the critical fiber length does as well. Ohsawa *et al.* observed a linear decrease in the shear strength at the fiber-matrix interface as temperature increased [197]. Although fibers continue to strengthen the matrix at elevated temperatures, they do so with diminishing returns until the glass transition temperature where the increased matrix mobility lessens the impact of the fibers.

CHAPTER THREE
HIGH TEMPERATURE EPOXY SELECTION

This section evaluates six high temperature epoxies for printing requirements. This work is not to be published.

3.1. Abstract

A printable, high temperature epoxy is desirable for improved design freedom in aerospace, automotive, and autoclaving mold applications [2, 4, 77, 179]. However, the definition for "high temperature" varies and many epoxies that achieve a glass transition temperature above 200°C are solid. Five resins were selected and evaluated for their thermal properties and printability. Although the curing agent plays a large role, only one was considered for simplicity. Of the five, only Epiclon HP-7250 from DIC yielded a T_g > 200°C although with an unfilled room temperature viscosity of 100,000 mPa.s, the resin remains too thick to extrude. Additional modifications will be required for a printable material.

3.2. Materials and Methodology

3.2.1. Materials

Five epoxy resins were used in this study: Duralco 4460 (4460, Contronics Corp., Brooklyn, NY), EP17HT (Master Bond, Hackensack, NJ), and Epiclon HP-6000, HP-4032SS, and HP-7250 (DIC Corporation, Japan). These resins were selected for their thermal properties, viscosities, and availability. Other resins were considered and can be found in appendix A. 1-Ethyl-3-methlimidazolium dicyanamide (EMIM DCA, Basionics VS03, Sigma-Aldrich, Inc. St. Louis, MO) was used in stoichiometric amounts based on the resin EEW as calculated using eq. 11 for the Epiclon resins**.** 4460 included both resin and hardener and EP17HT was a one-part system. Garamite 7035 nanoclay (BYK-Chemie GmbH, Wesel, Germany) was used as the only rheological modifier.

Relevant information, including the cure cycle, viscosity, and T_g, are included in table 3. Duralco 4460 was promoted as a "high temperature, low viscosity epoxy" with a working temperature up to 600°F (315°C), primarily for coating applications that require chemical,

electrical, and moisture resistance. At $600/30 cc of resin, Master Bond EP17HT was the most expensive resin tested and claimed a T_g of 220 – 225°C and a working temperature of 340°C. It was refrigerated prior to use to prevent curing and presented a high viscosity at room temperature. A solid, liquid, and semi-solid resin were chosen from DIC's Epiclon line. HP-6000 came as solid pellets that were approximately 3 mm in diameter with 80°C as the softening point. Of the solid epoxies considered, HP-6000 presented the lowest softening temperature. Had promise been shown, other solid resins would have been explored. With a RT viscosity of 1,000 mPa.s, HP-4032SS the lowest viscosity of a resin that met the target temperature. Despite this, the uncured material would separate at ambient temperature (~23°C) which could be reversed via heating. As a semi-solid with a high T_g, HP-7250 was chosen to bridge the gap between low temperature liquid resin and high temperature viscous resins. Note that curing agent varies across the systems. Molecular structures of HP-4032SS and HP-7250 were shown in figure 5.

3.2.2. Formulation

All inks were mixed using a centrifugal planetary mixer (Speedmixer, FlackTek, Inc., Landrum, SC). While the procedure varied due to different requirements from the resins (see table 4 for specifics), the general outline is as follows. The resin and curing agent were mixed for 1 – 2 minutes. Nanoclay was incrementally added until the ink maintained stiff peaks off the edge of a spatula. Between each mixing step, the walls of the mixing container were scraped with a spatula. The final formulation was remixed under 0.1 atm vacuum.

Additional steps were required for solid HP-6000 and viscous HP-4032SS and HP-7250. HP-6000 epoxy beads were first dissolved in 150 pph acetone (Fisher Scientific, Waltham, MA) using a magnetic stir bar (Fisher Scientific, Waltham, MA) at 400 - 500 rpm until fully dissolved. Clay and curing agent were then added to the solution as before. These inks were not mixed under vacuum, but were left in a desiccator (McMaster-Carr, Elmhurst, IL) overnight to remove excess gas and solvent.

Both HP-7250 and HP-4032SS were heated to 80°C in an oven prior to mixing. The decreased viscosity made clay incorporation possible.

Table 3. *Epoxies considered in this study. Refs: [107, 109, 110, 216 – 219].*

Epoxy	Curing Agent	Cure Cycle (°C / h)	RT Viscosity (mPa.s)	T_g (°C)	EEW (g/eq)
Contronics Duralco 4460	2 part system	120°C / 6 h	1,600	"high temperature 315°C"	-
Masterbond EP17HT	1 part system	150°C / 5 h + 177°C / 24 h	15,000 - 25,000 (@ 75°C)	220	-
DIC Epiclon HP-6000	phenol novolac	200°C / 1.5 h	Solid	220	250
DIC Epiclon HP-4032SS	4,4' -Diamino-diphenylsulfone (DDS)	150°C / 1h + 180°C / 3 h	1,000	212	143
DIC Epiclon HP-7250	4,4' -Diamino-diphenylsulfone (DDS)	150°C / 1h + 180°C / 3 h	100,000	345	162

Table 4. *Mixing parameters of all blends. Viscosity measurements come from technical data sheets. Clay was added in parts based on the number of sets listed in row 7 (ie, 12 pph clay in 3 sets = 4 pph clay added at a time)*

	Duralco 4460	EP17HT	HP-6000	HP-4032SS	HP-7250
Viscosity (mPa-s)	1,600	15,000 - 25,000	solid	1,000	semi-solid
Dissolve in acetone	N/A	N/A	Yes 3:1 acetone:resin	N/A	N/A
Heat in oven	N/A	N/A	N/A	Yes 80°C	Yes 80°C
pph VS03	N/A	N/A	5	5	5
mix with planetary mixer	1500 rpm 1 min	1500 rpm 2 min	N/A	1600 rpm 2 min, 0.1 atm	1600 rpm 2 min, 0.1 atm
pph clay	12	10	10	0	0
mix with planetary mixer	3 sets. 1500 rpm 1 min 0.1 atm	2 sets. 1800 rpm 2 min, 0.1 atm	2 sets. 1300 rpm 1 min,	N/A	N/A
Remix in planetary mixer	1500 rpm 2 min, 0.1 atm	1800 rpm 3 min, 0.1 atm	1300 rpm 2 min, 0.1 atm	1600 rpm 2 min, 0.1 atm	1600 rpm 2 min 0.1 atm

3.2.3. Evaluation

Inks were evaluated based on the glass transition temperature, cure behavior, and processing viability. Differential scanning calorimetry (DSC, TA Instruments Q20, New Castle, DE) was used to determine the glass transition temperature and cure behavior prior to the addition of nanoclay. Tests were run on 10 ± 2 mg samples in aluminum pans at a heating rate of 10°C/min from ~20°C to 300°C in a nitrogen environment. To observe the cure behavior, uncured ink was used with open pans to prevent movement during outgassing. The T_g was measured on samples that had been cured following the manufacture recommendation (see table 3) tested in sealed pans. The heat evolved during the cure, ΔH, was determined by calculating the area under the curve using a linear baseline. The glass transition temperature was measured using the midpoint method. In addition to DSC, the cure behavior was examined visually. For all but HP-4032 which was too viscous, nanoclay was incorporated and the ink was pre-cured at a low temperature mimicking a printed cure cycle. Success was determined by retention of surface details.

Processing viability for DIW was determine qualitatively based on a series of questions. 1) How many extra steps were required to mix the ink? 2) How long did it take to mix the ink? 3) Was nanoclay able to be incorporated? 4) Can the ink readily print? Of the three evaluation factors, processing was the least important as scaling up the process would likely use a different blending protocol.

3.3. Results

The results of DSC are shown in figure 11 and listed in table 5 along with nanoclay-filled cured prints shown in figure 12. Duralco 4460 yielded a T_g of 185°C, 15°C below the requirement. Although the ink presented an elevated viscosity, the resin was able to incorporate 12 pph nanoclay and maintain shape after curing as depicted in figure 12.a.

Despite requiring no additional formulation, EP17HT obtained a T_g of 195°C, 25°C lower than the expected value. A moderate (347 J/g) exothermic reaction was produced with the reaction peak occurring at 225°C. At 80°C, a low temperature softening behavior was observed. After incorporating 10 pph clay, figure 12.b demonstrates success with maintaining surface details when cured. However, the high cost eliminated it from further testing.

The solid resin, HP-6000 was dissolved into acetone for the addition of curing agent and clay. Testing was conducted after 90% solvent by weight had been removed via a vacuum

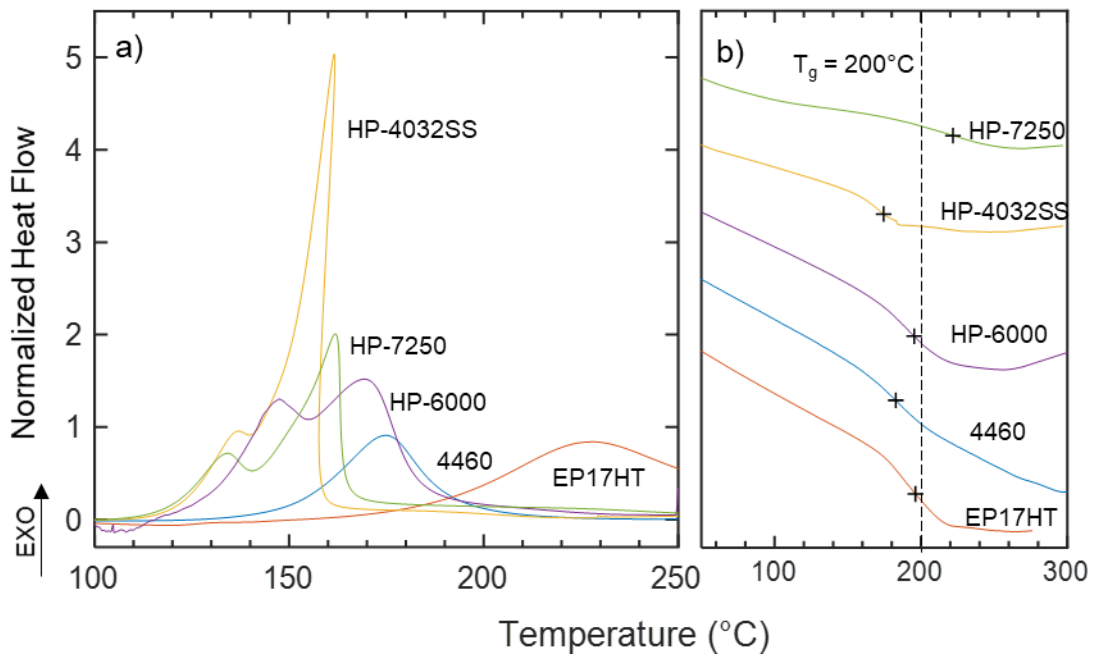

***Figure 11**. DSC thermograms of selected epoxies cured with VS03. The exothermic cures are shown in (a) while (b) depicts the glass transition temperatures*

***Table 5.** Cure properties of resins cured with 5 pph VS03 without clay.*

Epoxy	EEW (g/eq)	ΔH (J/g)	T_{peak} (°C)	Cure (°C/ h)	T_g (°C)
Duralco 4460	-	240	175	120°C / 6 h	185
EP17HT	-	347	225	150°C / 5 h + 177°C / 24 h	195
HP-6000	250	354	145, 170	200°C / 1.5 h	185
HP-4032SS	143	665	135, 162	150°C / 1h + 180°C / 3 h	175
HP-7250	162	555	137, 162	150°C / 1h + 180°C / 3 h	220

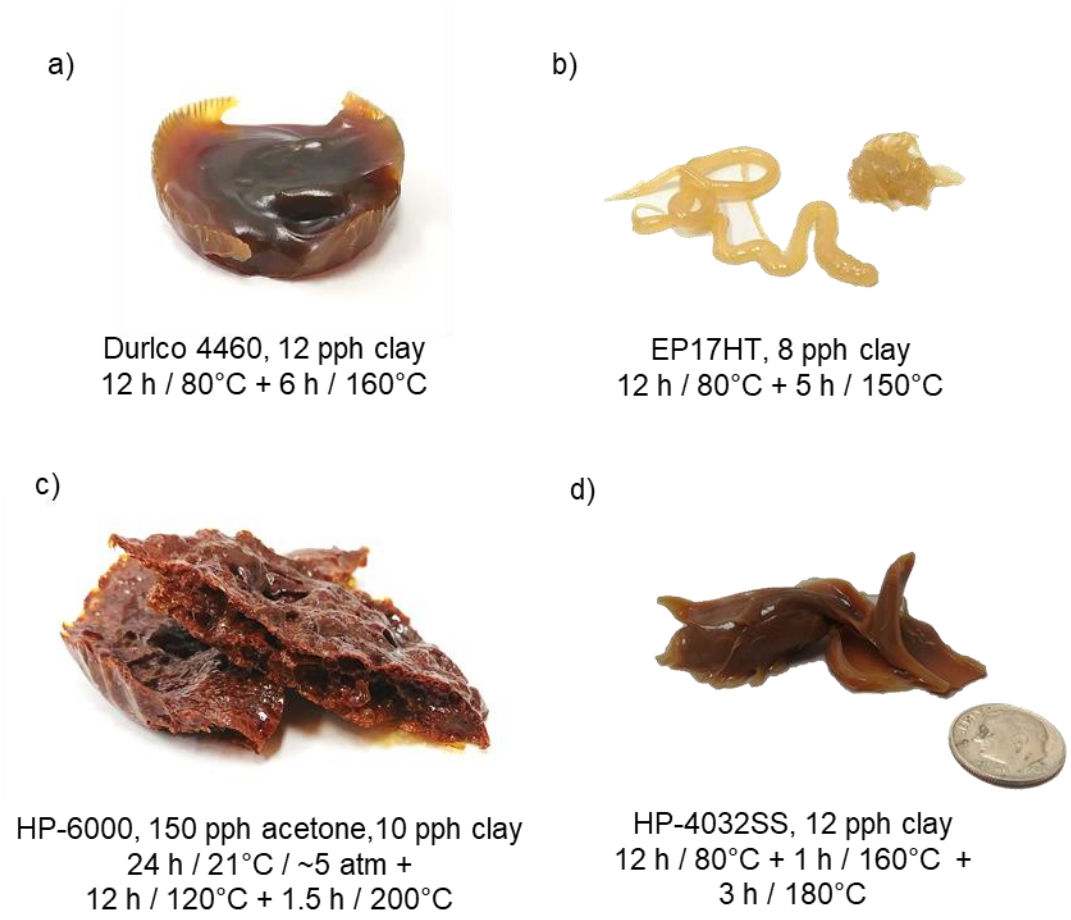

Figure 12. *Epoxy + clay. Cure included a pre-cure followed by the manufacture recommendation. Dime is included for size reference.*

chamber. While this also had an expected T_g of 220°C, the curing agent was varied from the manufacture recommendation, leading to 195°C from the VS03 system. Here, two exothermic peaks were observed at 145 and 170°C suggesting a 2-step reaction which produced 354 J/g of heat. At 110°C, a melting curve is observed.

Although HP-6000 had a lower T_g than required, the solvent nature of this system could allow for other curing agents, such as DDS, to be incorporated. However, despite removal of 90% of the acetone, the remaining solvent outgassed during the cure producing an uncontrolled foam as seen in figure 12.c. At this time, the solution is required for clay and curing agent to be incorporated. As such, solid epoxies are unable to be considered.

As a high-temperature liquid resin, HP-4032SS required the highest crosslinking density to reduce the free volume. This produced 665 J/g of energy during the cure. Again, two distinct exothermic peaks appeared at 135 and 162°C with a third, gradual slope from 175 to 220°C before returning to the baseline. Although HP-4032SS held form well (figure 12.d), at 183°C, the epoxy did not reach the required temperature threshold.

Of the resins, only HP-7250 obtained a Tg above 200°C at 220°C. However, this ink is too viscous to incorporate nanoclay. Similar to HP-4032SS, there are two reactions occurring that present peaks at 137 and 162°C. However, at 555 J/g, HP-7250 releases 16% less heat. For the Epiclon resins, the reduced T_g can be accounted for by the change in curing agent.

3.4. Discussion

The phrase “high temperature” presents a moving target making it difficult to find resins that are appropriate. This is best demonstrated with Duralco 4460. Rather than providing the T_g, the heat deflection temperature was given (260°C) along with 315°C as the upper working temperature. However, no criteria were provided to describe this upper limit. Although the measured T_g of 185°C was lower than expected, this fell within the range for marketed high temperature epoxies. For many applications, 180°C is sufficiently high.

The glass transition temperature measures a change in the molecular structure that occurs over a range of temperatures which can vary among test methods as discussed in chapter 2.2.2. Although less accurate, DMA of cast samples provides a measure of bulk properties and often a higher value.

Several additional solid resins were found with T_g values above that of HP-6000. However, the failure of HP-6000 discouraged additional iterations of solid resins. While a solvent could work for an ink with defined escape path, such as a syntactic foam, they are not feasible for this method.

At 220°C, HP-7250 is the only resin from the five candidates the presented the required glass transition temperature. However, even after heating, this formulation remains too viscous to incorporate nanoclay. As such, a blend of two resins, HP-7250 with the lower T_g liquid resin HP-4032SS will be required to reduce the viscosity for use in DIW AM. Further, the flexibility of curing agents for HP-7250 allows for additional improvements in the glass transition temperature.

3.5. Conclusions

Five resins were selected for their thermal properties; of these, only HP-7250 achieved a T_g > 200°C as desired. However, HP-7250 (T_g = 220°C), was too viscous to flow or have clay incorporated and is unable to be used for DIW AM in the as-received state. To achieve the required flow behavior, HP-7250 will have to be blended with a second resin to reduce the viscosity allowing for nanoclay to be incorporated. A heated extrusion system will also be required.

Slurry-based systems were explored. This would allow for high T_g solid pre-polymers to incorporate the required fillers and print. However, when curing, the solvent had no viable escape path and resulted in an uncontrolled foam. As such, solid pre-polymers are not viable at this time.

CHAPTER FOUR
DEVELOPMENT OF 6040 EPOXY FEEDSTOCK

Disclosure: This work is to be published in *Additive Manufacturing* (target: fall 2020). This work was completed and written alone with feedback from the projects PI, Brett Compton.

4.1. Abstract

Additive manufacturing, which allows for design and geometric independence while reducing material waste by producing near-net shape parts, has been employed to build polymeric lightweight, hollow custom molds, cars, and robotic components. However, these materials have a maximum working temperature that prevents autoclaving, engine, or aerospace applications where the design freedom allowed could be beneficial. Because of the shear thinning and bulk cure requirements of 3-D printing, not all materials are able to be formed this way. This work combines a high-temperature, high-viscosity resin with a lower viscosity resin to produce the flow properties required while maintaining a high working temperature as determined by the glass transition temperature (T_g). The thermal flow and cure properties were evaluated allowing for a warmed extrusion method to be employed. This ink presented a T_g of 210°C, flexure modulus of 4.26 GPa and strength of 130 MPa along the print direction.

4.2. Materials / Methods

4.2.1. Materials

Three epoxy resins were used in this study: Epiclon HP-7250, Epiclon HP-4032SS (DIC, Japan), and Epon 826 (Momentive Specialty Chemicals, Inc. Columbus, OH). Epiclon HP-7250 is a high-temperature, semi-solid resin with a room temperature viscosity of 60,000 Pa-s, T_g of 225°C, density of 1.2 g/cc, and EEW of 162 g/eq. HP-4032SS is a lower-temperature liquid resin with a room temperature viscosity of 12 Pa-s, T_g of 185°C, density of 1.2 g/cc and EEW of 170 g/eq. The two Epiclon resins were blended to obtain an extrudable viscosity while maintaining thermal properties. As a reference for printable epoxy behavior [35, 220], Epon 826 is a Bisphenol A diglycidyl ether (DGEBPA) with a density of 1.162 g/cc and EEW of 180 g/eq. 1-Ethyl-3-methylimidazolium dicyanamide (EMIM DCA, VS03) was used as a latent, heat activated curing agent (Basionics, Sigma-Aldrich, Inc. St. Louis, MO). Chemical structures of each were shown in

figure 5. Garamite 7035 nanoclay (BYK-Chemie GmbH, Wesel, Germany) was added as a rheological modifier.

4.2.2. Methodology

To determine the optimal blend of HP-7250 and HP-4032SS, six blends - 100 HP-7250/0 HP-4032SS, 75/25, 60/40, 50/50, 25/75, and 0 HP-7250/100 HP-4032SS – were formulated. The resins were heated to 80°C using a HERATherm oven (Thermo Scientific, Waltham, MA) and measured to the appropriate ratios. The blends were mixed at 1600 rpm for 1 minute using a centrifugal planetary SpeedMixer (FlackTek Inc. Landrum, SC). Viscosity measurements were taken on the blends and Epon 826 without the addition of curing agent using 25 mm parallel plates with a gap of 0.5 mm and a frequency of 1 Hz on a Discovery HR-2 Rheometer (TA Instruments, New Castle, DE). These tests were conducted at a constant stress of 20 Pa from ~21°C (ambient lab temperature) to 160°C at a rate of 10°C/min.

Next, 5 pph VS03 was added and mixed twice for 4 minutes at 1800 rpm and 0.1 atm. Cure analysis was conducted by casing 16 ± 2.5 mg samples were into DSC aluminum pans. Two sets of DSC cure and T_g analysis were run. The first was on uncured samples in open pans to prevent movement during outgassing. The cured samples (12 h / 160°C + 6 h / 200°C) were broken into pieces in sealed pans. These tests were both conducted with a heating rate of 10°C/min from RT to 300°C in a nitrogen environment using a DSC Q20 system (TA Instrument, New Castle, DE).

Printable inks were formulated by combining a 60/40 ratio of HP-7250 / HP-4032SS and 14 pph nanoclay. The nanoclay was added in 2 sets and that were mixed at 1600 rpm for 2 minutes after each. This was remixed under vacuum at 0.1 atm following the same schedule. Lastly, 5 pph VS03 was added and mixed twice for 4 minutes at 1800 rpm and 0.1 atm. Between each mixing step, the walls of the mixing container were scraped to ensure complete mixing, and the containers were stored in the oven to maintain a low viscosity. Prior to the addition of curing agent, the oven was held at 100°C with mixing occurring once $T_{resin} > 80°C$ and the material could readily flow. After the addition of the curing agent, the mixing temperature was lowered to 70°C to reduce the risk of crosslinking.

To observe thermal flow properties for both extrusion and cure, a rheological temperature sweep was conducted on 6040 ink following the same parameters as with the neat resin blends described above. Further testing was conducted at 50, 70, 90, and 110°C. To determine the pot life, 24-hour isothermal tests were conducted using oscillation rheometry with a frequency of 1 Hz

and a constant stress of 20 Pa on 25 mm flat platens at each temperature. Crosslink initiation was defined as the inflection point where the viscosity began increasing, and the pot life was determined by the plateau [95, 221].

Once formulated, the ink was manually loaded into 30 cc syringe barrels (Nordson EFD, Westlake, OH) using a spatula. Filled syringe barrels were placed in a 70°C oven for 20 minutes prior to being centrifuged at 3000 rpm for 10 minutes using a Sorvall ST-8 Centrifuge (ThermoFisher Scientific, Waltham, MA). Heated syringe barrels were insulated with zetex fabric (ID 5619T57, McMaster-Carr, Elmhurst, IL) during this degassing step. The heating and centrifuging process was repeated 3 times to remove all air bubbles trapped in the resin, as these can cause defects while printing.

During printing, the syringe barrel was maintained at 55°C using a heated syringe wrap (New Era Pump Systems, Farmingdale, NY), and the nozzle was held at 70°C via Repetier software (Repetier, Germany). The 515-µm-diameter brass nozzle and barrel heater assembly were taken from an FFF printer and mated to the syringe barrel using a stainless steel luer-to-thread adaptor (SKU 6264IND, Cadence Science).

G-code prints paths were generated using Scilab software (Scilab Enterprises, France) and executed on a custom direct ink writing platform comprising a 3-axis positioning stage (Shopbot Tools Inc., Durham, NC), solenoid valves, and an air pressure regulator (Fisnar JB1113N, Germantown, WI). To enable removal of the printed, cured components from the build plate, the aluminum build plate was covered with a PTFE-coated aluminum foil (Bytac, Saint-Gobain Performance Plastics, Worcester, MA). Printed objects were pre-cured at 70°C for 24 hours before being transferred to an uncoated aluminum sheet for the final step cure at 160°C for 12 hours followed by 6 hours at 200°C.

Five separate identical printed honeycombs (40 x 15 x 30 mm, t_{wall} = 0.515 mm) were used to evaluate the cure behavior at the same four temperatures (50, 70, 90, 110°C) along with a 10°C/minute ramp. At each isothermal cure, the honeycomb was placed in a heated oven for 24 hours. Because no cure was detected (no color change and resin remained pliable at RT) at 50°C, an additional 24-hours was provided. At 110°C, charring was detected (smell) and the sample was removed from the oven after 20 minutes with a measured surface temperature over 300°C. The ramp cure heated from 25°C to 175°C in 15 minutes. However, the heat produced by the reaction caused the cycle to be ended at 160°C when noticeable charring (smell and smoke

escaping the oven) were detected and the sample was allowed to fully cool in the oven before removal.

Thermal expansion and heat deflection temperature (HDT) were measured using a TA Instruments Q400 series thermomechanical analyzer (TMA, TA Instruments, New Castle, DE) with a heating rate of 10°C/min in air. Expansion utilized the expansion probe on a 2.4 mm cube. The coefficient of thermal expansion (CTE) was the slope of the linear regions below and above T_g which was determined by the inflection point.

HDT tests followed ASTM Standard 2092 [134] in the 3-point bend configuration on a single printed filament (4.98 x 1.30 x 0.325 mm). Based on the cross-section of the printed filament and a constant stress of 0.455 MPa, the applied load was calculated following eq. 5 with the HDT value recorded at the deflection corresponding to 0.2% strain following eq. 6. A heating rate of 10°C/min from ambient to 300°C was followed. The HDT gives a mechanical guideline for maximum working temperatures.

Both dynamic mechanical analysis (DMA) and flexure tests were conducted on 35 x 6.5 x 1.7 mm bars printed in both the longitudinal and transverse directions with a span length of 25 mm tested in a 3-point bend configuration. DMA was conducted on the Discovery HR-2 hybrid rheometer with the 3-point bend configuration and the same thermal profile as with TMA and DSC. Flexure measurements utilized a MTS machine (MTS, Eden Prairie, MN) with a 1 kN load cell and a crosshead speed of 0.4 mm/min following ASTM D790 [222]. The top and bottom surfaces of printed samples were ground flat. Density measurements was taken using Archimedes principle.

4.3. Results

4.3.1. Resin Blends

DSC thermograms of the resin blends are shown in figure 13.a. The crosslinking reaction creates two exothermic peaks at approximately 135 and 160°C before returning to the baseline at 250°C. Crosslinking does not begin until above 110°C, regardless of the composition of the blend. The HP-7250 displays the lowest heat of cure at 425 J/g, while the HP-4032SS displays the highest heat or cure of 580 J/g (nearly 35% higher than the HP-7250). Blends follow a linear rule of mixtures between these two values (figure 13.b). From this information we tentatively identify 55°C (one half of the cure onset temperature) as the target working temperature for

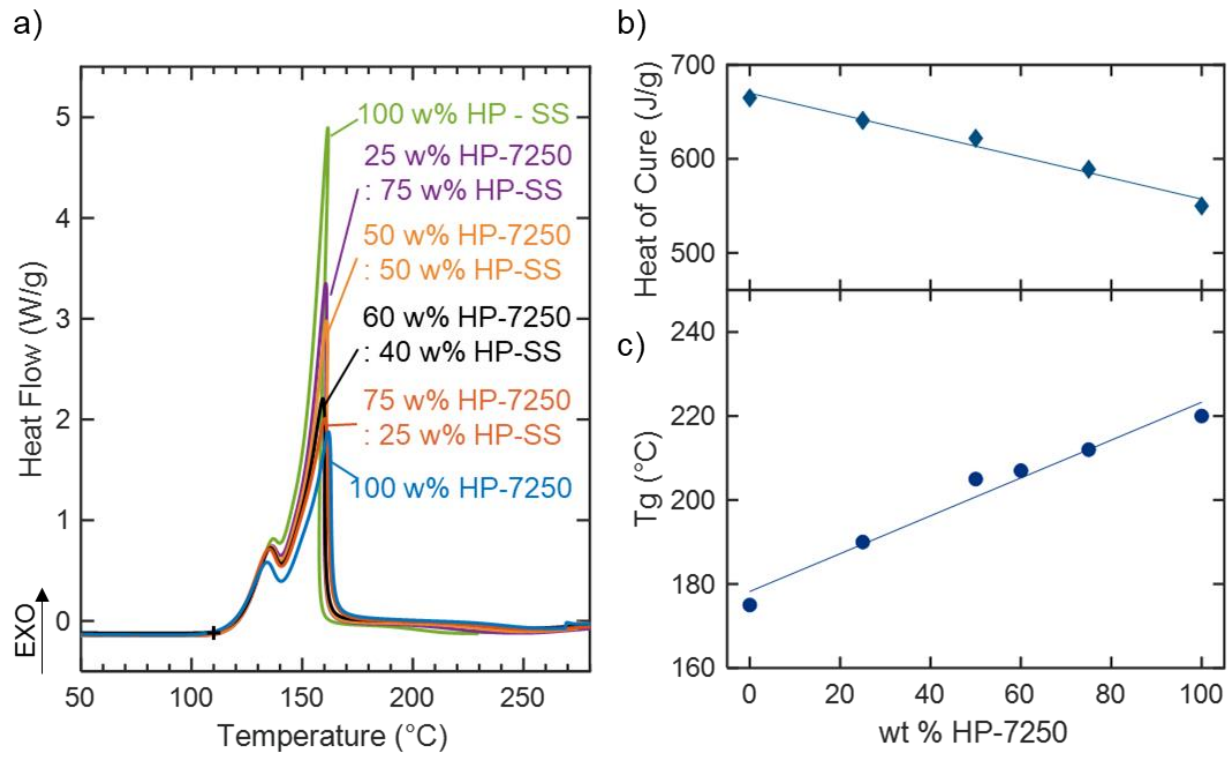

Figure 13. *DSC of blends of HP-SS and HP-7250. a) exothermic plot of resins during cure, b) produced heat during cure, c) the glass transition temperature. Resins are tested prior to the addition of clay at a heating rate of 10°C/min.*

formulation and printing, as this temperature is anticipated to provide reduced viscosity needed for mixing (confirmed below) and long pot-life needed for printing (confirmed in section 3.2).

Glass transition temperatures for the blends follow a linear trend, with T_g increasing from 175°C to a maximum of 225°C when going from 100% HP-4032SS to 100% HP-7250 (figure 13.c). All blends containing 50% or greater HP-7250 by weight yield T_g values above 200°C with a 1:1 blend resulting in a T_g of 205°C.

Viscosity measurements of the neat resin blends are depicted in figure 14.a. For comparison, data for Epon 826 epoxy resin is included as well, as this resin forms the basis for many printable epoxy formulations reported in the literature [35, 37], and is easily formulated into a successful ink at room temperature. From pure HP-4032SS to HP-7250 there is an increase by over three orders of magnitude in viscosity at room temperature, from 12 Pa-s to 60,000 Pa-s. Epon 826 has a RT viscosity of 4.4 Pa-s. For the purposes of formulation of a printable ink, this viscosity value (η^*) will be considered the target upper limit for a candidate blend. The temperature at which each blend exhibits this viscosity value is plotted in figure 14.b. Although the least viscous, HP-4032SS still requires an elevated temperature of 53°C to exhibit similar viscosity. The blends follow a linear increase to 70°C for HP-7250. Based on these viscosity data, the target of T_g > 200°C, and the target of 55°C working temperature, a blend of 60% HP-7250 and 40% HP-4032SS by weight – hereafter referred 6040 – is selected as the optimal blend to formulate a printable high temperature epoxy composite ink. Relevant properties of this blend are summarized in table 6.

4.3.2. Gel Time and Curing Process

Figure 15 depicts the storage modulus, loss modulus, and complex viscosity for the 6040 ink (comprising the 6040 resin blend with 14 pph by weight nanoclay and 5 pph curing agent) during a 10°C/min temperature ramp. As compared to the unfilled 6040 resin blend, the addition of nanoclay and VS03 increases the room temperature viscosity by 3.5×10^4 Pa.s to 4.0×10^4 Pa.s. The moduli and viscosity decrease rapidly during the early stages of the temperature ramp. The storage modulus and complex viscosity reach a minimum at 90°C, decreasing by approximately an order of magnitude from their room temperature values. Above 90°C, the storage modulus and complex viscosity begin to rise rapidly up to 160°C where the slope becomes infinite, indicating that gelation has occurred. The loss modulus reaches a minimum value at 110°C and

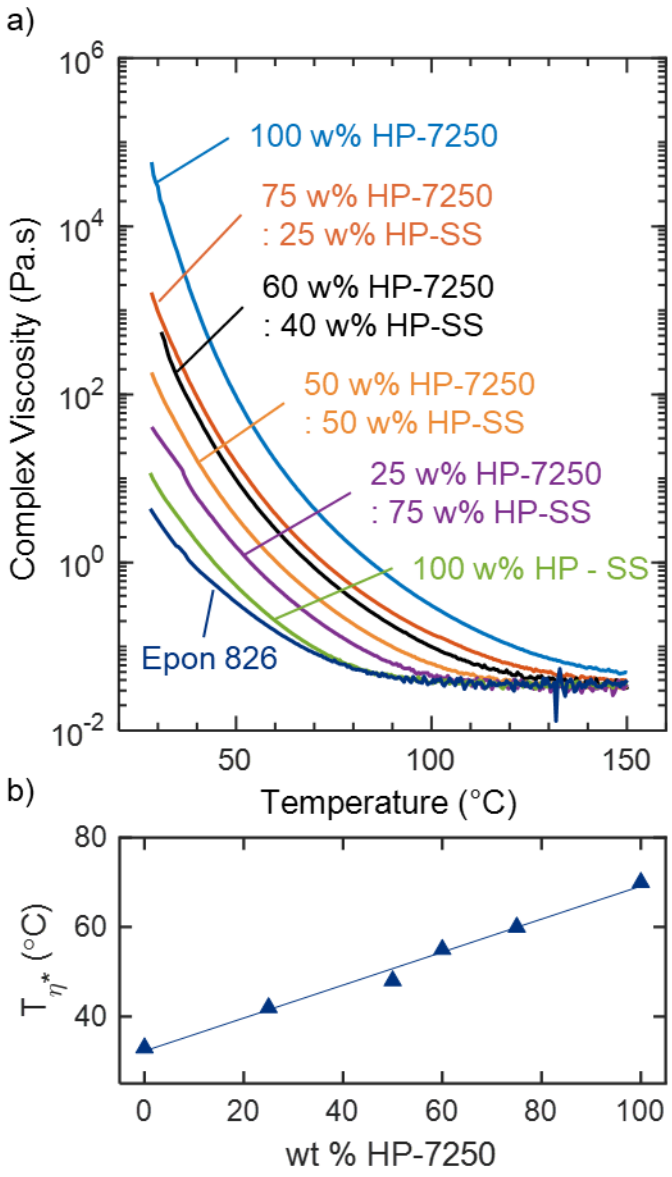

Figure 14. *Rheology of unfilled resin blends. A) viscosity of the resins as a function of temperature and B) temperature at the target viscosity (4.2 Pa.s) as determined by the RT viscosity of Epon 826. Resins are tested prior to the addition of clay and curing agent.*

Table 6. *Measured properties of the resin blends.*

Sample	Rheology		DSC				
(HP-7250 : HP-SS)	η_{RT} (Pa.s)	T_{η^*} (°C)	T_{onset} (°C)	$T_{p,1}$ (°C)	$T_{p,2}$ (°C)	ΔH (J/g)	T_g (°C)
100 : 0	60,000	70	109	134	162	550	220
75 : 25	1,600	60	110	136	161	590	215
60 : 40	600	55	110	135	160	605	207
50 : 50	180	48	110	135	161	622	205
25 : 75	70	42	111	136	160	640	190
0 : 100	13	33	111	136	161	665	175

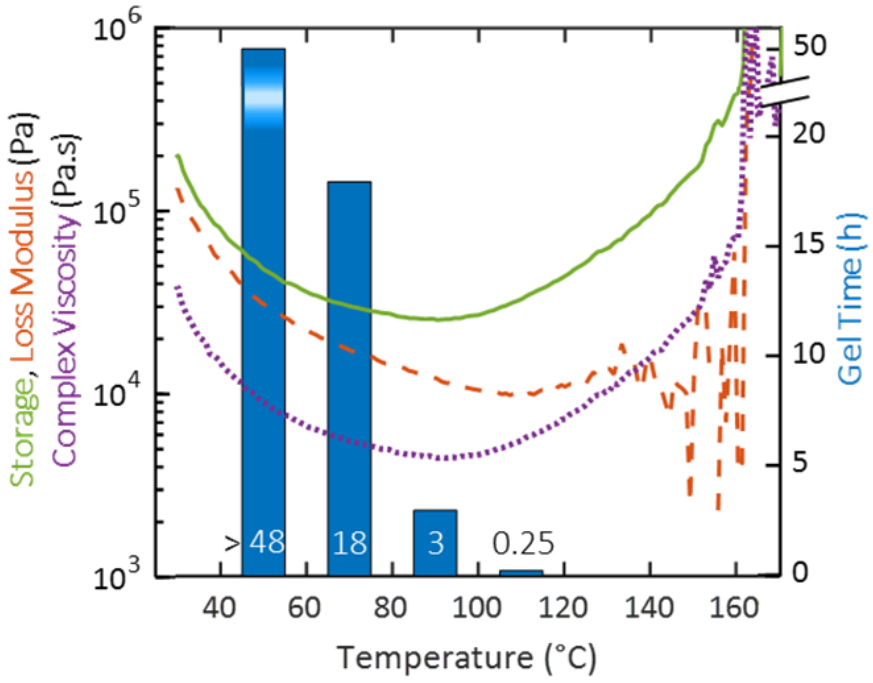

Figure 15. *Viscosity, storage, and loss modulus as a function of temperature as the resin crosslinks. These are overlaid with the gel times at 50, 70, 90, and 110°C measured by isothermal rheometry. All curves correspond to the left axis while the bar marks follow the right.*

increases more slowly with increasing temperature to 130°C above which the measurement contains significant noise.

Overlaid on this plot is the gel time measured via isothermal oscillatory rheometry at four different temperatures. Temperatures of 50°C, 70°C, 90°C, and 110°C are selected to encompass the working temperature, the temperature at minimum viscosity and a temperature above the minimum viscosity where the gel time is expected to be low. From gel time measurements at 50°C, there is minimal increase in the isothermal viscosity over a 48-hour period, indicating a pot life longer than 2 days at this temperature. At 70°C, the curve follows the traditional S-shaped curve [156, 165, 221] for epoxy cure. An initial flat region occurs before crosslinking begins with an increase in viscosity following the cure progressing. Gelation occurs once the viscosity curve plateaus. Here, crosslinking begins at 9 hours with gelation after 18 hours at 70°C. Both 90 and 110°C show immediate crosslinking once the temperature is reached and gel after 3 hours and 15 minutes respectively. From these results and various printing tests, a temperature of 55°C and 70°C were selected for the syringe barrel and nozzle, respectively, to be used during printing of demonstration pieces and test articles described next.

Four tall, thin-walled honeycomb structures were printed and subjected to the same isothermal heat treatment used for the gel time experiments, and a fifth identical honeycomb was printed and subjected to a 10°C/min temperature ramp. Each honeycomb was 30 mm tall with an average wall thickness of 0.82 mm. Heat treatment at 50°C resulted in no change in color, no noticeable loss of shape (figure 16.a), and the material remained soft and pliable after 2 days at temperature. After heat treatment at 70°C, the printed structure changed color from the light yellow of the as-printed ink to a dark brown (figure 16.b). This color change is characteristic of homopolymerization from the use of imidazoles as curing agents in epoxy resin [37], and indicates some level of crosslinking has occurred. After heat treatment at 90°C the printed structure attained the same color as that treated at 70°C, but honeycomb completely collapsed to 11 mm (figure 16.c). Both the treatment at 110°C and the temperature ramp resulted in collapsed structures, with some evidence of charring (a rough, black surface and noticeable odor) (figure 16.d,e). During the isothermal treatment at 110°C, this charring was observed after only 20 minutes in the oven, at which point the surface measured 300°C. The structure that was subjected to the temperature ramp reached 160°C in 14 minutes when it began to release smoke from the oven. The oven was immediately shut off and the structure was allowed to cool in the oven. After cooling, the structure was inspected and found to possess both smooth edges and a rough, charred base.

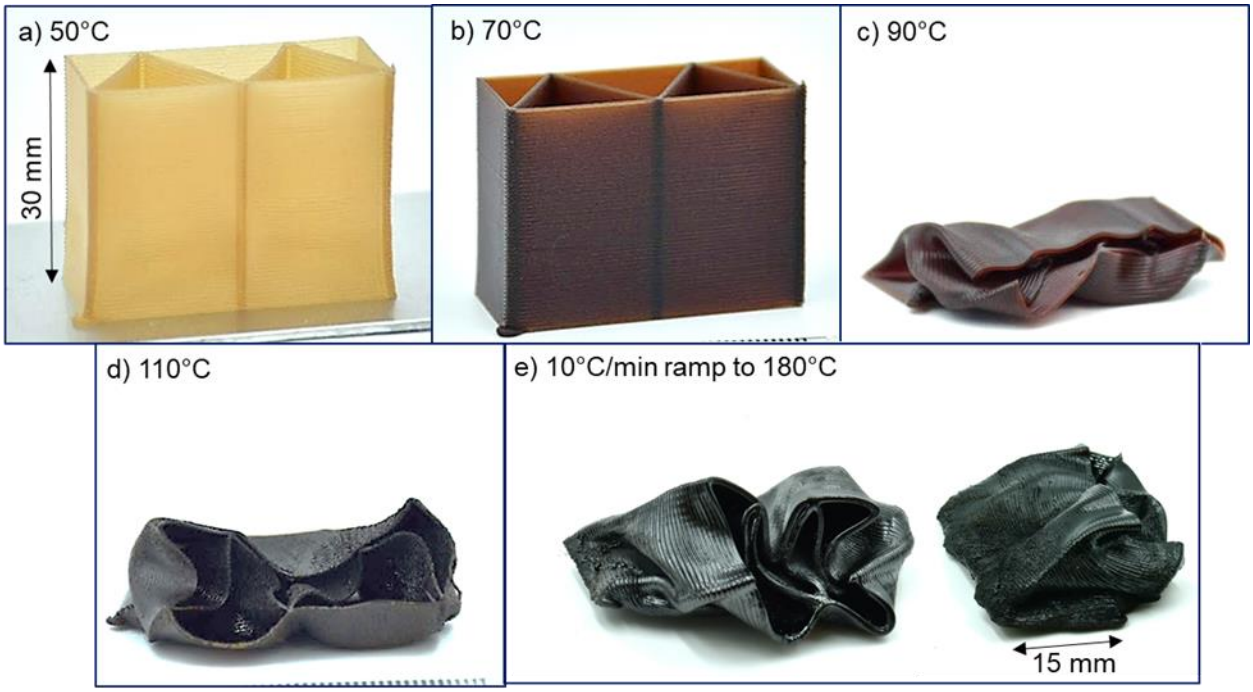

Figure 16. *Single wall honeycombs printed and cured at a) 50°C, b)70°C, c) 90°C, and d) 100°C. To directly compare to the rheological temperature sweep in fig. 15, e) is cured at the same ramp rate of 10°C/min to 180°C. Prints have an average wall thickness of 0.7 mm, a height of 30 mm, and length and width of 40 and 15 mm respectively.*

From these results a 24-hour pre-cure at 70°C was selected. Subsequent post-curing experiments at 160°C and 220°C demonstrated successful curing without charring or slumping.

4.3.3. Printed Structures

Selected printed objects are shown in figure 17. The cone is 100 mm tall with an average wall thickness of 1.2 mm (figure 17.a). Next to the cone is a 15-mm-tall dome with an outer radius of 20 mm (figure 17.b). An infill with a radius of 12 mm allowed for a 35° overhang to both print and cure. Next, a 30 mm wire clip and impeller geometry are shown (figure 17.c, d). As opposed to the other prints which were designed using SciLab programming software, the clip demonstrates an object printed from an .stl file generated from a solid CAD model making this process more adaptable than previously achieved. The wire clip also demonstrates the ability of the ink to span a free gap to create a mounting hole with a 15° overhang. The impeller has 13 mm long blades, also printed at a 15° angle. While the outer and inner cylinders are comprised of multiple printed beads, with a wall thickness of 0.9 mm, the blades are comprised of only a single print path (0.515 mm thick) and are able to maintain integrity throughout the printing and curing process. The printed bars shown figure 17.e, f are used for DMA and flexure testing. These highlight the clean, sharp surface finish that results from heated DIW printing process. Printed objects reach 1.33 g/cc as the cured density.

4.3.4. Thermal and Mechanical Properties

Figure 18.a shows the results of 3-point flexure DMA measured both along the print direction (axial) and transverse to it (transverse). T_g measured using the peak of the tan(δ) curve yields T_g = 218°C which decreased to 202°C when measured by the tangent intercept of the storage modulus. There is minimal difference between the two print directions. At room temperature, the storage modulus is 3.2 GPa. This value decreases to 2.5 GPa at 150°C and 1.8 GPa at 200°C.

Results from the thermal expansion and HDT measurements are shown in figure 18.b. Using the expansion probe, T_g via TMA is 205°C as indicated by a change in slope. Below this temperature, the coefficient of thermal expansion (CTE) is 0.1843 um/°C, and above this temperature the CTE is 0.4593 µm/°C.

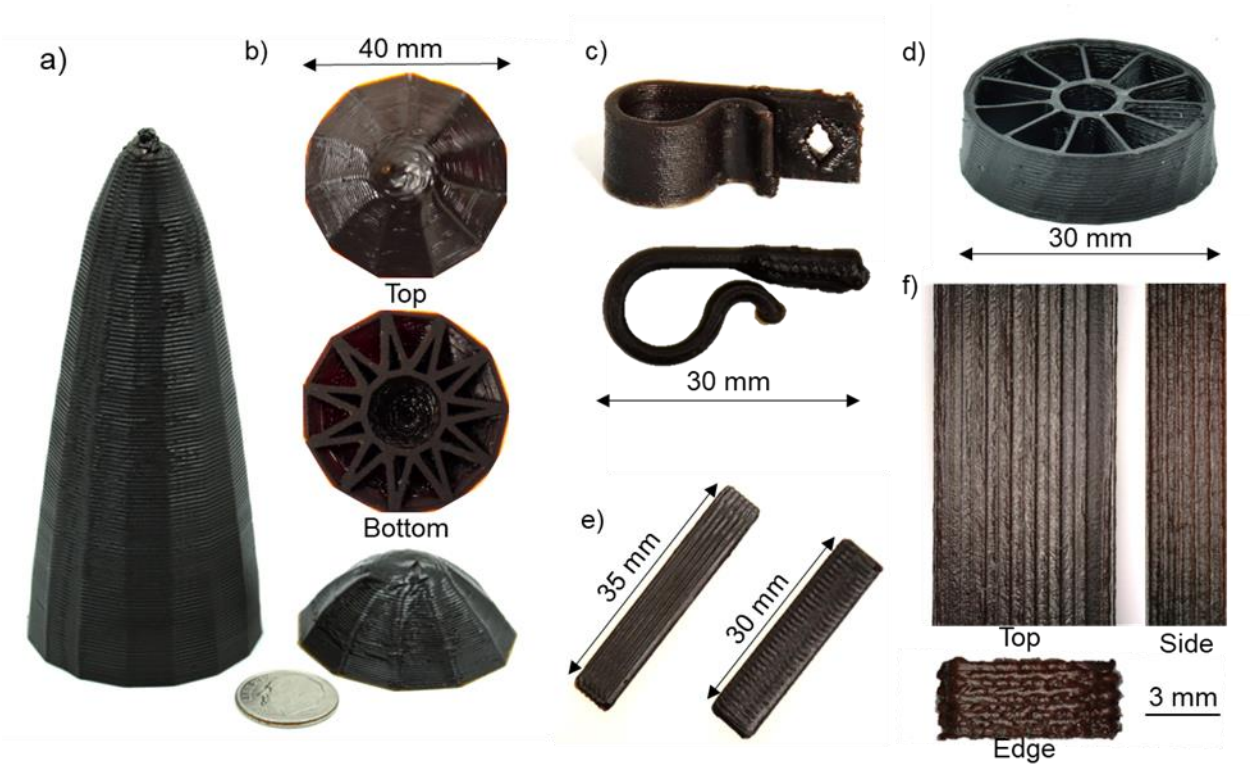

Figure 17. *Selected prints. a) 100 mm wall cone with a base radius of 20 mm and wall thickness of 1.2 mm. b) top, bottom, and side view of a 15 mm dome with an outer radius of 20 mm and inner radius of 8 mm with a star infill connecting the two. C) wire clip as could be used in application with a wall thickness of 0.9 mm and a screw hole with a 15° overhang. D) impeller with a 30, also printed with a 15° overhang on each 12 mm long blade. Bend bars printed both along and against the testing direction are show in (e) with surfaces enlarged in (f) to show detail.*

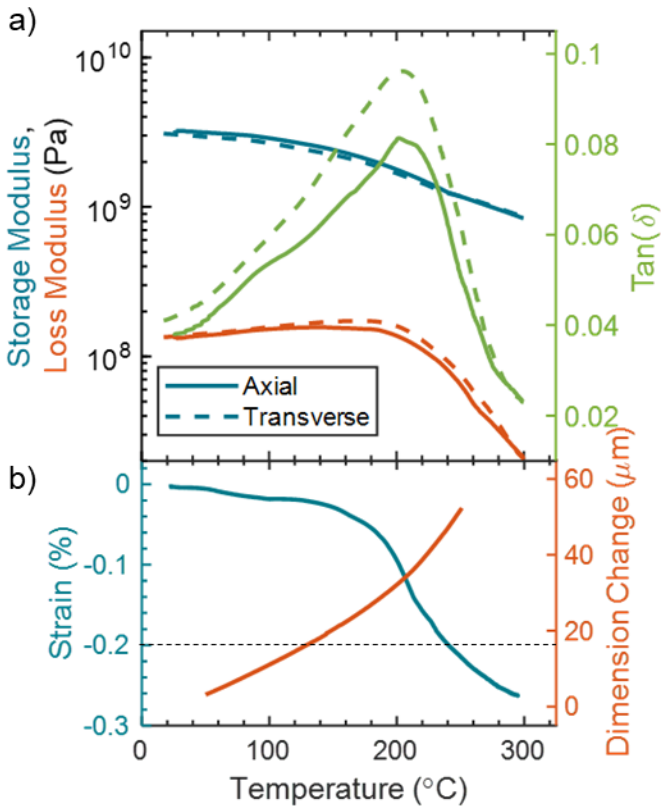

Figure 18. *Printed thermal properties: a) storage and loss moduli and tan(δ) from 3-point oscillatory DMA and b) gives the deflection temperature and thermal expansion from TMA.*

From 3pt-flexure geometry of a single row extruded filament, the HDT is measured as the temperature at which the maximum flexural strain reaches 0.2% during a temperature ramp at a constant applied stress of 0.455 MPa. Minimal deformation occurs up to ~150°C, after which the deformation rate increases and reaches a maximum at ~200°C. Deformation continues above this temperature until 0.2% strain is attained at 240°C.

Room temperature 3pt-flexure tests are shown in figure 19. The flexural modulus along the print direction is 4.26 ± 0.25 GPa and 4.01 ± 0.25 GPa transverse to the print direction. The flexural strength is 130 ± 20 MPa along the print direction and 82 ± 15 MPa transverse to the print direction. The strain-to-failure is 2.2% along the print direction and 3.5% transverse to it.

4.4. Discussion

4.4.1. Selection of Blend

A delicate balance must be met for these inks to be printable via DIW: a resin must be able to flow and hold shape. While elevated extrusion temperatures will allow for the resin to flow, HP-7250 has an initial RT viscosity of 60,000 Pa.s and is unable to incorporate nanoclay, failing the second criteria. By using a resin blend will reduce viscosity such that nanoclay can be incorporated, the additional requirement of miscibility must be considered. For the present blends, miscibility is confirmed by the presence of a single T_g in DSC as well as the linear relationship in the heat of cure [13-15].

Epon 826 has been shown to successfully print with the addition of nanoclay [7, 16]. Unlike the high temperature resins, Epon 826 incorporates nanoclay well at ambient temperatures. As such, the room temperature viscosity will be used as a reference for the high temperature system. Comparable flow behavior of the blend at an elevated “working” temperature should give the desired mixing properties.

Although higher temperatures do decrease the viscosity, they also increase the likelihood of crosslinking which is irreversible and catastrophic during formulating or printing. To prevent this, the working temperature will be set at 55°C which is ½ the onset temperature as measured by DSC. Although cure does occur below the onset temperature measured by DSC, it occurs at a lower rate. Further work with the cure time shows that the pot life at 50°C is greater than 2 days.

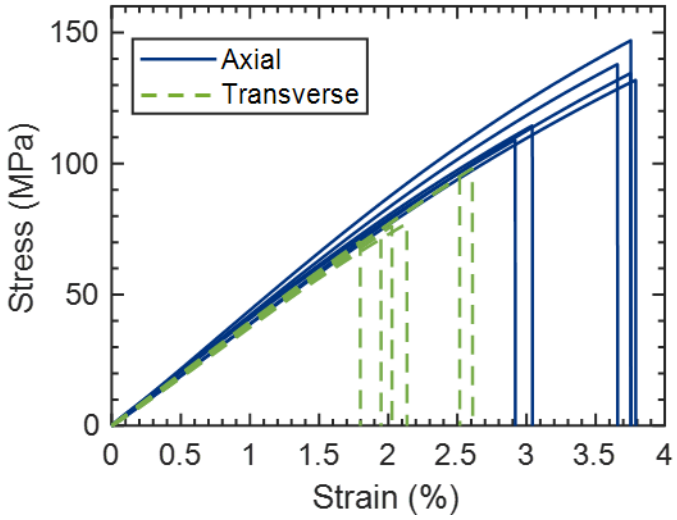

Figure 19. *Room-temperature mechanical tests conducted in 3-point bend geometry of bars tested both axially and transverse to the print direction.*

The viscosities of the 50:50 and 75:25 blends of HP-7250 : HP-4032SS straddle the target temperature of 55°C. As both of these blends fall above the minimum glass transition temperature (200°C) at 205 and 215°C respectively, the printability takes precedence. Following the linear viscosity-temperature trend observed in figure 14.b, at 55°C, a 60:40 blend is selected with the highest likelihood of printability. While a higher content of HP-7250 is likely to yield a higher usable temperature, higher extrusion and mixing temperatures would be required, increasing the likelihood of premature cure.

4.4.2. Temperature Profiles for Processing and Cure

Controlling the inverse relationship between temperature (and crosslinking) and viscosity is paramount. During formulating and printing, enough heat must be added so that the ink can readily flow, but not cure. Conversely, during the heated cure, the resin must be stiff enough to hold shape and not flow while still form crosslinking bonds.

During mixing, lower viscosities allow for faster and smoother blending with less energy required. However, once the curing agent has been added, the elevated temperatures associated with these viscosities can induce curing. As such, prior to the addition of curing agent, the resin can be mixed at 100°C which correlates to the resin viscosity below 4,800 Pa.s. However, once the curing agent has been added, the resin begins to crosslink in under an hour at this temperature. By lowering the mixing temperature to 70°C, the working time increases to 18 hours while still allowing for sufficient flow to homogenize.

While mixing occurs in approximately 20 minutes, printing takes longer. From the initial temperature estimation (50°C), there is at least a 48-hour pot life and the viscosity has dropped by a full order of magnitude. While this is effective for the bulk material in the syringe, the resin remains too viscous to extrude through at 515 µm nozzle. The nozzle temperature is increase to 70°C with an additional 40% reduction in viscosity. With a 9-hour window before crosslinking begins and an additional 9-hours before cure, this provides a long working time without premature cure during set up or breaks in extrusion. Increasing the nozzle temperature provides negligible increase in flow properties with a higher likelihood of detrimental early crosslinking.

When considering cure, the viscosity is at the minimum during the initial heating before crosslinking begins. As such, although both 70 and 110°C present the same viscosity, at 110°C, the uncured resin passed through the minimum viscosity at 90°C and the printed honeycomb

collapsed in on itself. Although both the 90 and 110°C prints crumpled, the higher temperature lead to a faster cure with a taller failed print.

Both the 10°C/min ramp and 110°C isotherm cured in under 15 minutes and the reaction autoaccelerated, which highlights the safety requirement of understanding the pre-cure. Despite being held at a constant temperature with relatively thin walls of 0.82 mm, the 110°C honeycomb reached temperatures above 275°C after 15 minutes. Although closest to the manufacture recommendation of an hour cure at 160°C, the ramp, which reached a maximum oven temperature of 170°C in 14 minutes, produced a significant amount of heat. While the surface temperature was unable to be measured, the upper edges of the print became smooth with minimal evidence of the print path although clear edges are still present. Although the base was unable to release the produced heat and experienced significant charring, the upper edges melted and solidified simultaneously.

At 90°C, the wall thickness becomes increasingly important. With thin walls, the prints fail due to viscosity as shown in figure 16.d. However, with thicker walls, the print is able to stand. Increasing the wall thickness to that which would be required for scaling up, the ink does char. Although a pre-cure at 90°C could reduce the total energy required during cure, the uncertainty and variation of print stability and the possibility of a runaway reaction increase the complexity and over-complicate the cure.

Practically, a 24-hour 70°C isotherm is selected for the pre-cure. Although rheometry indicates a gel time of 18-hours, work by Patel et al. suggests that a longer pre-cure improves the fully cured properties [17]. Although additional reactions become diffusion-dependent and require more time to occur, the epoxy has reached a critical gel point where the matrix is homogeneous and weaker regions with a lower crosslinking density do not exist. The improved moduli and lifespan offset the higher energy costs.

4.4.3. Printed Properties

From room (21°C) to cure (70°C) temperature, unfilled 6040, figure 14.a, decreases in viscosity by 500 Pa-s as compared to 4.4 Pa-s from Epon 826. As such, more nanoclay is required for the printable formulation to maintain structure during cure than had been previously optimized [6]. Therefore, the room temperature mechanical properties are predictably lower than other systems. However, the elevated temperature properties outperform other printable epoxies. With a T_g > 200°C measured by four different methods, the resin is reliable under varying high

temperature applications. For a more practical evaluation of structural performance, the deflection temperature has an increased value of 240°C which allows for a working temperature above 200°C. At temperature (200°C), the flexure modulus is 2.1 GPa as compared to 0.1 – 0.4 GPa for other resins as seen by DMA [6]. Further, both deflection temperature and mechanical strength will increase with the addition of fibers.

Further, by using a headed extrusion system, many of the beneficial properties achieved in fused filament fabrication (FFF) of thermoplastics are able to be achieved. Unlike many thermosets, the resin cools and becomes rigid during printing and larger print overhangs are able to be produced. The rigid previous layers allow for a smooth surface finish. However, unlike thermoplastics, epoxy undergoes a cure before the final part is produced. As such, the poor interlayer adhesion and residual stresses created by laying hot material onto cool material is reduced. When comparing to commercial high-temperature printable thermoplastics, 6040 has higher strength and modulus. Unlike thermoplastic fracture surfaces, there is minimal evidence of individual layers and tears propagating along the print path.

4.5. Conclusion

A printable, high-temperature thermoset epoxy blend, 6040, was developed with a T_g of 210°C. While higher HP-7250 content could further improve the thermal properties, the higher viscosity would increase the required extrusion temperature which could lead to premature cure in the nozzle using the current printing methodology. However, by engaging a warmed extrusion process, many of the beneficial properties of thermoplastic printing, such as clean print rows, long pot life, and improved stability from printing on rigid layers, are achieved although issues, such as poor interlayer strength, are minimized from the heated post-cure.

The formulation work is included in its entirely to show the relationship between the temperature and viscosity. From thermal work, it was found that a longer, lower temperature cure provided the best cure stability and final properties. The same temperature that the epoxy was cured at also provided the best flow behavior during extrusion. Although brittle, 6040 presented high strength and moduli values that can be further improved with the addition of fibers or other reinforcing agents.

CHAPTER 5
GLASS FIBER COMPOSITES

Disclosure: This work will be published with a submission target of Fall 2020. This work was completed and written alone with feedback from the projects PI, Brett Compton.

5.1. Abstract

Fiber composites are critical for high temperature structural components where specific strength and stiffness are required. Although additive manufacturing boasts superior design freedom with reduced geometric manufacturing constraints, most usable materials present insufficient mechanical properties for many applications. This incorporates milled glass fibers into the high temperature 6040 epoxy blend developed in chapter 4 to improve the heat deflection temperature by 60% and the modulus by 54%. Glass fibers are selected for their low cost, durability in off-axis orientations, and IR transparency for radome applications. The processing mechanisms are examined showing that mixing does not have a significant impact on the final fiber length.

5.2. Materials / methods

5.2.1. Materials

The same 6040 resin blend of Epiclon HP-7250 and HP-4032SS (DIC, Japan) with 14 pph Garamite 7035 nanoclay (BYK-Chemie GmbH, Wesel, Germany) were used in this study (see chapter 4.2.2 for the epoxy and clay mixing protocol). Rather than continuing with VS03 as the curing agent, a dicyandiamide with 3% of an inert flow control additive was used instead (Dicyanex 1400B, DICY, Evonik Corp., Allentown, PA). DICY is a fine powder that disperses readily under mixing, has a shelf stability of up to 6 months, and produces higher glass transition temperatures than the previously used EMIM Dicyanimide, VS03 [154].

Milled E-glass fibers with a 16 μm diameter and average length of 200 μm were added for strength and stiffness (1/16” GF 329, Fibre Glast Developments Corp., Brookville, OH). The fibers have a density of 2.6 g/cc and are incorporated in the as-received form. Sizing was accomplished by reaching an average bulk density of 0.53 g/cc via milling.

5.2.2. Formulation

The 6040 resin and 14 pph nanoclay were mixed following the same schedule outlined in chapter 4.2.2 at 80°C. Fibers were added in increments of 10 vol% to create 0, 10, 20, and 30 vol% inks. After each addition of fibers, the ink was mixed at 1600 rpm for 4 minutes at 0.4 atm. Intermediate heating was not required as friction from the fibers created heat reaching temperatures of 95°C. Walls were scraped after each mix. The resin was allowed to cool to 60°C before adding 5 pph of DICY which was mixed at 2350 rpm for 2 minutes at 0.1 atm. The ink was then remixed following the same protocol and loaded into a 30 cc syringe barrel (Fisnar, Germantown, WI) using a Speeddisk loading system (FlackTek Ink, Landrum, SC) while still warm.

Ink was extruded using the same custom DIW platform described in chapter 4.2.2. For all ink formulations, the bulk material was held at 55°C with a head rate of 20 mm/s and a 732 um nozzle diameter. The nozzle temperature ranged between 70 and 85°C with the pressure between 40 and 85 psi as described in table 7. Prints followed at 20 h pre-cure at 85°C followed by 18 h at 180°C and 6 h at 200°C.

5.2.3. Characterization

Fiber Length

Prior to the addition of curing agent, ~1 g of each ink was removed, placed on a glass slide, and dissolved in acetone to leave the fibers behind. Images were taken using a VHX-5000 digital microscope (Keyence Corporation of America, Itasca, IL.). Approximately 1,500 fibers per set were measured by hand using ImageJ software (ImageJ, NIH, Bethesda, MD.) [223].

Rheology

Rheological measurements of the ink were taken using a Discovery HR-2 Rheometer (TA Instruments, New Castle, DE) with the 25-mm parallel plate geometry. Tests were conducted at a frequency of 1 Hz with a 1.0 mm gap. Oscillatory stress sweeps were performed in stress-control mode from 5 – 10,000 Pa at 70°C which is the base extrusion temperature from the unfilled

Table 7. *Extrusion parameters of the fiber-filled inks.*

Fiber content	Extrusion Pressure	Temperature		Nozzle Diameter	Head Translation Speed	Δz
		Nozzle	Barrel			
(vol %)	(psi)	(°C)	(°C)	(μm)	(mm/s)	(μm)
0	40	70	55	713	20	392
10	50	70	55	713	20	392
20	60	75	55	713	20	392
30	85	85	55	713	20	392

ink. Temperature sweeps were conducted at 5°C/min to 95°C maintaining 20 Pa as the constant stress.

DMA / Flexure

Both DMA and flexure testing were conducted on printed 8 x 2.5 x 35 mm bars along both the longitudinal (axial, 0°) and transverse (90°) directions in 3-point loading with a 25 mm span length. DMA was conducted from RT to 325°C at a heating rate of 5°C/min with an oscillation frequency of 1 Hz on a Discovery HR-2 Rheometer (TA Instruments, New Castle, DE).

Flexure testing was conducted on an electromechanical load frame (MTS, Eden Prairie, MN) with a 1 kN load cell and a crosshead speed of 0.4 mm/min following ASTM D790 [222]. The top and bottom surfaces of printed samples were ground flat using a M-Prep 5 polishing wheel (Allied High Tech Products, Inc., Compton, CA).

Deflection

Heat deflection temperatures were conducted following the same parameters as above (chapter 2.2.2 and 4.2.2) on single road printed filaments. While dimensions changed and the force was recalculated for each, the beads had an average width of 1.25 mm and thickness of 0.5 mm leading to a 20.4 ± 9.4 mN force for the 4.98 mm gap length. For each set, 5+ samples were tested.

Microscopy

Scanning electron microscopy (SEM) were collected using a Phenom Pro X scanning electron microscope with a 10 kV image (Phenom-World BV, Netherlands). SEM samples were gold-coated using a SPI-Module Sputter Coater (EDEN Instruments, France) for 10 seconds to provide a conductive surface on the epoxy and fibers. Optical microscopy was also obtained using a VHX-5000 digital microscope (Keyence Corporation of America, Itasca, IL.).

5.3. Results

5.3.1. Fiber Length and Ink Rheology

Figure 20 depicts the cumulative distribution function and probability distribution function for fiber length measurements of the 3 blends as compared to the as-received fibers. Neither content nor mixing time was observed to have a significant impact on fiber length. The volume-

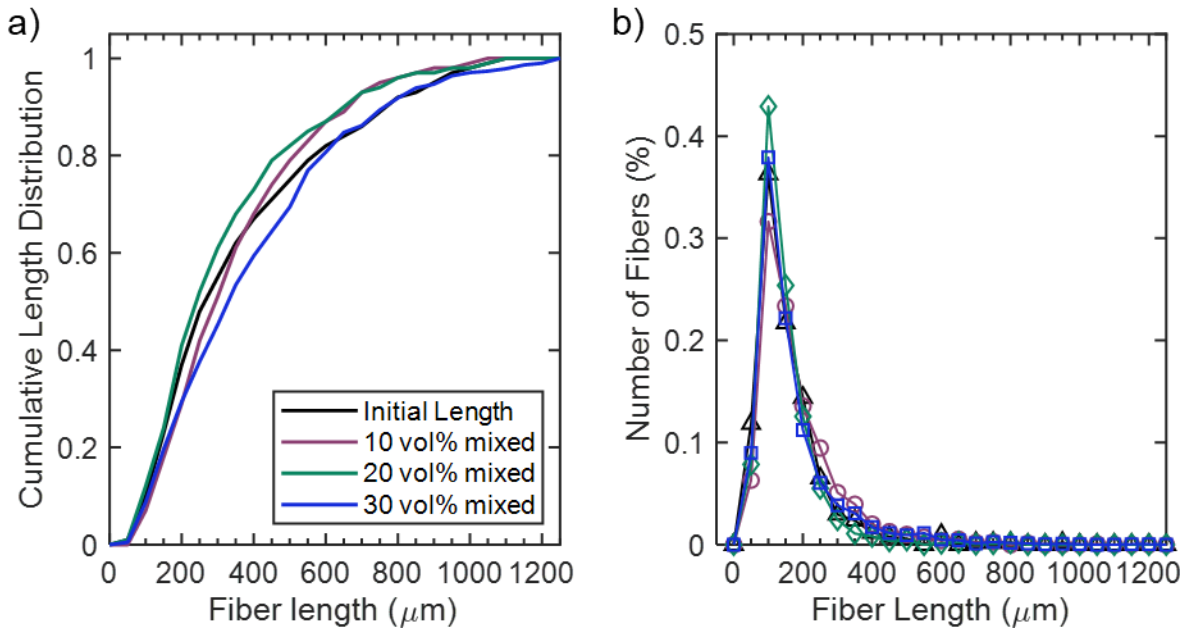

Figure 20. *Fiber length of GF after fully mixing in inks. A) give the probability of fibers shorter than some length while b) shows the probability of a fiber at a given length.*

weighted average fiber length for the as-received fibers was measured as 235 μm. To incorporate 10 vol% GF, the ink is mixed for 8 minutes and has an average length of 260 μm; 20 and 30 vol% fiber loadings are mixed for 12 and 16 minutes to produce 200 and 266 μm long fibers respectively. With a critical length of 120 μm, by volume, 15% of fibers are shorter this. While the as-received fibers are shorter than 10 and 20 vol% processed lengths, this is minimal can be accounted for by fibers settling where they have been taken from different sections of the container as well as insufficient measurements taken.

Figure 21 shows the viscosities of the four inks as a function of temperature. At 21°C, there is a 300% increase in viscosity from the unfilled to 30 vol% GF ink (figure 21.a). The curves follow similar decreasing slopes to 95°C where they begin to level. Practically, the inks are extruded with nozzle temperatures between 70 and 85°C. Figure 21.b shows the viscosity of the ink blends bracketing this range. While the unfilled and 10 vol% GF inks have similar flow behavior, the viscosity doubles for the 20 vol% ink followed by an additional 130% increase to the 30 vol% GF formulation. For comparison, at 85°C, the 30 vol% formulation has the same viscosity (19 Pa.s) of the unfilled ink at 35°C.

A rheological stress sweep at 70°C, depicted in figure 22, completes the flow property work. The full curves are shown in figure 22.a while 22.b plots the storage plateau modulus and shear yield stress with increasing fiber content. Here, the left axis shows the plateau storage modulus. Because the storage modulus is higher than the loss modulus for all, this indicates solid-like behavior at low stresses [37]. Above a threshold defined by the shear yield stress (right axis), the storage and loss modulus cross and the ink displays liquid characteristics. Inks with high plateau moduli have higher stability while the shear yield stress can be related to the required extrusion force.

Again, the unfilled and 10 vol% fiber inks display similar properties. For the unfilled ink, the plateau modulus is 0.98×10^5 which increases by 64% to 1.61×10^5 Pa for the 20 vol% formulation. At 88%, the largest increase is between the 20 and 30 vol% loading fractions. The initial yield stress is 665 Pa and increases by 6% at 10 vol% GF, and an additional 11% and 12% for the 20 and 30 vol% fiber formulations respectively. When comparing the two properties in figure 22.b, note the difference in axis: the plateau modulus is plotted following a log scale while the shear yield stress is linear.

When printing, the 10 vol% formulation behaved similarly to the unfilled ink. It printed cleanly and reliably. However, at both 20 and 30 vol% fiber loading, increased pressure was

required for extrusion at higher (85 – 85°C versus 70°C) temperatures. These prints both experienced failure due to fiber conglomeration reducing flow volume. For the 30 vol% formulation, failure occurred approximately 3 times as often as the base ink.

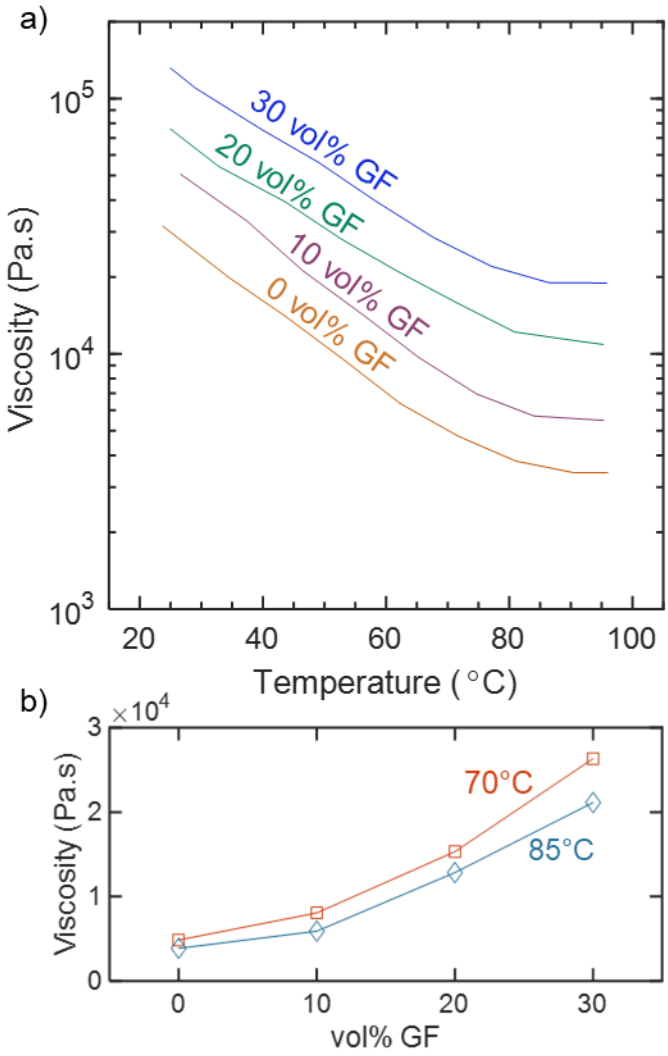

***Figure 21**. Viscosity temperature sweep. a) shows the decrease in viscosity as a function of temperature for the 4 blends while b) depicts the viscosity over the nozzle extrusion temperature range.*

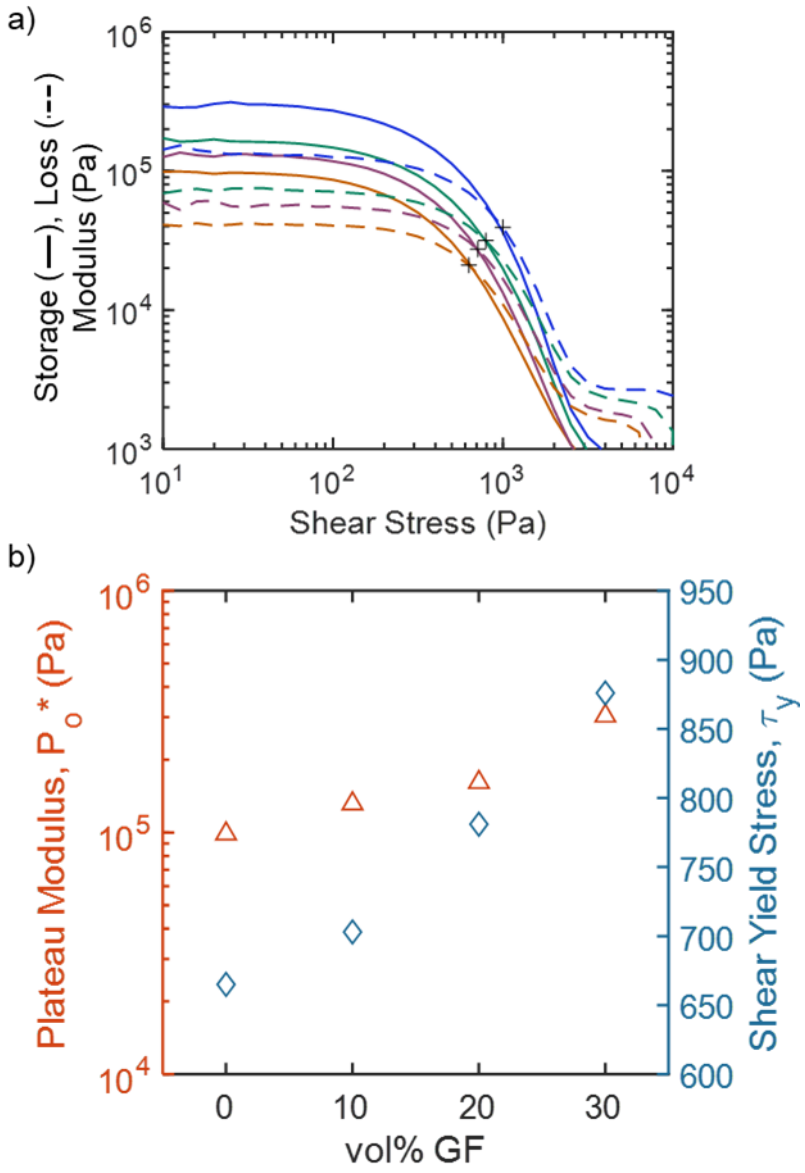

Figure 22. *Rheological oscillatory stress sweep of fiber-filled formulations at 70°C. a) storage and loss modulus versus oscillatory shear stress and b) linear viscoelastic plateau storage modulus and shear yield stress for the inks.*

5.3.2. Thermal and Mechanical Properties

The heat deflection temperature conducted at 0.455 MPa stress is shown in figure 23. The dashed line at -0.2% strain marks the temperature at which HDT is measured. For the unfilled ink, the HDT is 212°C which increases to 320°C for the fiber formulations. While there is some variation (319, 321, and 324°C increasing with fiber content), the presence of fibers yields over a 100°C increase the thermal stability.

Thermal expansion occurs until 120°C for the neat 6040 and 160°C for the fiber-filled inks. While there is variation in the degree of expansion, it does not correlate to fiber content, suggesting that this is more related to the print itself. A second plateau from 220 to 280°C is observed for the fiber-containing formulations. Above the T_g of 280°C as measured by tan(δ) in figure 24.c, deflection begins in earnest.

Figure 24 shows the (a) storage and (b) loss moduli along with (c) the tan(δ) curves from 3pt-flexure DMA both along (axially) and against (transverse to) the print direction. The glass-transition temperature ranges between 245 and 258°C when measured by the storage modulus and 279 and 284°C by peak tan(δ) for all except the 30 vol% formulation in the axial direction. Due to printing difficulties, the 30 vol% prints had surface defects that were larger than could be removed by sanding.

The largest increase (57%) in the storage modulus measured at 30°C occurs between the unfilled and 10 vol% GF formulation tested parallel to the print direction. For measurements conducted at 200 and 300°C, this trend holds. The unfilled ink had the largest decrease in modulus as the temperature increased. Although to a lesser degree, the largest improvement in the transverse direction comes from 10 vol% fiber formulation except at 30°C where the 10 to 20 fiber vol% is superior. The modulus values at 30, 200, and 300°C along with T_g are compiled in table 8.

The results of 3-point bend flexure testing are depicted in figure 25. From the representative plot in figure 25.a, there appears to be a decrease in strain-to-failure with increasing fiber content. A change in the slope appears at 2% and 1% strain for the unfilled and 10 vol% fiber formulation respectively. Both 20 and 30 vol% fiber formulations rupture soon after. Further, the apparent work-to-failure decreases with the fibers as well.

From unfilled to 30 vol% fibers, the flexure modulus (figure 25.b) increases by 160% axially from 4.93 to 13.2 GPa axially and by 60% from 4.2 to 6.9 GPa transverse. At 54% axially

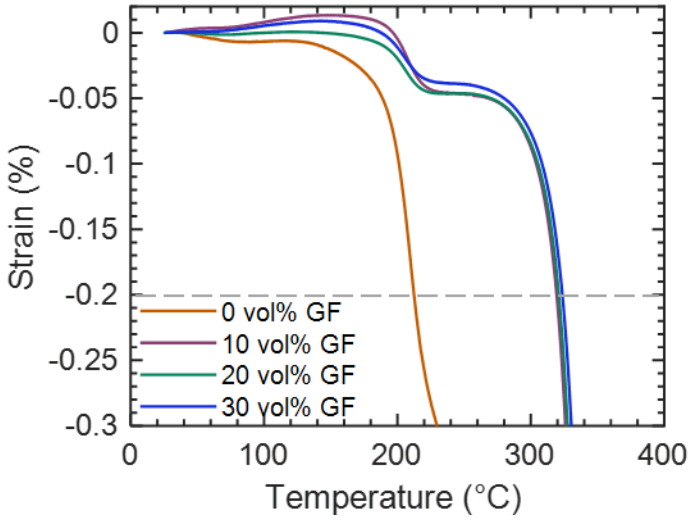

Figure 23. *Deflection temperature for the 4 inks taken at a constant stress of 0.455 MPa. The dashed line indicates -0.2% strain at which the HDT is measured.*

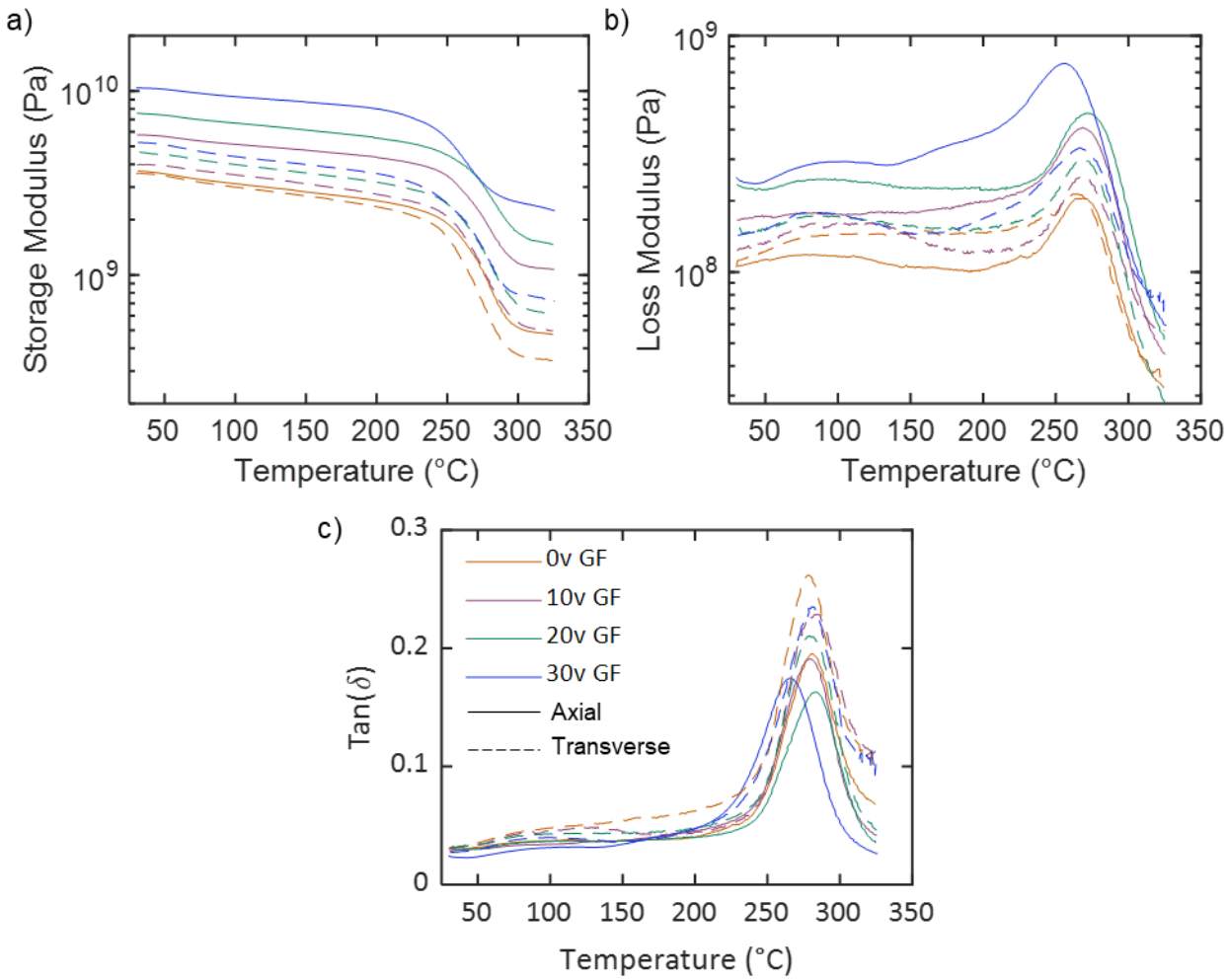

Figure 24. *3-point flexure DMA measurements as a function of temperature. (a) storage and (b) loss modulus and (c) tan(delta) curves for the 4 inks in both 0° and 90d print orientations.*

Table 8. *Storage modulus at temperature along with the T_g for the four inks.*

Fiber content		Storage Modulus (GPa)			T_g (°C)	
	(vol. %)	30°C	200°C	300°C	E'	tan(δ)
Axial	0	3.68	2.53	0.52	255	280
	10	5.78	4.37	1.15	250	279
	20	7.58	5.55	1.70	258	282
	30	10.39	8.00	2.48	240	265
Transverse	0	3.58	2.35	0.37	245	279
	10	3.98	2.74	0.55	250	284
	20	4.76	3.19	0.69	255	280
	30	5.26	3.56	0.79	250	281

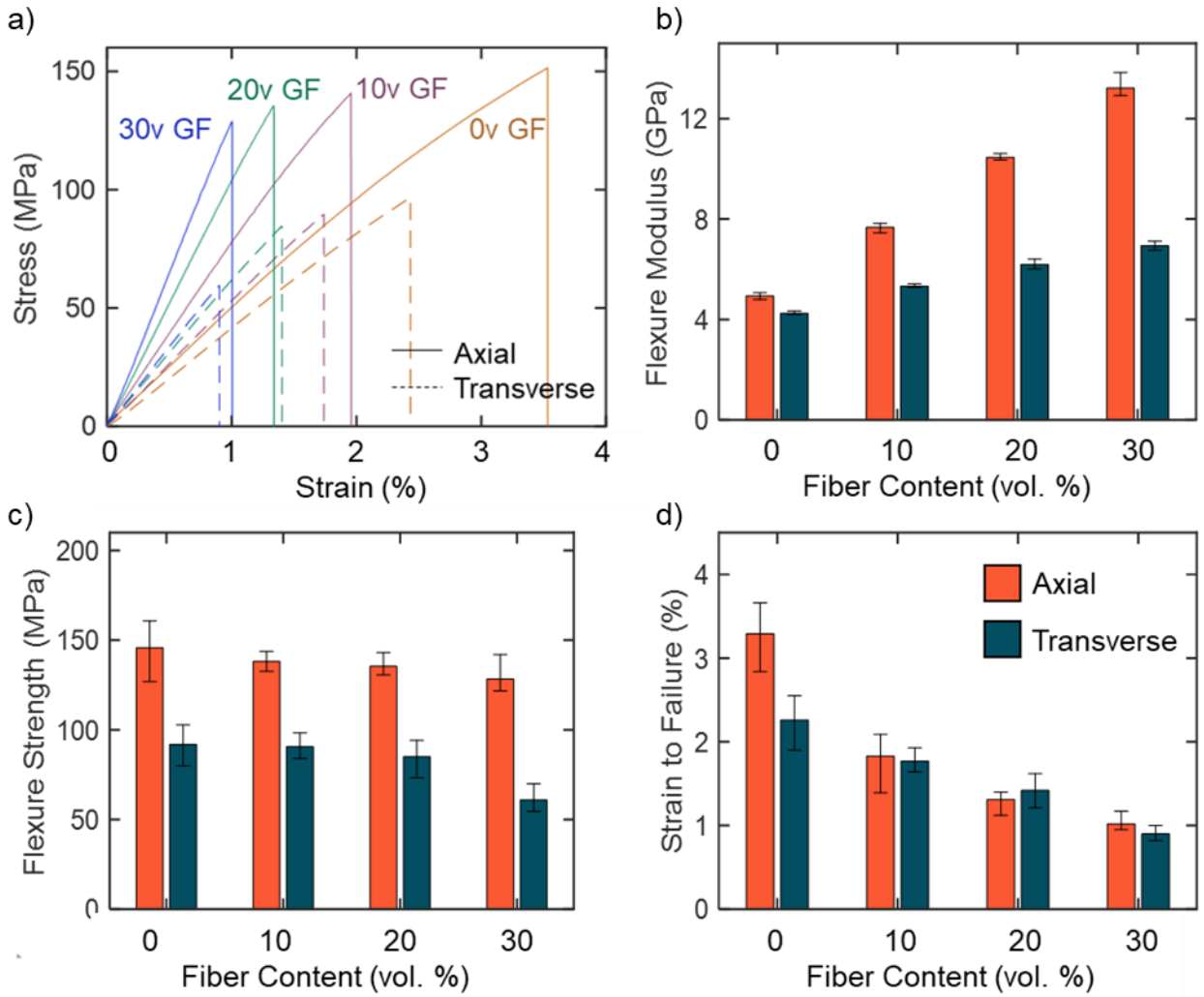

Figure 25. *3-point bend flexure testing. Representative data (a) and bar plot averages of the b) modulus, c) flexure strength, and d) strain to failure measured by 3-point flexure testing. Error bars show the maximum and minimum values from each set.*

and 25% along the print direction, the largest increase in modulus appears with the addition of 10 vol% fibers, similar to in DMA. Compared to DMA, the flexure moduli are 33% higher on average. This could be from the cooler testing environment (21 vs 30°C), sample preparation, or the testing method itself. While flexure samples were polished on both the top and bottom surfaces, DMA samples were only ground flat along the top.

While the flexure modulus increases in both print directions, the flexure strength, figure 25.c, shows a different trend. Axially, the strength remains relatively level from 146 to 138 MPa, decreasing by 10% initially and 13% in total across the 4 samples. Across the print direction, the strength remains constant until a 40% decrease between 20 and 30 vol% fibers. The expected increases in strength from the fibers are not observed. This could be from increasing porosity with fiber content as depicted in figure 26 a-d and the short fiber lengths as discussed in chapter 2.5.3.

Lastly, the strain-to-failure decreases with fiber content. With a high-crosslinking density required for a high T_g, 6040 is a brittle material. Although fiber pull-out was observed, the short fibers were unable to carry significant load. Further, the addition of short fibers decreases the amount of stretch possible by the polymer matrix. Results are summarized in table 9 and the full curves can be found in appendix B.

Images of representative axial flexure samples in figure 25.a are shown in figure 26. All images are shown in testing orientation with SEM microscopy taken away from the fracture initiation point. The relative image location in the prints vary to observe a variety of failure behavior. Optical microscopy of selected samples tested in transverse can be found in appendix C.

Optical microscopy is shown in section 1. While the unfilled, 10, and 20 vol% fiber samples (A-C) were printed individually as can be noted by the ribbed edges, the 30 vol% prints were unable to extrude and samples were cut from a previously made sheet. The short print path between turning at the edge could account for the increased number of fiber clogs [49]. In all, there appear to be more pores along the bottom surface than the top. While the pore size and frequency increase with fiber content, they appear at nodes from the print path and could be associated with under-extruding. However, increasing the extrusion pressure and decreasing the head speed had no effect. For the 30 vol% formulation, pores appear throughout the print, not limited to nodes. These vary in shape from a distorted triangle which has been observed from thermoplastic printing with improper height control [49, 92] to an rounded oblong from the fiber

Table 9. *Mechanical properties of the printed fiber composites.*

	Fiber Content (vol %)	Flexure Modulus (GPa)	Peak Stress (MPa)	Failure Strain (%)	# samples
Axial	0	4.93 (± 0.14)	145.8 (± 19)	3.29 (± 0.45)	6
	10	7.61 (± 0.29)	131.6 (± 5.6)	1.83 (± 0.44)	6
	20	10.40 (± 0.33)	131.1 (± 7.7)	1.31 (± 0.19)	6
	30	13.18 (± 0.66)	128.4 (± 13.6)	1.02 (± 0.15)	6
Transverse	0	4.26 (± 0.08)	91.9 (± 12.1)	2.26 (± 0.36)	6
	10	5.33 (± 0.09)	90.6 (± 7.7)	1.77 (± 0.16)	6
	20	6.19 (± 0.21)	85.0 (± 11.8)	1.42 (± 0.21)	6
	30	6.97 (± 0.21)	61.0 (± 8.9)	0.90 (± 0.10)	7

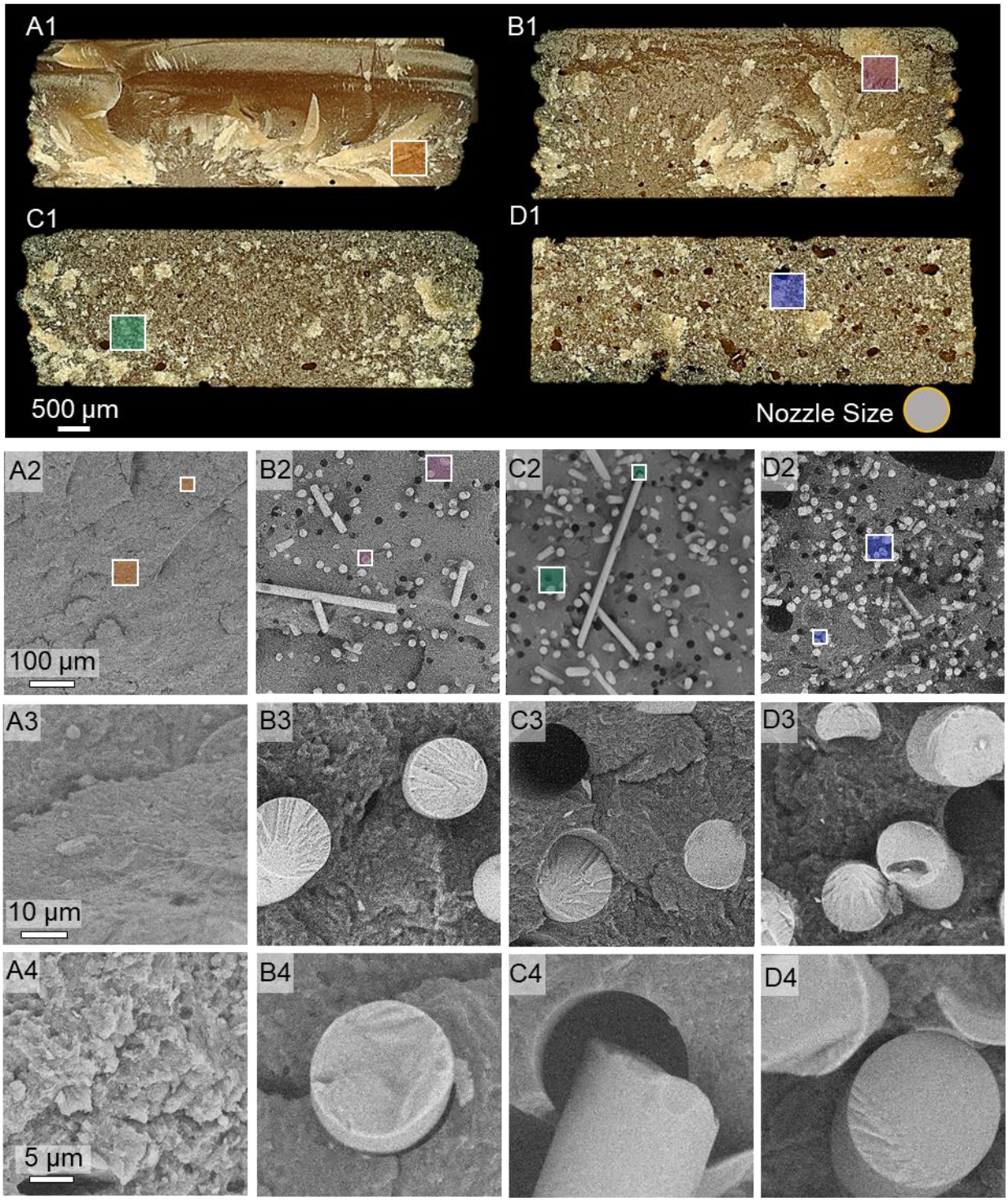

***Figure 26**. Micrographs of fracture surfaces from flexure testing of axially printed samples. (A) 0 vol% GF, (B) 10 vol% GF, (C) 20 vol% GF, and (D) 30 vol% GF. Set X1) is taken using optical Keyence microscopy at 50x while X2-4) are from SEM at 500x, 5,000x, and 10,000x respectively. The highlighted boxes in X2 correlate to X3 (larger) and X4 (smaller) of the same series.*

content. At high loading volumes, inconsistent and irregular flow can account for inadequate volume control.

Both the unfilled and 10 vol% fiber formulations show a fracture initiation point. The unfilled 6040 (A1) begins to break at a stress concentration in the lower middle of the print. At 10 vol% fibers (B1), the failure began from a subsurface pore on the lower left side. Failure progresses smoothly and the print splits into two even pieces. Neither the 20 (C1) nor 30 vol% (D1) have a clear fracture initiation point. For both, surface defects are present along the bottom surface that were unable to be polished away. These defects likely acted as stress concentrations. However, there is no smooth region indicating a failure zone. While all unfilled tests broke in 3 pieces with a triangular section breaking off the bottom half, the fiber-filled samples split vertically into two halves with visible fibers extruding past the fracture surface.

The first set of SEM images (row 2) are taken at 500x magnification. Here, the images are the size of the nozzle although specific locations along the print paths are unknown. In all SEM images of the unfilled sample, surface roughness is visible. Looking at B2-D2, fibers appear oriented along the print direction as determined by circular cross-sections. The percentage of non-oriented fibers increases with fiber content. There appears to be some preferential distribution with rows of fibers separated by matrix material. Both the 10 (B2) and 20 (C2) vol% fiber prints show long fibers laying across the fracture surface. These appear to have been pulled from the matrix during fracture before falling on the surface. At 30 vol% (D2), the fibers have clumped and this long fiber pull is less common. However, irregular sized pores can be observed along the upper and left side of the image.

Neither 20 nor 30 vol% show evidence of crack propagation. At 5,000x magnification (row 3), individual fiber rupture is visible. Image B3 falls along a fracture path and the two fibers have ruptured from seemingly different directions. This suggests that at this location in the print, there are multiple crack propagation paths. In C3, evidence of three fibers is shown. Clockwise from the upper left corner, the first fiber was pulled out and removed by the other half of the sample. The second shows a smooth surface with no evidence of fracture. Lastly, a clear initiation point is present and fracture appears to travel towards the upper left corner, towards the center of the sample. At 30 vol% loading (D3), fibers are concentrated. Surface defects are visible which could be from the high loading and resultant shear during mixing.

The last series (row 4, 10,000x magnification) shows individual fiber pullout. Comparing the neat 6040 surface with fiber filled, the matrix roughness appears to decrease around fibers.

Image B4 depicts the start of fiber-matrix deboning. In C4, the end of a pulled fiber shows surface texture of both the matrix and fiber. Lastly, fiber-fiber interactions at 30 vol% loading (D4) are visible.

5.4. Discussion

5.4.1. Fiber Length and Printability

Glass fibers show promise for processing in this method as compared to carbon fibers. A similar study by Pierson *et al.* had a 95% reduction in size at similar mixing parameters [49]. However, longer initial fibers are essential. While shorter fibers allow for a higher fiber loading, 60% of the given fibers are an ineffective length leading to decreased properties.

With polymer AM, fibers are included to improve the strengths of the matrix; for extrusion-based systems, processing requirements dictate the maximum loading. Higher fiber concentrations increase the ink viscosity, reducing the flowability and lead to clogging in the nozzle which can stop printing entirely. Unlike resin, fibers do not decrease in viscosity as the temperature increases. As such, the effect of heating the resin for extrusion reduces with higher fiber loading formulations. The minimum viscosity prior to the addition of curing agent is reached at 95°C for all blends. Further increasing the temperature above 85°C for the 30 vol% formulation would result in premature crosslinking. Additionally, the less viscous resin would reduce the matrixes ability to carry fibers increasing the likelihood of fibers clogging in the nozzle during extrusion.

Although there is greater variation in plateau modulus than the shear yield stress across fiber contents, these do not accurately predict flow behavior. From these, the 10 and 20 vol% formulations have the most similar values and could be expected to behave similarly. This is not the case. While additional factors also negatively impact print behavior, such as increased fiber conglomeration in the nozzle with fiber content, this can be observed from decreasing flow throughout the duration of the print until failure. Although this does occur at high loading fractions, particularly at 30 vol% fiber loading, it does not account for poor extrusion behavior at the onset of printing. Rather, the shear yield stress describes the extrusion behavior. At 70°C, over 800 Pa of shear force is required for the 30 vol% fiber ink to flow. With current capabilities, this is unable to be provided and the temperature must be increased. The shear yield stress for the

unfilled and 10 vol% formulations fall between 650 and 700 Pa. Both readily flow at moderate (40 – 50 psi) extrusion pressures and print well.

For this epoxy system, 10 vol% fiber loading behaves similarly to the unfilled ink. Unlike the 20 and 30 vol% fiber inks, the resin extrudes smoothly throughout the entire print. As the fiber content increases, issues with printing due to nozzle clogging and resin curing become more common. As the fiber content increased to 20 vol%, flow was not accessible using this extrusion system. Increasing the temperature to 75 and 85°C for the 20 and 30 vol% fiber formulations allowed for printing. However, fiber clogging was prevalent where the 30 vol% formulation failed due to inadequate flow mid-print approximately 3 times as often. For both formulations, resin remaining in the heated nozzle without flow began to crosslink and gelled in under 30 minutes. This is due to the decreased volume of resin in the system leading to a lower activation energy per mass.

5.4.2. Printed Properties

Thermally, the presence of fibers increases the HDT regardless of the concentration. Because of this, the 10 vol% GF formulation, which has the best processing characteristics, is sufficient for property improvement. There is minimal change in the glass transition temperature with fiber content.

Figure 27 shows the storage modulus anisotropy factor from DMA (figure 24) with respect to temperature. As predicted, the difference between the two print directions increases with both temperature and fiber content. For the unfilled blend below the glass transition temperature (T_g = 250 – 285°C from E' and tan(δ) respectively), the anisotropy factor remains at 1 ± 0.5 showing good interlayer adhesion. This supports the claim that the post cure of the part improves the overall uniformity. As fiber content increases, this factor increases with all 30 vol% fiber prints in the axial direction being more than twice that in the transverse. At 10 vol% fiber loading, this factor remains at 1.5 ± 0.9 from RT to 200°C. The close correlation is encouraging because it suggests that, although properties decrease with temperature, they follow a similar rate. However, the increase above the glass transition temperature indicates that the interlayer bonds are the weakest and print direction will become more pronounced at elevated temperatures.

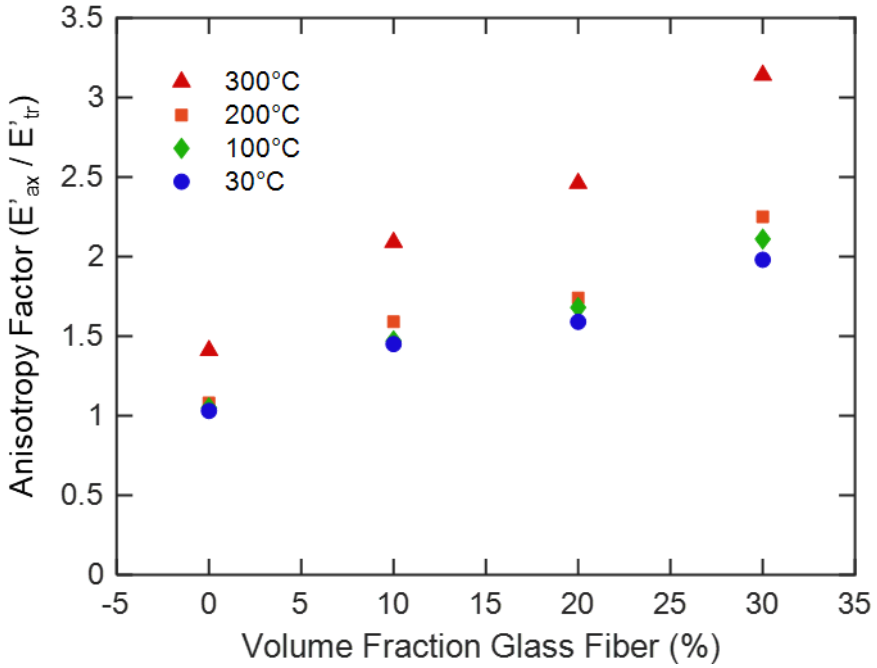

***Figure 27**. Anisotropy factor from DMA storage moduli at 30, 100, 200, and 300°C as a function of fiber content.*

Although the modulus does increase with fiber loading, it is to a lesser degree than expected. Figure 28 shows the flexure moduli plotted against the upper and lower bounds and Halpin-Tsai predictions. The upper bound is given by the rule of mixtures (eq. 17) while the lower bound is given by the harmonic mean (eq. 18).

By the Halpin-Tsai model, the fiber shape and length are accounted for through ξ, but fibers are assumed to be fully aligned. With a 16 um fiber diameter and an average fiber length falling between 200 and 266 μm, the Halpin-Tsai shape factor for aligned fibers, ξ, ranges from 25 to 46 as shown in table 10. The shape factor is 2 for the samples tested 90° from the print direction. However, when using these values, predicted values are 50 – 50% higher than observed. From qualitative fitting, a shape factor of 8 fits the axial data while 0.5 fits the transverse.

From optical microscopy, pores are prevalent in each print. Accounting for the void content following Boccaccini's model, the effective matrix moduli decreases by 36% from unfilled to the 30 vol% ink. Using this modulli with Halpin-Tsai's model and the calculated shape factor, the predicted flexure moduli comes within 7% of the measured values. Additional considerations of the fiber orientation and adhesion will further reduce the moduli.

Fiber-filled composites are commonly vacuum sealed during the cure to prevent the formation of pores [180]. However, one of the benefits of AM is the lack of molds required. Although pores are an issue, traditional methods of removing these during the cure negate the benefits of printing. In all of the prints, the voids fall predominantly along the bottom surface. This could be due to insufficient flow early in the print, the nozzle temperature not equilibrating, or the wrong initial print height. With the given system, the print is operating at the maximum temperature and pressure. However, prints were run at two different print speeds, 18 and 20 mm/s, with the same behavior occurring at both suggesting that insufficient flow is not the culprit. Although slower speeds could be tested, this is unreasonable for practical applications. Further, if this were the case, voids would be likely to be found throughout the print as print behaviors remain consistent. Because the bottom and top surfaces are polished prior to testing which removed 5 – 10% of the total thickness on average, an initial row height mismatch is less likely. These location and shape of these defects are reminiscent of those seen using a FFF system for a thermoplastic [49, 85]. Because of this, the issue is likely related to the nozzle temperature

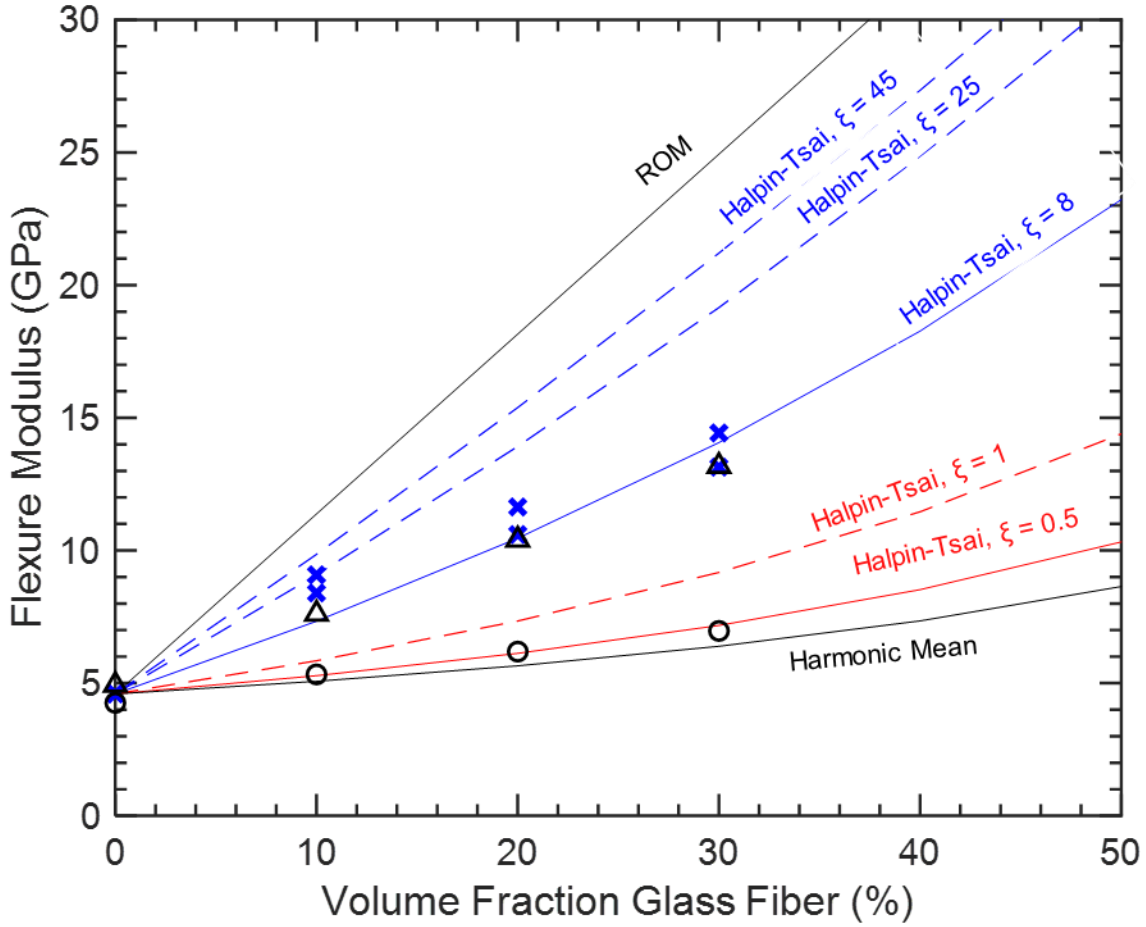

Figure 28. *Flexure moduli values plotted against the upper (ROM) and lower (harmonic mean) bounds and Halpin-Tsai approximations. The dashed Halpin-Tsai lines indicate calculated ξ factors while the solid are experimentally fitted. The blue X's mark the Halpin-Tsai limits after accounting for pores in the matrix.*

Table 10. *Measured and calculated flexure moduli with relevant fitting parameters for both Halpin-Tsai and Boccaccini's approximations.*

vol. GF (%)	avg. fiber length (μm)	ξ	η	vol. pores (%)	$E_{m,\ eff}$ (GPa)	Flexure Modulus (GPa)		
						H-T	H-T w/ pores	measured
0	-	-	-	0	4.93	4.93	4.93	4.93
10	260	45	0.229	4	3.93	9.56	8.18	7.61
20	200	24	0.354	9	3.48	13.34	10.18	10.40
30	366	46	0.229	14	3.15	20.21	13.79	13.18

during early extrusion and pauses between prints. However, that falls outside the scope of this work. While this work provides a proof of concept for glass fiber printability, a sizing factor will be required for continued work. Additionally, at 20 and 30 vol% fiber loading, the fracture surfaces indicate a high percentage of voids and surface defects.

Strength values were expected to increase. Even accounting for the void content using Boccaccini's model, the failure strengths fall below the predicted values. The lack of increase could be due to the amount of short fibers and possible poor fiber-matrix bonding. Prior to incorporation to the matrix, 15 vol% of the fibers were already below the critical fiber length. These fibers did not notably contribute to the final strength of the composite and could have decreased the strength of the matrix. Rather than measuring the critical fiber length, an approximation using the matrix and fiber strengths was utilized. As such, the actual critical length could have been longer leading to a larger negative effect of the short fibers. Additionally, although the fibers did not experience breakage during mixing, a high shear process was incorporated. Heat produced from fiber impact and friction raised the temperature to upwards of 110dC immediately after removal from the mixer. While the fibers may not have fractured, surface defects could decrease the initial fiber strength and cause weak spots that prematurely ruptured. However, at this time, that falls outside of the scope of this work.

5.5. Conclusions

This work incorporated up to 30 vol% glass fibers to a high temperature, high viscosity epoxy matrix. Unlike carbon fibers, processing did not break the fibers. This allows for longer mixing, assumedly better incorporation, and a larger importance on initial fiber size. However, milled fibers were selected which lead to a varied initial fiber length with 50% of fibers below the critical length for this system.

Increasing the fiber content led to worse printing conditions with the extrusion nozzle clogging for both the 20 and 30 vol% fiber formulations. An upper viscosity limit was found at 30 vol% GF although voids were common and independent of printing. Further, extrusion behavior was unpredictable and with failure during printing occurring in over 60% of all prints.

The presence of fibers was able to improve the heat deflection temperature by over 100°C with no additional improvement from an increased fiber content. The 10 vol% glass fiber formulation extruded smoothly and improved the modulus by 54% along the print directions and 25% against it. Glass fibers present a viable filler material for AM applications. Further, using a

larger extrusion nozzle, as would be required for scaling, will allow for longer fibers to be used allowing for additional improvements.

CHAPTER SIX
CONCLUSIONS

In this study, a high-temperature (T_g > 200°C), glass-fiber filled, epoxy resin feedstock was developed for direct-ink write additive manufacturing. From experimental results and observations, the following conclusions can be drawn:

Although “high temperature” epoxies exist, the criteria can be vague and the curing agent plays a large role in the final properties. Although using DDS as the curing agent can increase the glass transition temperature by more than 100°C as compared to VS03 or DICY, it is unable to readily incorporate at moderate temperatures. When mixed at elevated temperatures, DDS increases the uncured T_g and solidifies liquid resins.

While a solvent-based extrusion method would allow for solid epoxies to be utilized, the solvent is unable to escape from bulk material leading bubbling and an uneven surface. Further, if printed with solvent, the epoxy-nanoclay system does not maintain sufficient shear thinning behavior that gives printed parts stability. However, if provided stability, such as with microballoons for a syntactic foam, the printed solution could maintain structure during extrusion. Provided that printed parts have thin walls, microballoons could provide stability as excess solvent leaves the printed system. As such, the high temperature solid epoxies and DDS could be incorporated and printed.

By using a warmed extrusion process, some of the beneficial properties from FFF of thermosets can be achieved. The previous layers solidify as they cool providing a solid base which allows for higher degrees of overhang. However, because a secondary cure is required, issues with interlayer bonding and delamination are less. As such, this process produces smooth prints that, provided that the structure is maintained during the cure, can achieve complex geometries with similar (4.59 ± 0.34 GPa) flexural modulus behavior regardless of the print direction.

The blending of two resins reduced the viscosity, allowing for nanoclay to be incorporated and a warmed extrusion process to be possible. The miscibility was determined by the glass transition temperature and lack of phase separation. By comparing to Epon 826, a common epoxy for printed systems, a target “extrudable” viscosity was able to be selected. Mixed properties followed ROM and a 60:40 blend of HP-7250 and HP-4032SS was selected with a T_g

of 210°C and 55°C as the processing temperature. However, with the current system, the nozzle had to be held at a higher temperature for the resin to flow. Further rheological work showed that this system has a 48+ hour pot life at 50°C which reduced to 18 hours at 70°C which allowed for sufficient extrusion time before cure began.

Because many high temperature epoxies are developed for thin-film applications, the prescribed cure process is unable to be observed when scaling up the volume. Crosslinking is a highly exothermic reaction and the produced heat can lead to autoacceleration. Further, parts produced by DIW must remain rigid during a heated cure. As the temperature increases, the crossover point between the storage and loss moduli decrease and stability is lost. A pre-cure step at a low temperature (70 – 85°C) increases the stability while also managing the heat released from the reaction.

The addition of glass fibers improved the flexure modulus. However, the failure stresses remained consistent (134 ± 12 MPa) along the print direction and decreased by 30 MPa in the transverse direction. Although glass fibers experience less breakage during processing than carbon fibers, the as-received milled fibers exhibited a large (20 - 1300 μm) length distribution. Additional work can sieve the fibers to remove those which are below the critical length. Doing so will improve the fibers effectiveness and improve strength values.

At 20 and 30 vol% fiber loading concentrations, fiber clogging becomes increasingly relevant and can be detrimental to printing. When printing with 30 vol%, failure occurred 3 times as often. However, the 10 vol% formulation printed similarly to the unfilled resin and fiber clogging was minimal. Thermally, the presence of fibers improves the HDT by 100°C regardless of the concentration. Mechanically, higher fiber contents do increase the strength and modulus but at diminishing rates. The largest stepwise increase in modulus is from 0 to 10 vol% glass fibers. As such, this formulation is recommended for continued work.

Continued work needs to include lifetime analysis at elevated temperatures. Although a heat deflection temperature of 320°C is encouraging, HDT is a single short-term data point. Creep testing will provide better insight to the upper temperature limit for extended periods of time.

The impact of fiber length, loading volume, and resin viscosity on fiber clogging needs to be understood and modeled. While longer fibers improve strength values more so than shorter fibers, they can also increase extrusion difficulties.

LIST OF REFERENCES

1. Quan, Z., et al., *Microstructural design and additive manufacturing and characterization of 3D orthogonal short carbon fiber/acrylonitrile-butadiene-styrene preform and composite.* Composites Science and Technology, 2016. **126**: p. 139-148. DOI: 10.1016/j.compscitech.2016.02.021.
2. Huang, Y., et al., *Additive Manufacturing: Current State, Future Potential, Gaps and Needs, and Reccomendations.* Journal of Manufacturing Science and Engineering, 2015. **137**. DOI: 10.1115/1.4028725.
3. Masters, W.E., *Computer automated manufacturing process and system*, U.S.P.a.T. Office, Editor. 1984: United States.
4. Post, B.K., et al., *Feasibility of using Big Area Additive Manufacturing to Directly Manufacture Boat Molds.* 2018. DOI: 10.2172/1427645.
5. Post, B., et al. *Large-Scale Additive Manufacturing for Low Cost Small-Scale Wind Turbine Manufacturing*. 2019.
6. Kemp, J.W., N.S. Hmeidat, and B.G. Compton, *Boron nitride-reinforced polysilazane-derived ceramic composites via direct-ink writing.* Journal of the American Ceramic Society, 2020. DOI: 10.1111/jace.17084.
7. Sames, W.J., et al., *The metallurgy and processing science of metal additive manufacturing.* International Materials REviews, 2016. **61**(5): p. 315 - 360. DOI: 10.1080/09506608.205.111649.
8. Chin, S.Y., et al., *Additive manufacturing of hydrogel-based materials for next-generation implantable medical devices.* Science Robotics, 2017. **2**(2). DOI: 10.1126/scirobotics.aah6451.
9. Han, X., et al., *An In Vitro Study of Osteoblast Response on Fused-Filament Fabrication 3D Printed PEEK for Dental and Cranio-Maxillofacial Implants.* Journal of Clinical Medicine, 2019. **8**(6): p. 771. DOI: doi.org/10.3390/jcm8060771.
10. Hao, L., et al., *Material characterisation and process development for chocolate additive layer manufacturing.* Virtual and Physical Protyping, 2010. **5**(2): p. 57 - 64. DOI: 10.1080/17452751003753212.
11. Garrett, B., *3D Printing: New Economic Paradigms and Strategic Shifts.* Global Policy, 2014. **5**(1): p. 70 - 75. DOI: 10.1111/1758-5899.12119.
12. Obama, B.P., *Remarks by the President in the State of the Union Address*. 2013: The White House.
13. Feldman, A., *Meet the Italian Engineers 3D-Printing Respirator Parts for Free to Help Keep Coronavirus Patients Alive.* Forbes, 2020.
14. Selko, A., *Using 3D to Print Face Shields to Help Ease Shortage Due to Virus.* EHS Today, 2020.
15. Tamburin, A., *Tennessee colleges mass producing face shields to guard against coronavirus using 3D printers.* Tennessean, 2020.
16. *Engineering Students Producing 3D Printed Face Shields for Healthcare Professionals*. 2020.
17. Franchetti, M. and C. Kress, *An economic analysis comparing the cost feasibility of replacing injection molding processes with emerging additive manufacturing techniques.* Int. J. Adv. Manuf. Technol., 2016. **88**: p. 2573 - 2579. DOI: 10.1007/s00170-016-8968-7.
18. Sabiston, G. and I.Y. Kim, *3D topology optimization for cost and time minimization in additive manufacturing.* Structural and Multidisciplinary Optimization, 2020. **61**(731 - 748). DOI: 10.1007/s00158-019-02392-7.
19. Wohlers, *Wohlers Report 2020: 3D Printing and Additive Manufacturing, Global State of the Industry*. 2020.
20. Ngo, T.D., et al., *Additive Manuractureing (3D printint): A review of materials, methods, applicaitons, and challenges.* Composites Part B: Engineering, 2018. **143**: p. 172 - 193. DOI: 10.1016/j.compositesb.2018.02.012.

21. Gaskill, M., *Solving the Challenges of Long Duration Space Flight with 3D Printing*, M. Johnson, Editor. 2019, National Aeronautics and Space Administration International Space Station Program Science Office.
22. *Porsche Classic supplies classic part from a 3D printer*. 2018; Available from: https://newsroom.porsche.com/fallback/en/company/porsche-classic-3d-printer-spare-parts-slsprinter-production-cars-innovative-14816.html.
23. Toberer, N., *Porsche presents innovative 3D-printing technology for buket seats*. 2020, Porsche Newsroom.
24. Aetrex. *Aetrex 3D Printed Orthotics*. [cited 2020; Available from: https://www.aetrex.com/3D-printing.html.
25. Wohlers, T., *3D printing and additive manufacturing state of the industry.* Wohlers Report: Annual Worldwide Progress Report, 2018.
26. Wolfsburg. *Ready for mass production: Volkswagen uses latest 3D printing processes for production*. 2018.
27. Calvert, P., T.L. Lin, and H. Martin, *Extrusion freeform fabrication of chopped-fibre reinforced composites.* High Performance Polymers, 1997. **9**: p. 499-456.
28. Sachs, E.M., et al., *Three-dimensional printing techniques*, U. Patent, Editor. 1993.
29. Cesarano, J., III., et al., *Freeforming of Ceramics and Composites from Colloidal Slurries.* 1999. DOI: 10.2172/15159.
30. Cesarano, J., III. and P.D. Calvert, *Freeforming objects with low-binder slurry*, U.S.P.a.T. Office, Editor. 2000, Sandia Corporation: United States.
31. M'Barki, A., L. Bocquet, and A. Stevenson, *Linking Rheology and Printability for Dense and Strong Ceramics by Direct Ink Writing.* Scientific Reports, 2017. **7**(1): p. 6017. DOI: 10.1038/s41598-017-06115-0.
32. Rueschhoff, L., et al., *Additive Manufacturing of Dense Ceramic Parts via Direct Ink Writing of Aqueous Alumina Suspensions.* Applied Ceramic Technology, 2016. **13**(5): p. 821 - 830. DOI: 10.1111/ijac.12557.
33. Valentine, A.D., et al., *Hybrid 3D Pritning of Soft Electronics.* Advanced Materials, 2017. **29**(40). DOI: 10.1002/adma.201703817.
34. Skylar-Scott, M.A., et al., *Biomanufacturing of Organ-Specific Tissues with High Cellular Density and Embedded Vascular Channels.* Science Advances, 2019. **5**. DOI: 10.1126/sciadv.aaw2459.
35. Compton, B.G. and J.A. Lewis, *3D-Printing of Lightweight Cellular Composites.* Advanced Materials, 2014. **26**: p. 5930-5935.
36. Compton, B.G., et al., *Electrical and Mechanical Properties of 3D-Printed Graphene-Reinforced Epoxy.* Jom, 2017. **70**(3): p. 292-297. DOI: 10.1007/s11837-017-2707-x.
37. Hmeidat, N.S., J.W. Kemp, and B.G. Compton, *High-strength epoxy nanocomposites for 3D printing.* Composites Science and Technology, 2018. **160**: p. 9-20. DOI: 10.1016/j.compscitech.2018.03.008.
38. Liravi, F. and E. Toyserkani, *A hybrid additive manufacturing method for the fabrication of silicone bio-structures: 3D printing optimization and surface characterization.* Material & Design, 2018. **138**(15): p. 46 - 61. DOI: 10.1016/j.matdes.2017.10.051.
39. Sachs, E., et al., *Three dimensional printing: Rapid tooling and prototypes directly from a CAD model.* Journal of Enginnering for Industry 1992. **144**(4): p. 481 - 488. DOI: 10.1115/1.2900701.
40. Ligon, S.C., et al., *Polymers for 3D Printing and Customized Additive Manufacturing.* Chemical Reviews, 2017. **117**. DOI: 10.1021/acs.chemrev.7b00074.
41. Romberg, S.K., et al., *Large-Scale Additive Manufacturing of Highly Exothermic Reactive Polymer Systems*, in *SAMPE*. 2019: Charlotte, NC.

42. Algahtani, M.S., A.A. Mohammed, and J. Ahmad, *Extrusion-Based 3D Printing for Pharmaceuticals: Contemporary Research Applications.* Current Pharmaceutical Design, 2018. **24**(42): p. 4991 - 50008. DOI: 10.2174/1381612825666190110155931.
43. Liu, T., et al., *A nitrogen-free tetrafunctional epoxy and its DDS-cured high performance matrix for aerospace applications.* Ind. Eng. Chem. Res., 2017. DOI: 10.1021/acs.iecr.7b00096.
44. Wilson, D., *Polyimide Matrix Composites: Canidates for High Speed Commercial Aircraft or not?* High Performance Polymers, 1991. **3**(2): p. 73 - 87. DOI: 10.1088/0954-0083/3/2/002.
45. Kishore, V., *Melt Processability and Post-Processing Treatment of High Temperature Semi-Crystalline Thermoplastics for Extrusion Deposition Additive Manufacturing*, in *Energy Science and Engineering*. 2018, University of Tennessee. p. 127.
46. Ajinjeru, C., et al., *The Influence of Rheology on Melt Processing Conditions of Amorphous Thermoplastics for Big Area Additive Manufacturing (BAAM)*, in *Solid Freeform Fabrication Symposium*. 2016.
47. Thakker, J.R., et al., *Glass fiber reinforced composites of epoxy cured with different amines* Macromolecular and Materials Engineering, 1989. **172**(1): p. 103 - 111. DOI: 10.1002/apmc.1989.051720109.
48. Silva, A.A., et al., *New epoxy systems based on ionic liquid.* Polymer, 2013. **54**(8): p. 2123 - 2129. DOI: 10.1016/j.polymer.2013.02.021.
49. Pierson, H.A., et al., *Mechanical Properties of Printed Epoxy-Carbon Fiber Composites.* Experimental Mechanics, 2019. **59**(6): p. 843-857. DOI: 10.1007/s11340-019-00498-z.
50. Jubsilp, C., T. Takeichi, and S. Rimdusit, *Physical and Chemical Properties of Benzoxazine Resins.* 2011.
51. Sigma-Aldrich, *1,1'-(Methylenedi-4,1-phenylene)bismaleimide Safety Data Sheet.* 2020.
52. Plenco, *Plenco 02567 phenol-formaldehyde polymer Safety Data Sheet.* 2017.
53. Agag, T. and T. Takeichi, *Synthesis and Characterization of Novel Benzoxazine Monomers Containing Allyl Groups and their High Performance Thermosets.* Macromolecules, 2003. **36**: p. 6010 - 6017. DOI: 10.1021/ma021775q.
54. Pittroff, R.R., *Relationship between the physical properties and curing system of an epoxy matrix material*, in *Mechanical Engineering*. 2007, Tshwane University of Technology.
55. *Appendix 1: EPON Resin - Curing Agent Systems*, in *EPON Resin Structural Reference Manual - EPI-CURE Curing Agents* 2001, Resolution Performance Products.
56. Bibin, J. and C.P.R. Nair, *Syntactic Foams*, in *Handbook of Thermoset Plastics*, H. Dodiuk and S.H. Goodman, Editors. 2014, Elsevier.
57. Rinaldi, M., et al., *Additive layer manufacturing of poly (ether ether ketone) via FDM.* Composites Part B: Engineering, 2018. **145**: p. 162-172. DOI: 10.1016/j.compositesb.2018.03.029.
58. Guo, Y. and R.D. Bradshaw, *Isothermal physical aging characterization of Polyether-ether-ketone (PEEK) and Polyphenylene sulfide (PPS) films by creep and stress relaxation.* Mech Time-Depend. Mater., 2007. **11**: p. 61-89. DOI: 10.1007/s11043-007-9032-7.
59. MatWeb. *Overview of materials for Polyetheretherketone, Unreinforced*. [cited June 2020.
60. Wu, T., et al., *Additively manufacturing high-performance bismaleimide architectures with ultraviolet-assisted direct ink writing.* Materials and Design, 2019. **180**. DOI: 10.1016/j.matdes.2019.107947.
61. Solvay, *Solvay HDTM 556 BMI data sheet*
62. Solvay, *Solvay CYCOM 5250-4 BMI Prepreg Neat Resin.*

63. Takeichi, T., T. Kawauchi, and T. Agag, *High Performance Polybenzoxazines as a Novel Type of Phenolic Resin.* Polymer Journal, 2008. **40**: p. 1121-1131. DOI: 10.1295/polymj.PJ2008072.
64. Lin, C.H., et al., *Low Dielectric Thermoset. IV. Synthesis and Propertiesof a Dipentene-Containing Cyanate Ester and ItsCopolymerization with Bisphenol A Dicyanate Ester.* Journal of Polymer Science: Part A, 2003. **42**: p. 3986 - 3995. DOI: 10.1002/pola.20226.
65. Rabilloud, G., *Adhesives for Electronics*, in *Handbook of Adhesives and Surface Preperation*, S. Ebnesajjad, Editor. 2011, Elvisear.
66. Love, L.J., et al., *The Importance of Carbon Fiber to Polymer Additive Manufacturing.* Journal of Materials Research, 2014. **29**(17): p. 1893 - 1898. DOI: 10.1557/jmr.2014.212.
67. Ning, F., et al., *Additive manufacturing of carbon fiber-reinforced plastic composites using fused deposition modeling: Effects of process parameters on tensile properties.* Journal of Composite Materials, 2017. **51**(4): p. 451 - 462. DOI: 10.1177/0021998316646169.
68. MatterHackers, *3D Printer Filament Technical Data Sheet.* 2020.
69. Weiss, K.-P., et al., *Thermal and mechanical properties of selected 3D printed thermoplastics in the cryogenic temperature regime.* IOP Conference Series: Materials Science and Engineering, 2015. **102**. DOI: 10.1088/1757-899X/102/1/012022.
70. Prashantha, K. and F. Roger, *Multifunctional properties of 3D printed poly(lactic acid)/graphene nanocomposites by fused deposition modeling.* Journal of Macromolecular Science, Part A, 2016. **54**(1): p. 24 - 29. DOI: 10.1080/10601325.2017.1250311.
71. Senatov, F.S., et al., *Mechanical properties and shape memory effect of 3D-printed PLA-based porous scaffolds.* Journal of the Mechanical Behavior of Biomedical Materials, 2016. **57**: p. 139 - 148. DOI: 10.1016/j.jmbbm.2015.11.036.
72. MatWEb. *Overview of materials for Polylactic Acid (PLA) Biopolymer*. [cited June 2020.
73. Hull, D., *An Introduction to Composite Materials*. Cambridge Solid State Science Series, ed. R.W. Cahn, E.A. Davis, and I.M. Ward. 1981, Cambridge, NY: University of Cambridge.
74. Theriault, R.P. and T.A. Osswald, *A Numerical Model of the Viscosity of an Epoxy Prepreg Resin System.* Polymer Composites, 1999. **20**(5): p. 628 - 633.
75. Patel, A., O. Kravchenko, and I. Manas-Zloczower, *Effects of Curing Rate on the Microstructure of Epoxy Fiberglass Composites.* Polymers, 2018. **10**(125).
76. Mangalgiri, P.D., *Composite materials for aerospace applications.* Bull. Mater. Sci., 1999. **22**(3): p. 657 - 664.
77. Huang, R., et al., *Energy and emissions saving potential of additive manufacturing: the case of lightweight aircraft components.* Journal of Cleaner Production, 2016. **135**: p. 1559-1570. DOI: 10.1016/j.jclepro.2015.04.109.
78. Immarigeon, J.P., et al., *Lightweight materials for aircraft applications.* Materials Characteristion 1995. **31**(1): p. 41 - 67. DOI: 10.1016/1044-5803(95)00066-6.
79. Fan, J. and J. Njuguna, *An introduction to lightweight composite materials and their use in transport structures*, in *Lightweight Composite Structures in Transport*. 2016, Science Direct. p. 3 - 34.
80. Nawafleh, N. and E. Celik, *Additive manufacturing of short fiber reinforced thermoset composites with unprecedented mechanical performance.* Additive Manufacturing, 2020. **33**: p. 101109. DOI: 10.1016/j.addma.2020.101109.
81. Ning, F., et al., *Additive manufacturing of carbon fiber reinforced thermoplastic composites using fused deposition modeling.* Composites Part B: Engineering, 2015. **80**: p. 369-378. DOI: 10.1016/j.compositesb.2015.06.013.
82. Swolfs, Y., I. Verpoest, and L. Gorbatikh, *Tensile failure of hybrid composites: measuring, predicting and understanding.* IOP Conference Series: Materials Science and Engineering, 2016. **139**: p. 012008. DOI: 10.1088/1757-899x/139/1/012008.

83. Xu, W., et al., *EM Performance Analysis of Radomes with Material Properties Errors.* IEEE Antennas and Wireless Propagation Letters 2014. **13**: p. 848-851. DOI: 10.1109/LAWP.2012.2320898.
84. *E-Glass Fiber*. 2001: AZO Materials.
85. Tekinalp, H.L., et al., *Highly oriented carbon fiber–polymer composites via additive manufacturing.* Composites Science and Technology, 2014. **105**: p. 144-150. DOI: 10.1016/j.compscitech.2014.10.009.
86. Wang, X., et al., *3D printing of polymer matrix composites: A review and prospective.* Composites Part B, 2016. **110**: p. 442 - 458. DOI: 10.1016/j.compositesb.2016.11.034.
87. Merati, P., et al., *Underhood Buoyancy Driven Flow - An experimental study.* J. Heat Transfer, 2011. **133**(8). DOI: 10.1115/1.4003758.
88. Bhatnagar, N. and N. Asija, *Durability of high-performance ballistic composites*, in *Lightweight Ballistic Composites: Military and Law-Enforcement Aplications*, A. Bhatnagar, Editor. 2016, Woodhead Publishing
89. Fu, S.-Y. and B. Lauke, *Effects of Fiber Length an Fiber Orientation Distributions on th Tensile Strength of Short-Fiber-Reinforced Polymers.* Composites Science and Technology, 1996. **56**: p. 1179 - 1190.
90. Paranthaman, M.P., et al., *Binder Jetting: A Novel NdFeB Bonded Magnet Fabrication Process.* Jom, 2016. **68**(7): p. 1978-1982. DOI: 10.1007/s11837-016-1883-4.
91. Kumar, S., *Selective Laser Sintering/Melting*, in *Compresensive Materials Processing*, S. Hashmi, et al., Editors. 2014, Elsevier. p. 93 - 134.
92. Abbott, A.C., et al., *Process-structure-property effects on ABS bond strength in fused filament fabrication.* Additive Manufacturing, 2018. **19**: p. 29-38. DOI: 10.1016/j.addma.2017.11.002.
93. Melnikova, R., A. Ehrmann, and K. Finsterbusch, *3D printing of textile-based structures by Fused Deposition Modelling (FDM) with different polymer materials.* IOP Conference Series: Materials Science and Engineering, 2014. **62**. DOI: 10.1088/1757-899X/62/1/012018.
94. Duty, C.E., et al., *A Viscoelastic Model for Evaluating Extrusion-Based Print Conditions.* Conference: Solid Freeform Fabrication Symposium, 2017.
95. Menard, K.P., *Dynamic Mechanical Analysis - A Practical Introduction*. 1999, Boca Raton, FL: CRC Press.
96. Dong, Y., X. Min, and W.S. Kim, *A 3-D-Printed Integrated PCB-Based Electrochemical Sensor System.* IEEE Sensors Journal, 2018. **18**(7). DOI: 10.1109/JSEN.2018.2801459.
97. Hmeidat, N.S., et al., *Mechanical anisotropy in polymer composites produced by material extrusion additive manufacturing.* Additive Manufacturing, 2020. **34**. DOI: 10.1016/j.addma.2020.101385.
98. Wang, B., et al., *3D printing of in-situ curing thermally insulated thermosets.* Manufacturing Letters, 2019. **21**: p. 1-6. DOI: 10.1016/j.mfglet.2019.06.001.
99. Invernizzi, M., et al., *UV-Assisted 3D Printing of Glass and Carbon Fiber-Reinforced Dual-Cure Polymer Composites.* Materials, 2016. **9**(583). DOI: 10.3390/ma9070583.
100. Lewis, J.A., *Direct Ink Writing of 3D Functional Materials.* Advanced Functional Materials, 2006. **16**: p. 2193 - 2204. DOI: 10.1002/adfm.200600434.
101. Gibson, I., D. Rosen, and B. Stucker, *Direct Write Technologies*, in *Additive Manufacturing Technologies*. 2015, Springer: New York.
102. Wang, J. and L. Shaw, *Rheological and extrusion based behavior of dental porcelain slurries for rapid prototyping applications.* Materials Science and Engineerin: A, 2005. **397**(1 - 2): p. 314 - 321. DOI: 10.1016/j.msea.2005.02.045.
103. Yan, C., et al., *3D printing of bioinspired textured surfaces with superamphiphobicity.* Nanoscale, 2020. **12**: p. 2924 - 2938. DOI: 10.1039/c9nr09620e.

104. Truby, R.L. and J.A. Lewis, *Printing soft matter in three dimensions.* Nature Reviews Materials, 2016. **540**: p. 371 - 378 DOI: 10.1038/nature21003.
105. Wallin, T.J., J. Pikul, and R.F. Shepherd, *3D printing of soft robotic systems.* Nature Reviews Materials, 2018. **3**: p. 84 - 100. DOI: 10.1038/s41578-018-0002-2.
106. Engelberg, P.I. and G.C. Tesoro, *Mechanical and Thermal Properties of Epoxy Resins With Reversible Crosslinks.* Polymer Engineering & Science, 1990. **30**(5): p. 303 - 307. DOI: 10.1002/pen.760300507.
107. *Epiclon HP-6000 data sheet*. 2015, DIC Corporation.
108. *Technical Data Sheet - Epon Resin 164*, Hexion, Editor. 2002.
109. *Technical Data Sheet, Comparison data of cured resin*. Nov. 2015, DIC Corporation.
110. *Data Sheet - 600F Duralco 4460*. 2018, Contronics.
111. Fox, J.G. and P.J. Flory, *Second-Order Transition Temperatures and Related Properties of Polystyrene. I. Influence of Molecular Weight.* J. of Applied Physics, 1950. **21**(581). DOI: 10.1063/1.1699711.
112. Fried, J.R., *Polymer Science & Technology*. 2 ed, ed. N. Radhuber. 2003, NJ: Pearson.
113. Dimarzio, E.A. and J.H. Gibbs, *Molecular Intrepretation of Glass Temperature Depression by Plasticizers.* Journal of Polymer Science: Part A, 1963. **1**: p. 1417 - 1428. DOI: 10.1002/pol.1963.100010428.
114. Langer, E., et al., *Plasticizers Derived from Post-Consumer PET*. Plastics Design Library, ed. W. Andrew. 2019: Elsevier.
115. Flory, P.J., *Statistical Mechanics of Swelling of Network Structures.* Journal of Chemical Physics, 1950. **18**(108). DOI: 10.1063/1.1747424.
116. Venditti, R.A., et al., *Free Volume After Cure vs. Fractional Conversion for a High-T, Epoxy/Amine Thermosetting System.* Journal of Applied Polymer Sciences, 1995. **56**: p. 1207 - 1220.
117. Gillham, J.K., *Formation and Properties of Thermosetting and High Tg Polymric Materials.* Polymer Engineering and Science, 1986. **26**(20): p. 1429 - 1433. DOI: 10.1002/pen760262012.
118. Callister, W.D. and D.G. Rethwisch, *Materials Science and Engineering, An Introduction*. 9 ed. 2014: Wiley.
119. Kumar, A.A., M. Alagar, and R.M.V.G.K. Rao, *Synthesis and characterization of siliconized epoxy-1,3-bis(maleimido) benzene intercrosslinked matrix materials.* Polymer, 2002. **43**: p. 693 - 702.
120. MacVarish, N.K., *Understanding Your Data Sheet: Heat Deflection Temperature.* Impact Plastics, 2018.
121. Wang, Y., et al., *Preparation and Major Properties of Montmorillonite/Epoxy Nanocomposites.* Key Engineering Materials, 2003. **249**: p. 413-416. DOI: 10.4028/www.scientific.net/KEM.249.413.
122. ASTM, *E1545 - Standard Test Method for Assignment of the Glass Transition Temperature by Thermomechanical Analysis*. 2016.
123. ASTM, *D7028 - Standard Test Method for Glass Transition Temperature (DMA Tg) of Polymer Matrix Composites by Dynamic Mechanical Analysis (DMA)*. 2015.
124. ASTM, *E1356 - Standard Test Method for Assignment of the Glass Transition Temperatures by Differential Scanning Calorimetry*. 2014.
125. Gupta, M.K., *Glass Transiton Measurments on Automotive Coatings by DSC, DMA, and TMA*, in *American Society for Testing and Materials*, R.J. Seyler, Editor. 1994: Philadelphia. p. 293 - 301.
126. Paroli, R.M. and J. Penn, *Measuring the Glass Transition Temperature of EPDM Roofing Materials: Comparison of DMA, TMA, and DSC Techniques, Assignment of the Glass Transition, ASTM STP 1249*, in *American Socitey for Testing and Materials*, R.J. Seyler, Editor. 1994: Philadelphia. p. 269 - 276.

127. Martin, J.L., *Kinetic analysis of two DSC peaks in the curing of an unsaturated polyester resin catalyzed with methylethylketone peroxide and cobalt octoate.* Polymer Engineering & Science, 2007. **47**(1): p. 62-70. DOI: 10.1002/pen.20667.
128. Simon, S.L. and J.K. Gillham, *Thermosetting Cure Diagrams: Calculation and Application.* Journal of Applied Polymer Sciences, 1994. **53**: p. 709 - 727.
129. Hardis, R., et al., *Cure kinetics characterization and monitoring of an epoxy resin using DSC, Raman spectroscopy, and DEA.* Composites Part A: Applied Science and Manufacturing, 2013. **49**: p. 100-108. DOI: 10.1016/j.compositesa.2013.01.021.
130. Kraus, G. and J.T. Gruver, *Thermal expansion, free volume, and molecular mobility in a carbon black-filled elastomer.* Journal of Polymer Science Part A-2: Polymer Physics, 1970. **8**(4): p. 571 - 581. DOI: 10.1002/pol.1970.160080408.
131. ASTM, *E831 - Standard Test Method for Linear Thermal Expansion of Solid Materials by Thermomechanical Analysis.* 2019.
132. *A Beginners Guide to TMA 4000*, P. Elmer, Editor. 2018.
133. ASTM, *D648 - Standard Test Method for Deflection Temperature of Plastics Under Flexural Load in the Edgewise Position*. 2018.
134. ASTM, *E2092 - Standard Test Method for Distortion Temperature in Three-Point Bending by Thermomechanical Analysis*. 2018.
135. Dvornic, P.R., J.D. Jovanovic, and M.N. Govedarica, *On the Critical Molecular Chain Length of Polydimethylsiloxane.* Journal of Applied Polymer Sciences, 1993. **49**: p. 1497 - 1507.
136. *Polymer Properties Database* in *Glass Transition Temperature*, Crow, Editor. 2019.
137. Chan, L.C., H.N. Nae, and J.K. Gillham, *Time-Temperature-Transformation (TTT) Diagrams of High Tg Epoxy Systems: Competition Between Cure and Thermal Degradation.* Journal of Applied Polymer Sciences, 1984. **29**: p. 3307 - 3327.
138. Xie, T., D.E. Rodak, and W.R. Rodgers, *Shape Memory Epoxy Polymers*, U.S.P.a.T. Office, Editor. 2008, GM Global Technology Operations, Inc.
139. Usuki, A., et al., *Composite material containing a layered silicate*, U.P.a.T. Office, Editor. 1988, Toyota Central R&D Labs Inc: United States.
140. Khanbabaei, G., et al., *Preparation and Properties of Epoxy-Clay Nanocomposites.* Journal of Macromolecular Science, Part B, 2007. **46**(5): p. 975-986. DOI: 10.1080/00222340701457287.
141. Johnson, J., *Runaway reaction lead to four deaths.* Chemical and Engineers News, 2009. **87**(38): p. 8.
142. Abu-Thabit, N.Y., *Thermochemistry of Acrylamide Polymerization: An Illustration of Auto-acceleration and Gel Effect.* World Journal of Chemical Education, 2017. **5**(3): p. 94 - 101. DOI: 10.12691/wjce-5-3-3.
143. Binks, F.C., et al., *Investigating the mechanism through which ionic liquids initiate the polymerisation of epoxy resins.* Polymer, 2018. **139**: p. 163-176. DOI: 10.1016/j.polymer.2018.01.087.
144. Turut, A. and E. Sancaktar, *Viscoelastic and Processing Effects on the Fiber-Matrix Interphase Strength. Part II. The Effects of Cure Temperature Time and Curing Agent Content.* Journal of Adhesion, 1992. **38**(1-2): p. 111 - 129. DOI: 10.1080/00218469208031270.
145. Minty, R.F., J.L. tohmason, and H.N. Petersen, *The Role of the Epoxy Resin: Curing Agent Ratio in Composite Interfacial Strength by Single Fibre Microbond Test*, in *20th International Conference on Composite Materials*. 2015: Copenhagen.
146. Rios, O., et al., *3D printing via ambient reactive extrusion.* Materials Today Communications, 2018. **15**: p. 333-336. DOI: 10.1016/j.mtcomm.2018.02.031.

147. Prolongo, S.G., et al., *Printable self-heating coatings based on the use of carbon nanoreinforcements.* Polymer Composites, 2019. **41**(1): p. 271-278. DOI: 10.1002/pc.25367.
148. Dodiuk, H., S. kenig, and I. Liran, *Room Temperature Curing Epoxy Adhesives for Elevated Temperature Service.* Journal of Adhesion, 1986. **11**(2): p. 227 - 251. DOI: doi.org/10.1080/00218468708071245.
149. Rahmathullah, A.M., et al., *Room Temperature Ionic Liquids as Thermally Latent Initiators for Polymerization of Epoxy Resins.* Macromolecules, 2009. **42**(9): p. 3219 - 3221.
150. Appelhans, L., et al. *Polymer Network Formation in Epoxy-Acrylate Dual-Cure Thermoset Resins for Direct Ink Write Additive Manufacturing*. in *APS March Meeting 2020*. 2020. Denver, CO.
151. Sigma-Aldrich, *1-Ethyl-3-methylimidazolium dicyanamide Technical Data Sheet.* 2020.
152. Sigma-Aldrich, *Dicyandiamide Technical Data Sheet.* 2020.
153. *Safety Data Sheet - 4,4'-Diaminodiphenyl sulfone for synthesis.* Millipore Sigma, 2017.
154. Neumeyer, T., et al., *Influence of an imidazolium salt on the curing behaviour of an epoxy-based hot-melt prepreg system for non-structural aircraft applications.* CEAS Aeronautical Journal, 2014. **6**: p. 31 - 37. DOI: 10.1007/s13272-014-0127-y.
155. Hodd, K., *Comprehensive Composite Materials*, ed. A. Kelly and C. Zweben. 2000: Elsevier Ltd.
156. Hu, J., et al., *Isothermal Curing Kinetics of a Flame Retardant Eposy Resin Containing DOPO investigated by DSC and rheology.* Thermochimical Acta, 2016. **632**: p. 56 - 63. DOI: 10.1016/j.tca.2016.02.010.
157. Hourston, D.J., J.M. Lane, and H.X. Zhang, *Toughening of Epoxy Resins with Thermoplastics: 3. An Investigation into the Effects of Composition on the Properties of Epoxy Resin Blends.* Polymer International, 1997. **42**: p. 349 - 355.
158. Blakhaman, Y., *Adducts of diaminodiphenyl sulfone compounds as hardeners for epoxy resins*, U.P.a.T. Office, Editor. 1992, Huntsman Advanced Materials Americas LLC.
159. Ryan, M.E. and A. Dutta, *Kinetics of epoxy cure: a rapid technique for kinetic parameter estimation.* Polymer, 1979. **20**: p. 203 - 203.
160. Wisanrakkit, G. and J.K. Gillham, *The glass transition temperature (T g) as an index of chemical conversion for a high-T g amine/epoxy system: Chemical and diffusion-controlled reaction kinetics.* Applied Polymer Science, 1990. **41**(11 - 12): p. 2885 - 2929. DOI: 10.1002/app.1990.070411129.
161. Charlesby, A. *Gel Formation and Molecular Weight Distribuition in Long-Chain Polymers*. in *Proceedings of the Royal Society of London. Series A, Mathematical and Physical Sciences*. 1954. JSTOR.
162. ASTM, *Standard Test Method for Gel Time of Thermosetting Coating Powder*. 2017.
163. Hinrickhs, R.J., *Rheological Cure Transformation Diagrams for Evaluating Polymer Cure Dynamics.* ACS Symposium Series, 1983: p. 187 - 199.
164. Pollard, M. and J.L. Kardos, *Analysis of Epoxy Resin Curing Kinetics Using the Avrami Theory of Phase Change.* Polymer Engineering & Science, 1987. **27**(11): p. 829 - 836.
165. Brostow, W. and N.M. Glass, *Cure progress in epoxy systems: dependence on temperature and time.* Materials Research Innovations, 2003. **7**(3): p. 125-132. DOI: 10.1007/s10019-002-0222-2.
166. Winter, H.H. and F. Chambon, *Analysis of Linear Viscoelasticity of a Crosslinking Polymer at the Gel Point.* Journal of Rheology, 1986. **30**(2): p. 367-382. DOI: 10.1122/1.549853.
167. Enns, J.B. and J.K. Gillham, *Time-Temperature-Transformation (TTT) Cure Diagram: Modeling the Cure Behavior of Thermosets.* Applied Polymer Science, 1983. **28**(8): p. 2567 - 2591. DOI: 10.1002/app.1983.070280810.

168. Rahmani, N., et al., *The effect of post cure temperature on fiber/matrix adhesion of T650/Cycom 5320-1 using the micro-droplet technique.* Polymer Testing, 2015. **46**: p. 14-20. DOI: 10.1016/j.polymertesting.2015.05.012.
169. Kissinger, H.E., *Reaction Kinetics in differential thermal analysis.* Analytical Chemistry, 1957. **29**: p. 1302 - 1706. DOI: 10.1021/ac60131a045.
170. Gu, A. and G. Liang, *Thermal degradation behaviour and kinetic analysis of epoxy/montmorillonite nanocomposites.* Polymer Degradation and Stability, 2003. **80**(2): p. 383 - 391. DOI: 10.1016/S0141-3910(03)00026-0.
171. Shutz, H., *Lifetime assessment of epoxies by the kinetics of thermal degradation.* Journal of Applied Polymer Sciences, 2003. **91**: p. 1886 - 1886.
172. Lima, P., et al., *3D Printing of Porcelain by Layerwise Slurry Deposition.* Journal of the European Ceramic Society, 2018. **38**(9): p. 3395 - 3400. DOI: 10.1016/j.jeurceramsoc.2018.03.014.
173. Fateri, M., et al., *Feasibility study on additive manufacturing of recyclable objects for space applications.* Additive Manufacturing, 2018. **24**: p. 400 - 404. DOI: 10.1016/j.addma.2018.09.020.
174. Curzons, A.D., D.C. Constable, and V.L. Cunningham, *Solvent selection guide: a guide to the integration of environmental, health and safety criteria into the selection of solvents.* Clean Products and Processes, 1999. **1**.
175. Zhang, D., J. Ye, and H.Y. Sheng, *Free-edge and ply cracking effect in cross-ply laminated composites under uniform extension and thermal loading.* Composite Structures, 2006. **76**(4): p. 314 - 325. DOI: 10.1016/j.compstruct.2005.04.021.
176. Compton, B.G., et al., *Direct-write 3D printing of NdFeB bonded magnets.* Materials and Manufacturing Processes, 2016. **33**(1): p. 109-113. DOI: 10.1080/10426914.2016.1221097.
177. Kumar, S.K.S., et al., *Benzoxazine–bismaleimide blends: Curing and thermal properties.* European Polymer Journal, 2007. **43**(12): p. 4084 - 4096. DOI: 10.1016/j.eurpolymj.2007.09.012.
178. Jouyandeh, M., et al., *'Cure Index' for thermoset composites.* Progress in Organic Coatings, 2019. **127**: p. 429-434. DOI: 10.1016/j.porgcoat.2018.11.025.
179. Kim, K.-H., D.-H. Choi, and H.-S. Kim, *Design optimization of a carbon fiber reinforced composite automotive lower arm.* Composites Part B: Engineering, 2014. **58**: p. 400 - 407. DOI: 10.1016/j.compositesb.2013.10.067.
180. Taylor, G.A., *Fabrication of glass fiber-reinforced transparent composites using vacuum asisted resin transfer molding process*, in *Aerospace Engineering*. 2014, Missouri University of Science and Technology. p. 39.
181. Kennedy, M.A.D., *Development of Cost Effective Composites using Vacuum Processing Technique*, in *Mechanical Engineering*. 2018, Ohio State University: Russ College of Engineering and Technology. p. 130.
182. Wang, Y., et al., *3D-Printed All-Fiber Li-Ion Battery toward Wearable Energy Storage.* Advanced Functional Materials, 2017. **27**(43). DOI: 10.1002/adfm.201703140.
183. Mishanaevsky, L.J. and G. Dai, *Hybrid carbon / glass fiber composites: Micromechanical analysis of structure-damage resitance relationships.* Computational Materials Science, 2014. **81**: p. 630 - 640. DOI: 10.1016/j.commatsci.2013.08.024.
184. *Fracture Processes of Aerospace Materials*, in *Introduction to Aerospace Materials*, A.P. Mouritz, Editor. 2012, Woodhead Publishing.
185. *E-Glass Fibre*, A. Materials, Editor. 2001.
186. *S-Glass Fibre.* AZO Materials, 2001.
187. *matweb.com*. MatWeb Material Property Data. ASM International.
188. Hexcel, *HexTow AS4 Carbon Fiber Product Data Sheet.* 2019.
189. Zoltek, *Zoltek PX30 Data Sheet.* Zoltek, Toray Group, 2019.

190. Godara, A., et al., *Influence of carbon nanotube reinforcement on the processing and the mechanical behaviour of carbon fiber/epoxy composites.* Carbon, 2009. **47**(12): p. 2914-2923. DOI: 10.1016/j.carbon.2009.06.039.
191. Cho, J., J.Y. Chen, and I.M. Daniel, *Mechanical enhancement of carbon fiber/epoxy composites by graphite nanoplatelet reinforcement.* Scripta Materialia, 2007. **56**(8): p. 685-688. DOI: 10.1016/j.scriptamat.2006.12.038.
192. Withers, G.J., et al., *Improved mechanical properties of an epoxy glass–fiber composite reinforced with surface organomodified nanoclays.* Composites Part B: Engineering, 2015. **72**: p. 175-182. DOI: 10.1016/j.compositesb.2014.12.008.
193. Patel, A., O. Kravchenko, and I. Manas-Zloczower, *Effect of Curing Rate on the Microstructure and Macroscopic Properties of Epoxy Fiberglass Composites.* Polymers (Basel), 2018. **10**(2). DOI: 10.3390/polym10020125.
194. Zhang, J. and B.L. Fox, *Characterization and Analysis of Delamination Fracture and Nanocreep Properties in Carbon Epoxy Composites Manufactured by Different Processes.* Journal of Composite Materials, 2005. **40**(14): p. 1287-1299. DOI: 10.1177/0021998305057438.
195. Van Hattum, F. and C. Bernado, *A model to predict the strength of short fiber composites.* J. Polym Comp, 1999. **20**(4): p. 524 - 533. DOI: 10.1002/pc.10376.
196. Kelly, A. and W.R. Tyson, *Tensile Properties of Fibre-Reinforced Metals: Coppen/Tungsten and Copper/Molybdenum.* J. Mech. Phys. Solids, 1965. **13**: p. 329 - 350.
197. Ohsawa, T., et al., *Temperature Dependence of Critical Fiber Length for Glass Fiber-Reinforced Thermosetting Resins.* J. of Applied Polymer Science, 1978. **22**: p. 3203-3212. DOI: 10.1002/app.1978.070221115.
198. Hao, W., et al., *Preparation and characterization of 3D printed continuous carbon fiber reinforced thermosetting composites`.* Polymer Testing, 2018. **65**: p. 29 - 34. DOI: 10.1016/j.polymertesting.2017.11.004.
199. Fu, S.-Y., et al., *Tensile properties of short-glass-fiber- and short-carbon-fiber-reinforced polypropylene composites.* Composites Part A, 2000. **31**: p. 1117 - 1125.
200. Bell, J.P., *Flow Orientation of Short Fiber Composites.* Journal of Composite Materials, 1969. **3**(2). DOI: 10.1177/002199836900300204.
201. Es-Said, O.S., et al., *Effect of Layer Orientation on Mechanical Properties of Rapid Prototyped Samples.* Materials and Manufacturing Processes, 2000. **15**(1): p. 107 - 122. DOI: 10.1080/10426910008912976.
202. Romberg, S.K., et al. *Understanding print stability in material extrusion additive manufacturing of thermoset composites*. in *Innovative Materials for Additive Manufacturing (IMAM)*. 2020. New Mexico.
203. Agarwala, M.K., et al., *Structural quality of parts processed by fused deposition.* Rapid Prototyping Journal, 1996. **2**(4): p. 4 - 19.
204. Lee, J.-H., J.P. Singer, and E.L. Thomas, *Micro-Nanostructured Mechanical Metamaterials.* Advanced Materials, 2015. **24**(36): p. 4782 - 4810. DOI: 10.1002/adma.201201644.
205. Li, N., Y. Li, and S. Liu, *Rapid prototyping of continuous carbon fiber reinforced polylactic acid composites by 3D printing.* Journal of Materials Processing Technology, 2016. **238**: p. 218 - 225. DOI: 10.1016/j.jmatprotec.2016.07.025.
206. Markforged. *Markforged X7 Industrial 3D Printer*. 2020 June 2020]; Available from: https://markforged.com/x7/.
207. Halpin, J.C. and J.L. Kardos, *The Halpin-Tsai Equations: A Review.* Polymer Engineering & Science, 1976. **16**(5): p. 334 - 352.

208. Boccaccini, A.R., et al., *On the Effective Young's Modulus of Elasticity for Porus Materials: Microstructure Modelling and Comparison Between Calculated and Experimental Values.* Journal of the Mechanical Behavior of Materials, 1993. **4**(2): p. 119 - 128.
209. Berenbaum, R. and I. Brodie, *Measurement of the tensile strength of brittle materials.* British Journal of Applied Physics 1959. **10**: p. 281 - 287.
210. Leguillon, D., É. Martin, and M.-C. Lafarie-Frenot, *Flexural vs. tensile strength in brittle materials.* Comptes Rendus Mécanique, 2015. **343**(4): p. 275-281. DOI: 10.1016/j.crme.2015.02.003.
211. Swaminathan, G. and K. Shivakumar, *A Re-examination of DMA Testing of Polymer Matrix Composites.* Journal of Reinforced Plastics and Composties, 2009. **28**(8): p. 979 - 994. DOI: 10.1177/0731684407087740.
212. Bullock, R.E., *Strength Ratios of Composite Materials in Flexure and Tesnison.* J. Composite Materials, 1974. **8**: p. 200 - 206
213. Mortazavian, S. and A. Fatemi, *Effects of fiber orientation and anisotropy on tensile strength and elastic modulus of short fiber reinforced polymer composites.* Composites Part B: Engineering, 2015. **72**: p. 116 - 129. DOI: 10.1016/j.compositesb.2014.11.041.
214. Hassan, A., N.A. Rahman, and R. Yahya, *Extrusion and injection-molding of glass fiber/MAPP/polypropylene: effect of coupling agent on DSC, DMA, and mechanical properties.* Journal of Reinforced Plastics and Composties, 2011. **30**(14): p. 1223 - 1232. DOI: 10.1177/0731684411417916.
215. Zhang, Y., et al., *Mechanical and thermal properties of basalt fiber reinforced poly(butylene succinate) composites.* Materials Chemistry and Physics, 2012. **133**: p. 845 - 849. DOI: 10.1016/j.matchemphys.2012.01.105.
216. *Technical Data Sheet EPON Resin 826*. 2005, Hexion.
217. *Technical Data Sheet EPON Resin 164*. 2018, Hexion.
218. *Data Sheet - XU 35910 Benzoxazine Resin*. 2014, Huntsman.
219. *EP17HT Technical Data Sheet*. 2018, MasterBond.
220. Hmeidat, N.S., J.W. Kemp, and B.G. Compton, *High-strength epoxy nanocomposites for 3D printing.* Composites Science and Technology, 2018(160): p. 9 - 20.
221. Winter, H.H. and F. Chambon, *Analysis of Linear Viscoelasticity of a Crosslinking Polymer at the Gel Point.* Journal of Rheology, 1986. **30**(2): p. 367 - 382.
222. ASTM, *D790 - Standard Test Methods for Flexural Properties of Unreinforced and Reinforced Plastics and Electrical Insulating Materials*. 2017.
223. Rasband, W.S., *ImageJ*. 1997 - 2018, U.S. National Institutes of Health: Bethesda, Maryland, USA.

APPENDIXES

Appendix A: All epoxies considered for this work

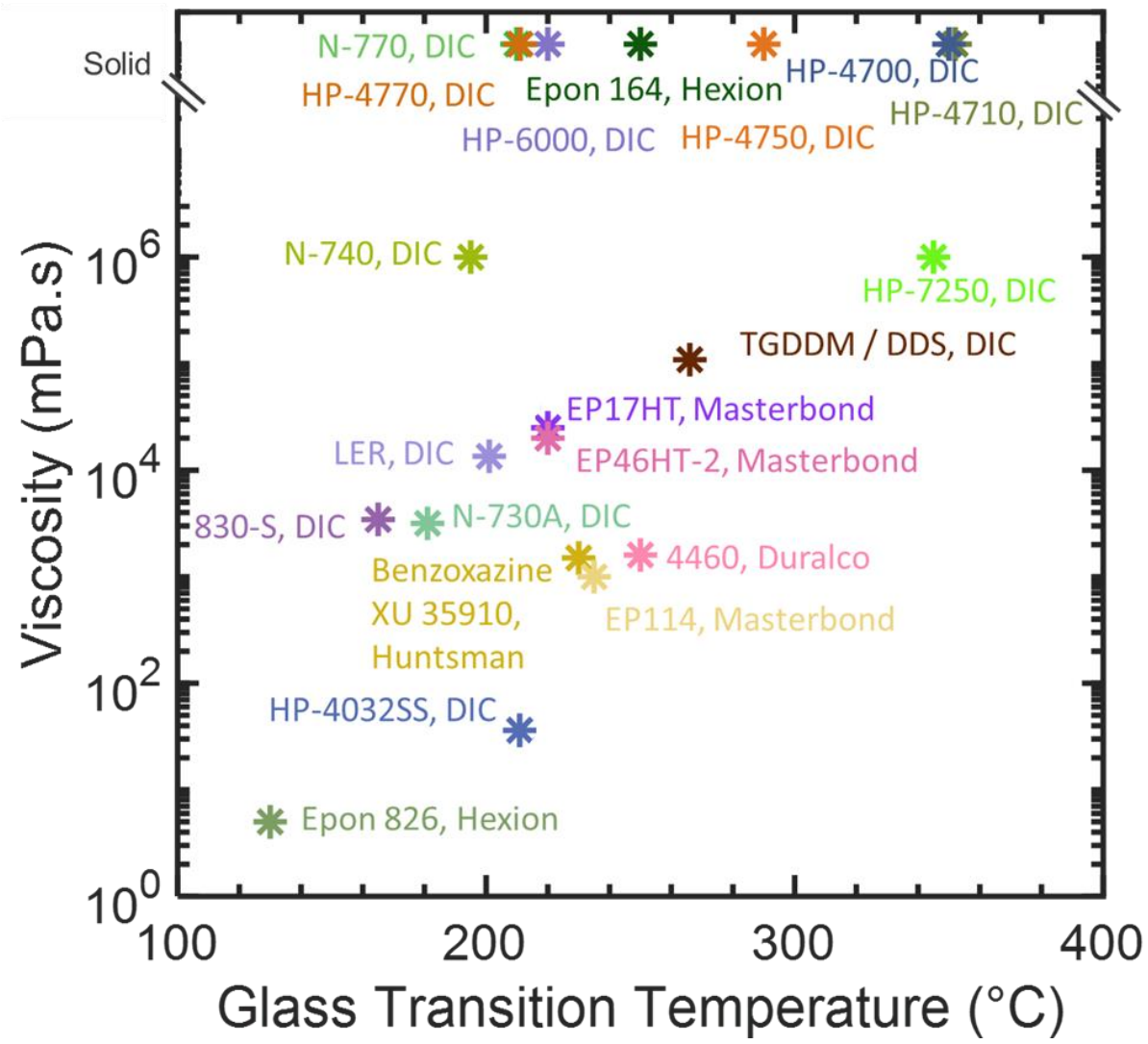

Room temperature viscosity and glass transition temperature of epoxies considered for this work. Glass transition temperatures are presented as reported on the safety data sheet. The curing agents and profiles vary among companies. All DIC resins are cured with DDS which is unable to be incorporated for DIW at this time. As such, values are artificially high. 4460 from Duralco, EP17HT from Masterbond, and HP-4032SS, HP-7250, and HP-6000 from DIC were selected for testing based on T_g values, viscosity, cost, and availability. For comparison, Epon 826 is liquid at room temperature.

Appendix B: Epoxy-GF flexure results

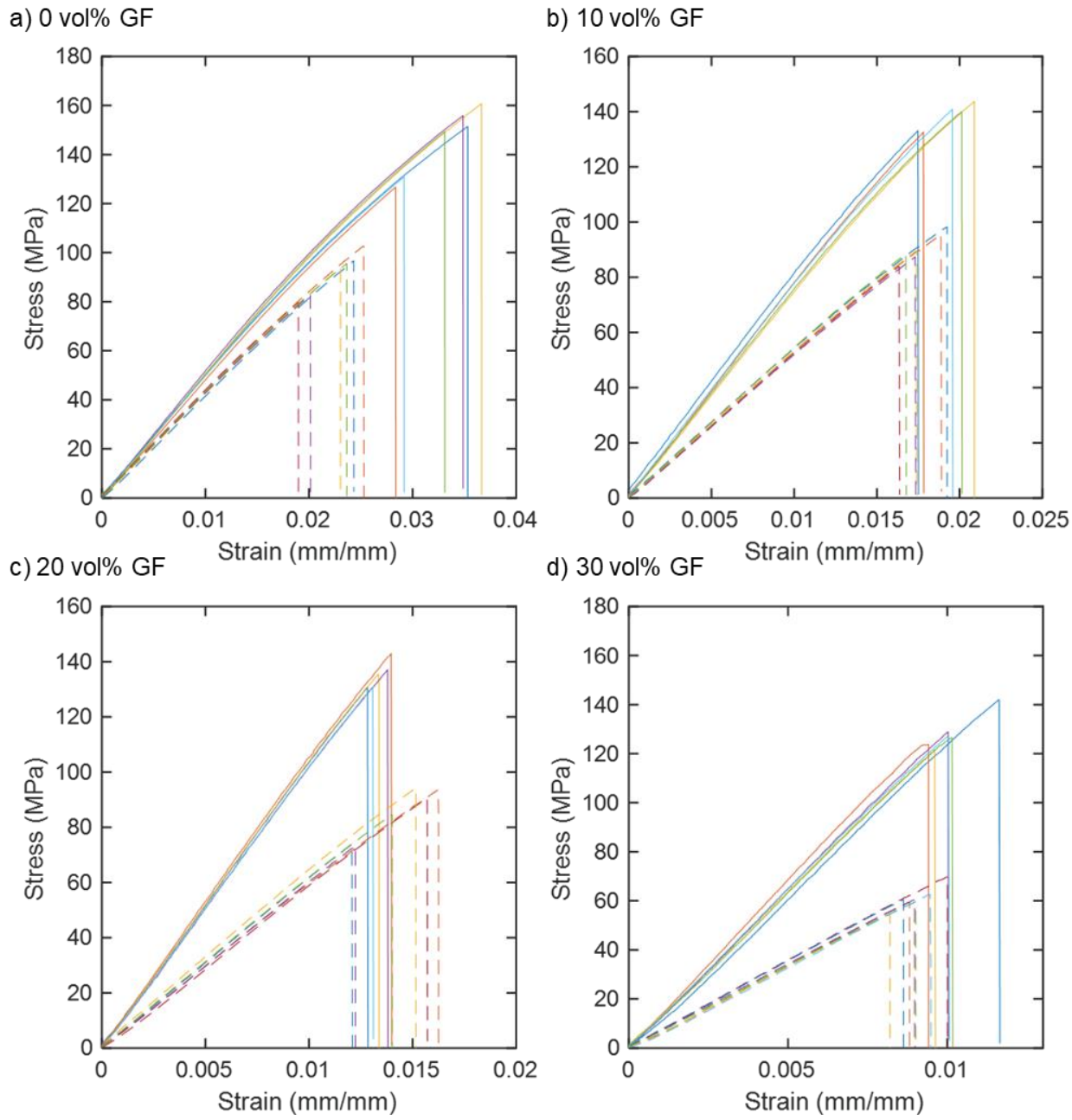

Flexure tests results for a) unfilled, b) 10 vol%, c) 20 vol%, and d) 30 vol% glass fibers. Solid lines denote axial testing while dashed lines indicate transverse.

Appendix C: Fracture surfaces of transverse tested samples

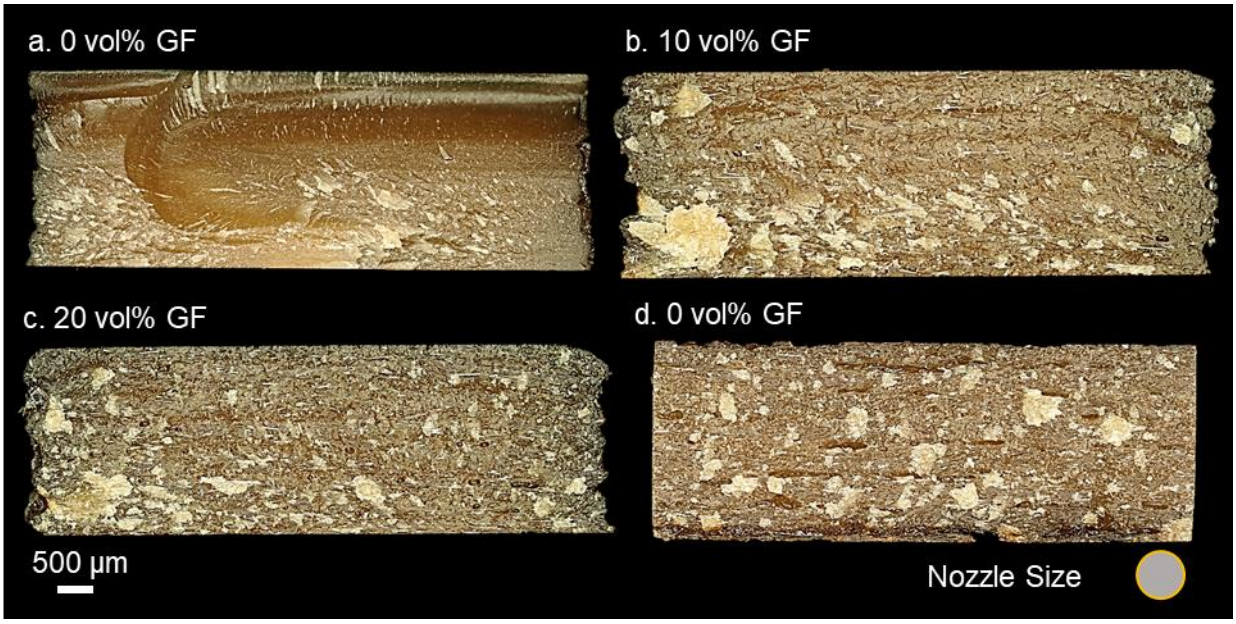

Fracture surface of a) unfilled 6040, b) 10 vol%, c) 20 vol%, and d) 30 vol% fiber formulations tested in 3pt-flexure against the print path.

VITA

Madeline Wimmer was born and raised in Maryville, Tennessee before she attended the University of Tennessee, Knoxville where she earned her Bachelors of Science in Materials Science and Engineering (MSE), Cum Laude in 2018. While in her undergraduate program, Madeline was heavily involved in the Wesley Foundation and MSE departmental events. She helped develop the MSE Ambassadors program to introduce high school students to UT and materials. She also served as the outreach chair of the local Materials Advantage chapter and travelled to Washington, D.C. to meet with Tennessee congressional representatives about the importance of science education and funding. Madeline is passionate about expanding science relatability to larger non-technical audiences.

Her primary research interest is in developing material systems and processes that have a lower negative environmental impact. She sees additive manufacturing as a way to reduce material use by creating near-net shapes and is excited to help shape how this method can be used. After earning a Master of Science in Engineering Science, Madeline will continue at UT as a student in the Bredesen Center for her PhD work.